



저작자표시-비영리-변경금지 2.0 대한민국

이용자는 아래의 조건을 따르는 경우에 한하여 자유롭게

- 이 저작물을 복제, 배포, 전송, 전시, 공연 및 방송할 수 있습니다.

다음과 같은 조건을 따라야 합니다:



저작자표시. 귀하는 원저작자를 표시하여야 합니다.



비영리. 귀하는 이 저작물을 영리 목적으로 이용할 수 없습니다.



변경금지. 귀하는 이 저작물을 개작, 변형 또는 가공할 수 없습니다.

- 귀하는, 이 저작물의 재이용이나 배포의 경우, 이 저작물에 적용된 이용허락조건을 명확하게 나타내어야 합니다.
- 저작권자로부터 별도의 허가를 받으면 이러한 조건들은 적용되지 않습니다.

저작권법에 따른 이용자의 권리는 위의 내용에 의하여 영향을 받지 않습니다.

이것은 [이용허락규약\(Legal Code\)](#)을 이해하기 쉽게 요약한 것입니다.

[Disclaimer](#)

Doctoral Thesis

Bioinspired Polymeric Nanoneedle Array  
for Effective and Robust Anti-biofouling

Hyun-Ha Park

Department of Mechanical Engineering

Graduate School of UNIST

2020

# Bioinspired Polymeric Nanoneedle Array for Effective and Robust Anti-biofouling

Hyun-Ha Park

Department of Mechanical Engineering

Graduate School of UNIST

# Bioinspired Polymeric Nanoneedle Array for Effective and Robust Anti-biofouling

A dissertation  
submitted to the Graduate School of UNIST  
in partial fulfillment of the  
requirements for the degree of  
Doctor of Philosophy

Hyun-Ha Park

12/10/2019

Approved by



---

Advisor

Hoon Eui Jeong



# Bioinspired Polymeric Nanoneedle Array for Effective and Robust Anti-biofouling

Hyun-Ha Park

This certifies that the dissertation of Hyun-Ha Park is approved.

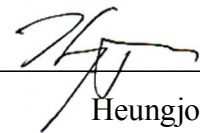
12/10/2019



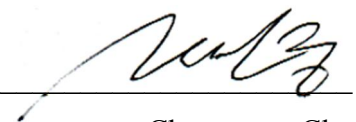
Advisor: Hoon Eui Jeong



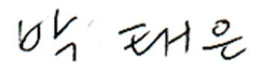
Taesung Kim



Heungjoo Shin



Chaenyung Cha



Tae-Eun Park

## Abstract

In recent years, extensive efforts have been devoted to developing antibiofilm material which can effectively prevent biofilm formation. Currently, the most common method of preventing protein or bacteria adhesion is to impart surface functionalization using PEGylated materials or zwitterionic materials with excellent antifouling properties. This method is resistant to the surface adhesion of proteins and microorganisms but is less mechanically durable and easily damaged by external physical and chemical stimuli, which can lead to the loss of antifouling performance. Bactericidal methods include chemical killing by antibiotics and physical killing due to surface structure. Chemical methods using silver, nitrates, or copper can cause microbial infections due to antibiotic resistance and can be toxic and biologically harmful.

To avoid this problem, researchers have been studying physical killing methods. Nanostructures which can be fabricated using silicon, metal, or polymers have been used to kill bacteria. However, these methods also have many limitations, such as complex fabrication methods, high cost, secondary biofilm formation, and especially the problem of the remaining dead bacterial carcasses. Furthermore, many previous studies, whether concerning the chemical or mechanical approaches, have focused on a single strategy, such as antifouling coatings, bactericidal materials, or nanopatterning. However, these single-strategy approaches have many limitations, such as the drug resistance of bacteria, toxicity to cells and the environment, low antifouling performance, high cost, or low mechanical and chemical durability in the prevention of biofilm formation. Therefore, to overcome these many drawbacks first of all, simple, cost-effective, environmentally friendly and reproducible fabrication methods are strongly required. Moreover, to overcome several problems of the single-strategy approaches, a multi-strategy or hybrid approach should be considered.

This dissertation presents the development of a hybrid strategy based on an antifouling material and bactericidal nanostructures that aim to combine both the antifouling and bactericidal functions to maintain effective anti-biofouling performance.

Our hybrid anti-biofouling surface consists of nanostructures with the biocompatible materials polyethylene glycol dimethacrylate (PEGDMA) and cellulose acetate (CA). The biocompatible nanostructure array was easily fabricated using UV molding and soft lithography. Moreover, 2-methacryloyloxyethyl phosphorylcholine (MPC), a zwitterionic polymer, was covalently grafted onto the fabricated nanostructures for superior antifouling performance. The surface can be applied to various 3D surfaces and large areas, due to the flexibility of the base material. Based on the synergetic integration of the bio- and ecofriendly nanostructural polymer and MPC, our hybrid strategy can easily fabricate an efficient anti-biofouling surface which can overcome the limitations of previous antifouling and antibacterial surfaces. Furthermore, our hybrid surface has high chemical / structural stability even in wet conditions. Not only can it effectively prevent bacterial attachment, but it also exhibits better bactericidal effects, regardless of the bacterial types, compared with single anti-biofouling strategies (repelling bacteria or killing bacteria). Furthermore, it preserves robust and excellent anti-biofouling activity, even under external stimuli and long-term fouling tests.

This novel hybrid anti-biofouling surface provides a more-promising solution for the prevention of initial bacterial attachment and subsequent biofilm formation. In particular, the hybrid anti-biofouling function makes these surfaces more suitable for applications in which long-term antibacterial activity is required. Also, our developed surfaces can play an important role in solving bio-contamination problems in the medical and marine industries.

**Keywords:** Antifouling, Bactericidal, Nanostructure, Biofilm, Biocompatible, Flexible, Durable,

## Contents

<b>Abstract</b> .....	<b>i</b>
<b>Contents</b> .....	<b>iii</b>
<b>List of figures</b> .....	<b>v</b>
<b>List of tables</b> .....	<b>ii</b>
<b>1. Introduction</b> .....	<b>1</b>
1.1. Research background and motivation.....	1
1.2. Research objectives .....	7
1.3. Research concept and outline.....	8
<b>2. Functionalized Poly(ethylene glycol) dimethacrylate nanoneedle array</b> .....	<b>9</b>
2.1. Introduction.....	9
2.2. Experimental .....	11
2.3. Results and Discussion .....	13
2.3.1. Fabrication of the MPC-grafted PEGDMA NN hybrids .....	13
2.3.2. Chemical mechanism of the MPC-grafted PEGDMA NN hybrids .....	17
2.3.3. Structural stability properties of the PEGDMA NN .....	22
2.3.4. Anti-biofouling properties of PEGDMA nanoneedle arrays .....	24
2.3.5. Durability properties of MPC-PEGDMA-NN hybrid by external stimuli .....	35
2.3.6. Anti-biofouling performance against marine microorganism .....	43
2.4. Summary.....	46
<b>3. Functionalized Cellulose acetate nanoneedle array</b> .....	<b>47</b>
3.1. Introduction.....	47
3.2. Experimental .....	49
3.3. Results and Discussion .....	51
3.3.1. Preparation and structures of the cellulose acetate nanoneedle array .....	51
3.3.2. Chemical mechanism of the MPC-grafted cellulose acetate nanoneedle array .....	54

3.3.3. Surface, mechanical, and optical properties of the MPC-grafted cellulose acetate nanoneedle array .....	60
3.3.4. Evaluation of the biofilm-resistance of the MPC-coated cellulose acetate nanoneedle array .....	65
3.3.5. Long-term evaluation of anti-biofouling performance on the MPC-grafted cellulose acetate nanoneedle .....	69
3.4. Summary .....	71
<b>4. Conclusions and Perspectives .....</b>	<b>72</b>
<b>References .....</b>	<b>74</b>

## List of figures

Figure 1. Previous anti-biofouling methods in medical industry. ....	1
Figure 2. Previous anti-biofouling methods in marine industry. ....	2
Figure 3. Critical cases due to microbe in medical field (left) and Economic loss due to microbe in marine industry (right). ....	2
Figure 4. Existing researches on chemical-based antifouling approach. ....	3
Figure 5. Existing researches on chemical-based bactericidal approach. ....	3
Figure 6. Schematic illustration for the formation of hydration shell. (a) Each unit of the representative PEG materials is integrated with one water molecule. (b) Each unit of the zwitterionic materials is integrated with eight water molecules [9]. ....	4
Figure 7. Micro/nano structures for antifouling in nature. ....	5
Figure 8. Existing researches on structure-based antifouling approach. ....	6
Figure 9. Research objectives. ....	7
Figure 10. Schematic of the fabrication procedure of the MPC-PEGDMA-nanoneedle hybrid. ....	13
Figure 11. Conceptual illustration of the hybrid structure in which the PEGDMA nanoneedle arrays with covalently tethered zwitterionic MPC molecules are uniformly formed on the surface. ....	14
Figure 12. (i) Photograph of the fabricated MPC-PEGDMA-nanoneedle hybrid showing its high flexibility, (ii) an SEM image of the MPC-grafted PEGDMA nanoneedle arrays and, (iii) a TEM image of the cross section of the MPC-grafted PEGDMA nanoneedle. Thickness of the grafted MPC layer is 5 nm. ....	14
Figure 13. Mechanical properties of the PEGDMA (MW: 550) with different concentrations (80 wt%, 90 wt% and 100 wt%) in the dried and swollen states. The swollen samples were submerged in DI water for 18 h before the measurements. ....	15
Figure 14. Contact angle measurements of the planar and nanostructured PUA and PEGDMA (80 wt%) samples before and after MPC grafting. ....	16
Figure 15. ATR-FTIR spectra of the pristine (i) oxygen-plasma treated, and MPC-grafted PEGDMA samples showing detailed peak at $730\text{ cm}^{-1}$ . (ii) oxygen-plasma treated, and MPC-grafted PEGDMA samples in the wavenumber range of $650\text{--}4000\text{ cm}^{-1}$ . ....	17
Figure 16. Deconvoluted peaks of (i) $\text{C}_{1s}$ , (ii) $\text{O}_{1s}$ , (iii) $\text{N}_{1s}$ , (iv) $\text{P}_{2p}$ of XPS spectra of the pristine, oxygen-plasma treated, and MPC-grafted PEGDMA samples. ....	18

Figure 17. (a) ATR-FTIR spectra of the pristine, oxygen-plasma treated, and MPC-grafted PUA samples in the wavenumber range of 650-4000  $\text{cm}^{-1}$ . (b) Deconvoluted peaks of (i)  $\text{C}_{1s}$ , (ii)  $\text{O}_{1s}$ , (iii)  $\text{N}_{1s}$ , and (iv)  $\text{P}_{2p}$  of XPS spectra of the pristine, oxygen-plasma treated, and MPC-grafted PUA samples. .... 19

Figure 18. Chemical reaction mechanism of PEGDMA and MPC via oxygen plasma treatment. .... 20

Figure 19. Swelling ratio of the PEGDMA with different concentrations as functions of the water-exposure time. .... 22

Figure 20. *In-situ* AFM images of swollen PEGDMA NN applied at concentrations of (i) 100 wt%, (ii) 90 wt%, and (iii) 80 wt%. Before the AFM imaging, the samples were submerged in DI water for 18 h. AFM images of the swollen samples were directly obtained from the submerged samples. .... 23

Figure 21. Environmental SEM (ESEM) images of swollen PEGDMA NN applied at concentrations of (i) 100 wt%, (ii) 90 wt%, and (iii) 80 wt%. Before the ESEM imaging, the samples were submerged in DI water for 18 h. The relative humidity of the ESEM chamber was maintained at 100% during the imaging (environmental mode). .... 23

Figure 22. SEM images of the nanoneedle arrays with different pitches (500 nm, 1  $\mu\text{m}$ , and 4  $\mu\text{m}$ ) and ARs (1.5 and 1.0). .... 24

Figure 23. Confocal microscopy images of (i) *E. coli* and (ii) *B. subtilis* cultured on the PEGDMA and MPC-grafted PEGDMA nanoneedle arrays with different pitches and ARs for 18 h. The bacteria were stained with a fluorescent labeling reagent (live/dead bacterial viability kit). .... 25

Figure 24. CFU of *E. coli* and *B. subtilis* grown on various PEGDMA samples with different pitches (AR: 1.5). .... 26

Figure 25. CFU of *E. coli* and *B. subtilis* grown on various PEGDMA samples with different ARs (pitch: 500 nm). .... 26

Figure 26. Confocal microscopy images of *E. coli* cultured on the (i) planar, (ii) MPC-grafted planar, (iii) nanoneedle, and (iv) MPC-grafted nanoneedle samples made of PUA, 100 wt%, 90 wt%, and 80 wt% PEGDMA for 18 h. The bacteria were stained with a fluorescent labeling reagent (live/dead bacterial viability kit). .... 27

Figure 27. Quantification of area coverage of the live (green) and dead (red) cells cultured on various PUA and PEGDMA samples. .... 28

Figure 28. CFU of the *E. coli* grown on various PUA and PEGDMA samples after 0, 3, 18, 24, and 30 h culture. ( $n=9$ ,  $*p < 0.05$ ,  $**p < 0.01$  and  $***p < 0.001$  compared to bare PUA, data was analyzed by a one-way ANOVA). .... 29

Figure 29. Confocal microscopy images of (i) *E. coli* and (ii) *B. subtilis* cultured on the planar glass for 18 h.

The bacteria were stained with a fluorescent labeling reagent (live/dead bacterial viability kit). ..... 29

Figure 30. SEM images of (a) *E. coli* and (b) *B. subtilis* cultured on the PEGDMA NN for 18 h. .... 30

Figure 31. TEM image of *E. coli* cultured on the PEGDMA NN for 18 h. .... 31

Figure 32. Rupture and lysis of bacterial cell as the bactericidal mechanism of nanoneedle structure. .... 31

Figure 33. AFM images of (i) *E. coli* and (ii) *B. subtilis* cultured on the planar PEGDMA and PEGDMA NN for 18 h. .... 32

Figure 34. Confocal microscopy images of *B. subtilis* cultured on the (i) planar, (ii) MPC-grafted planar, (iii) nanoneedle, and (iv) MPC-grafted nanoneedle samples made of PUA, 100 wt%, 90 wt%, and 80 wt% PEGDMA for 18 h. The bacteria were stained with a fluoresce labeling reagent (live/dead bacterial viability kit). .... 33

Figure 35. Quantification of area coverage of the live (green) and dead (red) cells cultured on various PUA and PEGDMA samples. .... 34

Figure 36. CFU of *B. subtilis* grown on various PUA and PEGDMA samples after 0, 3, 18, 24, and 30 h culture. ( $n=9$ , \*  $p < 0.05$ , \*\*  $p < 0.01$  and \*\*\*  $p < 0.001$  compared to bare PUA, data was analyzed by a one-way ANOVA). .... 34

Figure 37. (a) (i) (top) 3D micrograph and (bottom) cross-section, and (ii) SEM images showing the damaged MPC-PUA-NN. False colors were used to emphasize the damaged sites. (b) Confocal fluorescence microscopy images of the (i) *E. coli* and (ii) *B. subtilis* grown on the damaged MPC-PUA-NN (culture hour: 18 h). .... 35

Figure 38. (a) (i) (top) 3D micrograph and (bottom) cross-section, and (ii) SEM images showing the damaged MPC-PEGDMA-NN. False colors were used to emphasize the damaged sites. (b) Confocal fluorescence microscopy images of the (i) *E. coli* and (ii) *B. subtilis* grown on the damaged MPC-PEGDMA-NN (culture hour: 18 h). .... 36

Figure 39. ATR-FTIR spectra of the PEG-grafted Si, MPC-grafted Si, and MPC-grafted PEGDMA on Si samples in the wavenumber ranges of (i)  $650-4000\text{ cm}^{-1}$  and (ii)  $675-1275\text{ cm}^{-1}$ . The PEG-grafted Si was prepared using PEG-aldehyde on a 3-aminopropyltriethoxysilane (APTES)-treated Si surface, which has been used in prior studies. The MPC-grafted Si was prepared based on the UV-induced free radical grafting method widely adopted in several prior studies. The MPC-grafted PEGDMA was prepared by covalently tethering MPC over 80% PEGDMA. .... 37

Figure 40. Three-dimensional micrographs showing the surfaces of the (i) PEG-grafted Si, (ii) MPC-grafted Si, and (iii) MPC-grafted PEGDMA (80 wt%) on Si substrates (a) before and (b) after applying mechanical stimuli. .... 38



Figure 41. Confocal fluorescence microscopy images of *E. coli* on the PEG-grafted, MPC-grafted, and MPC-grafted PEGDMA samples (i) without- and (ii) with mechanical damages after 18 h of culture. .... 39

Figure 42. Confocal fluorescence microscopy images of *B. subtilis* on the PEG-grafted Si, MPC-grafted Si, MPC-grafted PEGDMA (80 wt%) on Si, and MPC-grafted PEGDMA (80 wt%) nanoneedles on Si substrates (i) without- and (ii) with mechanical damages after 18 h of culture. .... 40

Figure 43. ATR-FTIR spectra of the PEGDMA-MPC mixture and MPC-grafted PEGDMA samples in the wavenumber ranges of (i) 650-4000  $\text{cm}^{-1}$ . .... 41

Figure 44. Three-dimensional micrographs showing the surfaces of the PEGDMA-MPC mixture (left) and MPC-grafted PEGDMA samples (right). .... 41

Figure 45. Confocal fluorescence microscopy images of *E. coli* and *B. subtilis* cultured on the PEG-MPC mixture and MPC-grafted PEGDMA samples for 18 h. .... 42

Figure 46. (i) Photograph of *Pyropia yezoensis* (ii) Development shape of *Pyropia yezoensis*. .... 43

Figure 47. Attachment test of *Pyropia yezoensis* on various PUA and PEGDMA samples for 14 days. .... 44

Figure 48. (i) Spore adhesion rate of *Pyropia yezoensis* spore, (ii) Development of *Pyropia yezoensis* spore on various PUA and PEGDMA samples for 14 days. .... 45

Figure 49. Biodegradation mechanism of CA. .... 48

Figure 50. Schematic of the fabrication procedure for the cellulose acetate (CA) nanoneedle array grafted with 2-methacryloyloxyethyl phosphorylcholine (MPC). .... 52

Figure 51. Conceptual illustration of the flexible CA nanoneedle array on which MPC is uniformly coated. .... 53

Figure 52. (i) Photograph of the fabricated MPC-coated CA nanoneedle film, (ii) an SEM image of the CA nanoneedle array, (iii) a TEM image of the single CA nanoneedle coated with MPC. The dark coating layer around the nanoneedle represents the MPC layer with a thickness of 5 nm. .... 53

Figure 53. (a) ATR-FTIR spectra of the pristine and  $\text{O}_2$  plasma-treated CA in the wavenumber range of 650-4000  $\text{cm}^{-1}$ . (b) ATR-FTIR spectra of the MPC-coated CA in the wavenumber range of 650-4000  $\text{cm}^{-1}$ . .... 55

Figure 54. Deconvoluted peaks of (a)  $\text{C}_{1s}$ , (b)  $\text{O}_{1s}$ , (c)  $\text{N}_{1s}$ , and (d)  $\text{P}_{2p}$  of XPS spectra of the pristine,  $\text{O}_2$  plasma-treated, and MPC-coated CA samples. .... 56

Figure 55. Deconvoluted peaks of (a)  $\text{C}_{1s}$ , (b)  $\text{O}_{1s}$ , (c)  $\text{N}_{1s}$ , and (d)  $\text{P}_{2p}$  of XPS spectra of the  $\text{O}_2$  plasma-treated and MPC-coated CA samples and MPC-coated CA samples without  $\text{O}_2$  plasma treatment. .... 57

Figure 56. Carbonyl groups (carboxylic acid and ketone) were generated on various positions of CA unit. .... 58

Figure 57. Contact angle of water droplet on untreated,  $\text{O}_2$  plasma treated and  $\text{O}_2$  plasma treated and MPC coated

surfaces. ....59

Figure 58. MPC reacted with radical intermediates of CA via addition or oligomerization. ....59

Figure 59. Contact angle of water droplet on the planar CA, CA nanoneedle, and MPC-coated nanoneedle surfaces. ....61

Figure 60. Contact angle measurements of the O<sub>2</sub> plasma-treated and MPC-coated nanoneedle samples, which were submerged in DI water for different periods of 0 – 28 d. ....61

Figure 61. ATR-FTIR spectra of the O<sub>2</sub> plasma-treated and MPC-coated nanoneedle samples, which were submerged in DI water for different periods of 0 – 28 d. ....62

Figure 62. A stress-strain curve of the CA sample. ....63

Figure 63. *In-situ* AFM image of the CA nanoneedle submerged in DI water for 18 h. The image was directly acquired from the submerged sample. ....63

Figure 64. Optical transmittance of the pristine CA, CA nanoneedle, and MPC-coated CA nanoneedle samples in the wavelength range of 250-800 nm. ....64

Figure 65. Confocal microscopy images of *E. coli* grown on the planar glass, planar CA, CA nanoneedle, and MPC-coated CA nanoneedle surfaces for 18 h. The bacteria were stained with a fluorescent labeling reagent. ....66

Figure 66. Confocal microscopy images of *B. subtilis* grown on the planar glass, planar CA, CA nanoneedle, and MPC-coated CA nanoneedle surfaces for 18 h. The bacteria were stained with a fluorescent labeling reagent. ....66

Figure 67. (i) Coverage area of the live (green) and dead (red) *E. coli* cultured on the control and various CA samples. (ii) CFU of the *E. coli* grown on the control and various CA samples after 0, 3, 18, 24, and 30 h culture ( $n = 9$ , \*  $p < 0.05$ , \*\*  $p < 0.01$ , and \*\*\*  $p < 0.001$  compared to control; data was analyzed by a one-way ANOVA). ....67

Figure 68. (i) Coverage area of the live (green) and dead (red) *B. subtilis* cultured on the control and various CA samples. (ii) CFU of the *B. subtilis* grown on the control and various CA samples after 0, 3, 18, 24, and 30 h culture ( $n = 9$ , \*  $p < 0.05$ , \*\*  $p < 0.01$ , and \*\*\*  $p < 0.001$  compared to control; data was analyzed by a one-way ANOVA). ....68

Figure 69. (i) Confocal microscopy images of *P. aeruginosa* grown on the planar glass, planar CA, CA nanoneedle, and MPC-coated CA nanoneedle surfaces for 28 d. The bacteria were stained with a fluorescent labeling reagent. (ii) CFU of the *P. aeruginosa* grown on the control and various CA samples after 0 h, 3 h, 18 h, 1 d, 7 d, 14 d, 21 d, and 28 d culture. ....70

## List of tables

Table 1. Surface elemental compositions of C <sub>1s</sub> , O <sub>1s</sub> , N <sub>1s</sub> , and P <sub>2p</sub> , and their relative ratios for the pristine, O <sub>2</sub> -plasma treated, and MPC-grafted PEGDMA samples measured by XPS. ....	21
Table 2. Surface elemental compositions of C <sub>1s</sub> , O <sub>1s</sub> , N <sub>1s</sub> , and P <sub>2p</sub> , and their relative ratios for the pristine, O <sub>2</sub> -plasma treated, and MPC-grafted PUA samples measured by XPS. ....	21
Table 3. Relative ratios of C, O, N, and P with respect to Si for the PEGDMA-MPC mixture and MPC-grafted PEGDMA samples measured by XPS. ....	42
Table 4. Relative concentrations of the functional groups from deconvoluted C <sub>1s</sub> , O <sub>1s</sub> , N <sub>1s</sub> , and P <sub>2p</sub> peaks of the XPS spectra of the untreated, O <sub>2</sub> plasma-treated, O <sub>2</sub> plasma-treated and MPC-coated, and MPC-coated without O <sub>2</sub> plasma treatment samples. ....	58
Table 5. Surface elemental compositions of C <sub>1s</sub> , O <sub>1s</sub> , N <sub>1s</sub> , and P <sub>2p</sub> , and their relative ratios for the untreated, O <sub>2</sub> plasma-treated, O <sub>2</sub> plasma-treated and MPC-coated, and MPC-coated without O <sub>2</sub> plasma treatment samples measured by XPS. ....	60

# 1. Introduction

## 1.1. Research background and motivation

Biofilm formation is caused by the attachment of a small number of bacteria on the surface. The bacterial attachment on a certain surface and bacterial proliferation greatly affect human daily life, the medical industry and the marine industry [1]. For the medical industry, surface contamination by bacteria attachment in catheters, artificial vessels, and implants can lead to inflammation response and infection, which also causes cell necrosis, major mortality in patients, and biological damage (Figure 1, 3) [2].

To solve these problems, the antifouling surfaces have been treated with gases or chemicals such as ethylene oxide gas, hydrogen peroxide gas plasma, hydrogen peroxide, and antibiotics for the anti-attachment and killing of microorganisms in the medical industry [3]. However, the frequent use of chemical treatments makes bacteria chemically resistant, which leads to secondary damage to human life.

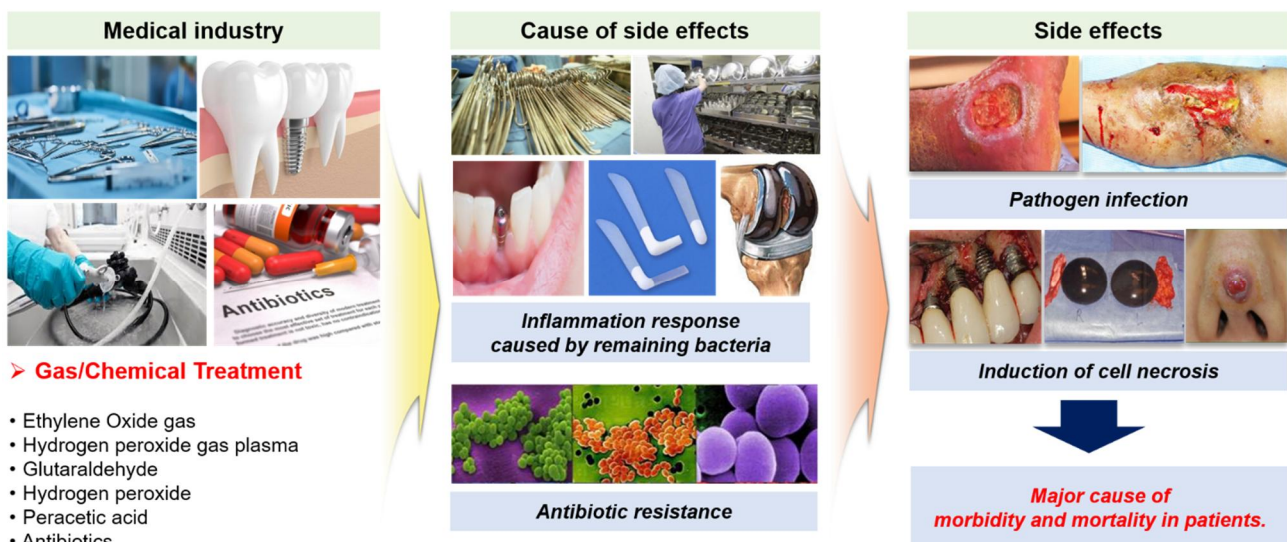


Figure 1. Previous anti-biofouling methods in the medical industry.

For the marine industry, antifouling surfaces are coated with chemicals such as tributyltine paint, copper oxide paint, and mercury paint to prevent microbial adhesion. It has a short-term antifouling performance and is easily detached from the surface due to its low durability. Due to these problems, the cost of surface replacement and fuel loss in the marine industry is increasing and environmental destruction is caused because they have toxic components (Figure 2, 3) [4, 5].

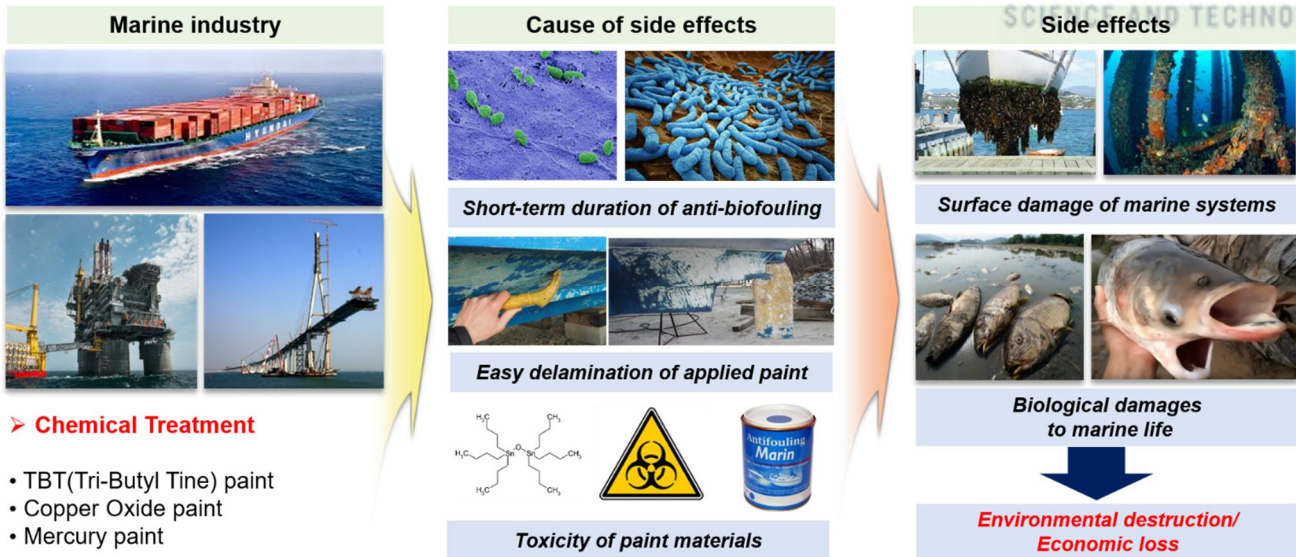


Figure 2. Previous anti-biofouling methods in the marine industry.

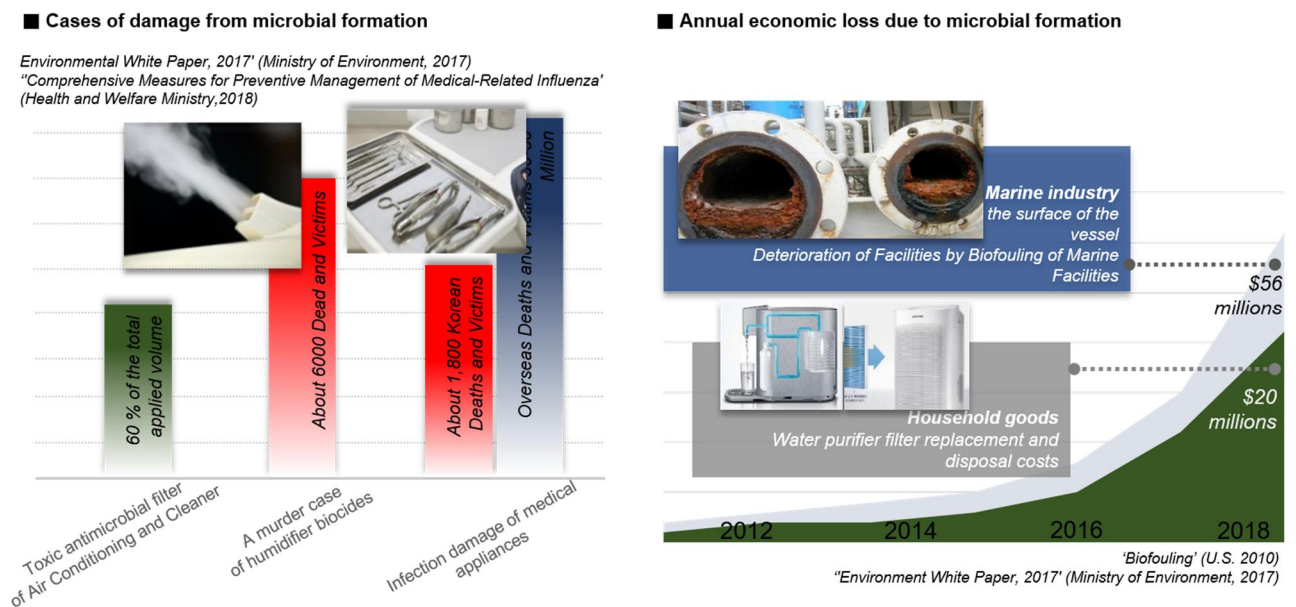


Figure 3. Critical cases due to microbes in the medical field (left) and Economic loss due to microbes in the marine industry (right).

To solve the above-mentioned problem, many researchers have been actively developing the anti-fouling and anti-bacterial surfaces that can effectively inhibit the attachment of bacteria and the formation of biofilm through the chemicals. Traditional anti-biofouling surfaces are generally classified into two types according to the functional mechanism including chemicals and structural anti-biofouling properties [6]. The first type is based on chemicals, which can repel or kill the bacteria on the surface (Figure 4, 5). First of all, the chemicals to prevent bacterial adhesion are as follows. The antifouling materials are hydrophilic, zwitterionic, hydrophobic and smart materials, among which the typical representative materials are PEGylated and zwitterionic substances.



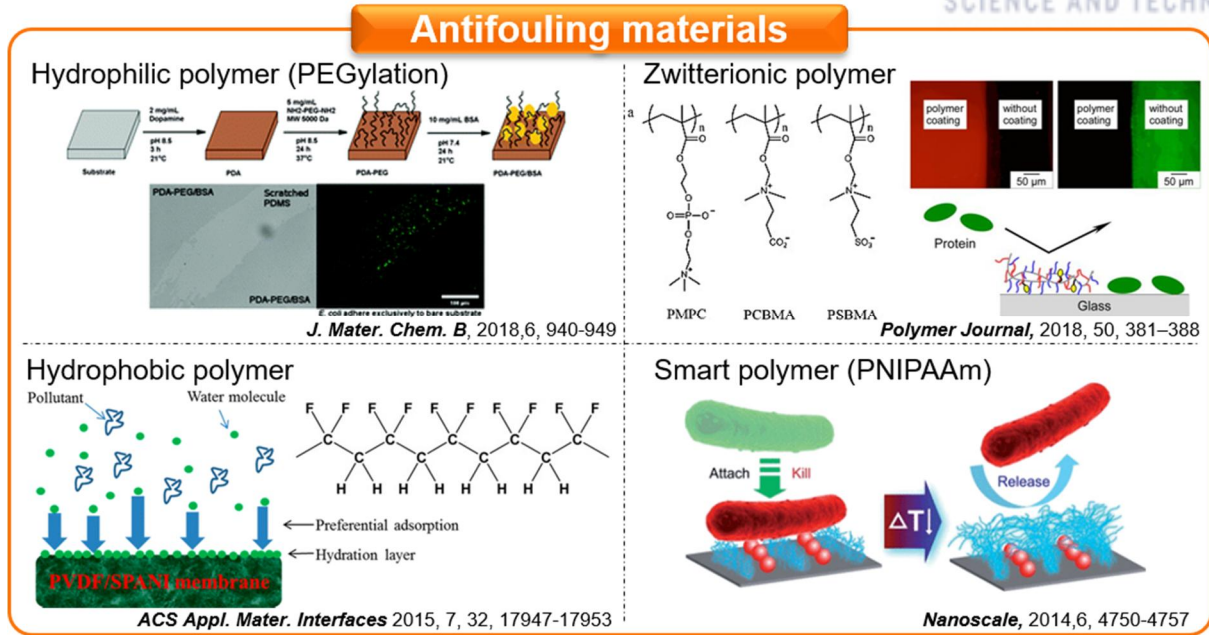


Figure 4. Existing researches on chemical-based antifouling approach.

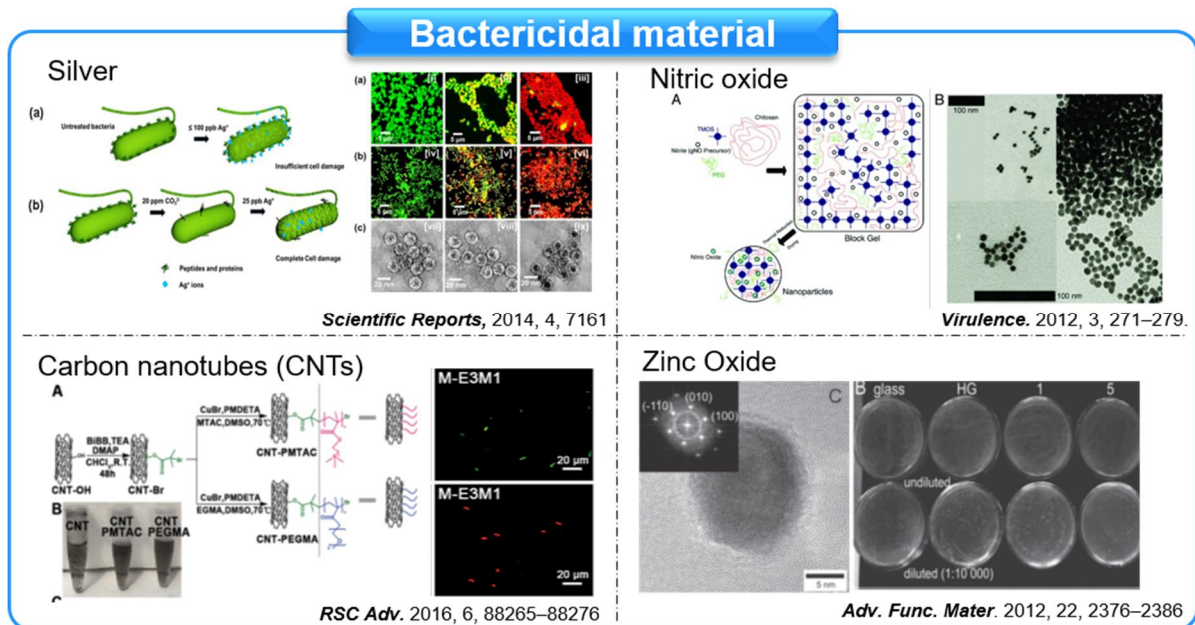


Figure 5. Existing researches on chemical-based bactericidal approach.

PEG is the most representative hydrophilic polymers, has been broadly employed to modify surfaces for antifouling properties [7-10]. The antifouling behavior of PEG-based surfaces is activated by the hydration shell formed by hydrogen bonds between PEG and water molecules in addition to the steric repulsion effect due to flexible chains (Figure 6a) [9, 11]. Zwitterionic materials are biocompatible with anti-biofouling functions and have phosphorylcholine side chains mimicking the hydrophilic group of phosphatidylcholine in the cell membrane such as the typical polybetaines, including poly(2-methacryloyloxyethyl phosphorylcholine) (PMPC), poly(sulfobetaine methacrylate) (PSBMA) and poly(carboxybetaine methacrylate) (PCBMA) (Figure

6b). Also, because zwitterionic material possesses both anionic and cationic groups with overall charge neutrality, they can form hydration shell via electrostatic interactions, which are much stronger than hydrogen bonds, resulting in denser and tighter hydration layer [9]. Compared with PEG, the hydration shell formed by zwitterionic materials is denser and thicker. For PEG molecular chains consist of repetitive units  $\text{CH}_2\text{CH}_2\text{O}$ -, and each unit includes an oxygen atom integrated with one water molecule via hydrogen bonding interactions, while zwitterionic molecule chains consist of equally charged units, and each unit includes a positive charged group and a negative charged group integrated with eight water molecules via at most electrostatic interactions [9]. PEG or MPC are often used as surface grafting materials for planar surfaces based on covalent immobilization, physical adsorption, or gas phase treatment rather than as structural materials [12]. Despite excellent antifouling characteristics, they are easily damaged under physical-chemical and physical stimuli due to molecular-level thickness. This means that the damaged antifouling surface leads to subsequent biofilm formation.

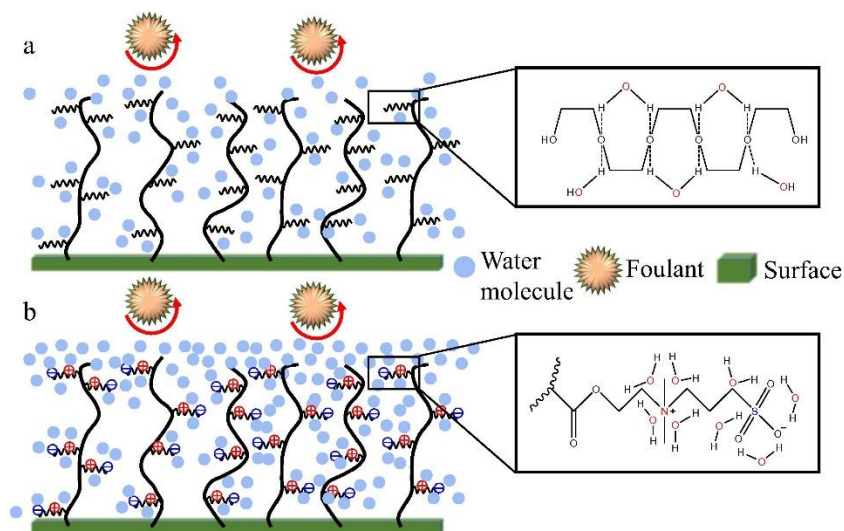


Figure 6. Schematic illustration for the formation of hydration shell. (a) Each unit of the representative PEG materials is integrated with one water molecule. (b) Each unit of the zwitterionic materials is integrated with eight water molecules [9].

Chemicals can interfere with the adhesion of bacteria, but it can also kill bacteria. To kill bacteria, several chemicals are used as follows. Synthetic or antimicrobial agents are used to kill the bacteria. Representative biocidal materials are antibiotics, silver, copper, and nitrates that coat or impregnate the surface coating (Figure 5) [13, 14]. However, it is difficult for actual applications in daily routine, biomedical, marine, and industrial applications because biocide substances have their own limitations including toxicity, high corrosivity, and lack of surface stability. Antibacterial surfaces generally have problems related to the accumulation of dead bacteria and debris, which not only reduces antibacterial efficacy because they prevent the action of antibacterial performance but also form another microbial film by providing it as a nutrient for subsequent bacterial attachment [6].

The second type is based on structures, which can effectively kill the bacteria on the surface. To overcome the limitations of chemical methods for bacteria-repelling and bacteria-killing, researches have been actively performed to physically kill bacteria. Many living creatures in nature minimize bacterial contamination through self-cleaning to maintain their function (Figure 7). In particular, the sterilization effect of the cicada or dragonfly wing is based on the physical surface structure and is continuously cleaned through structural sterilization to maintain a clean surface [15-17].

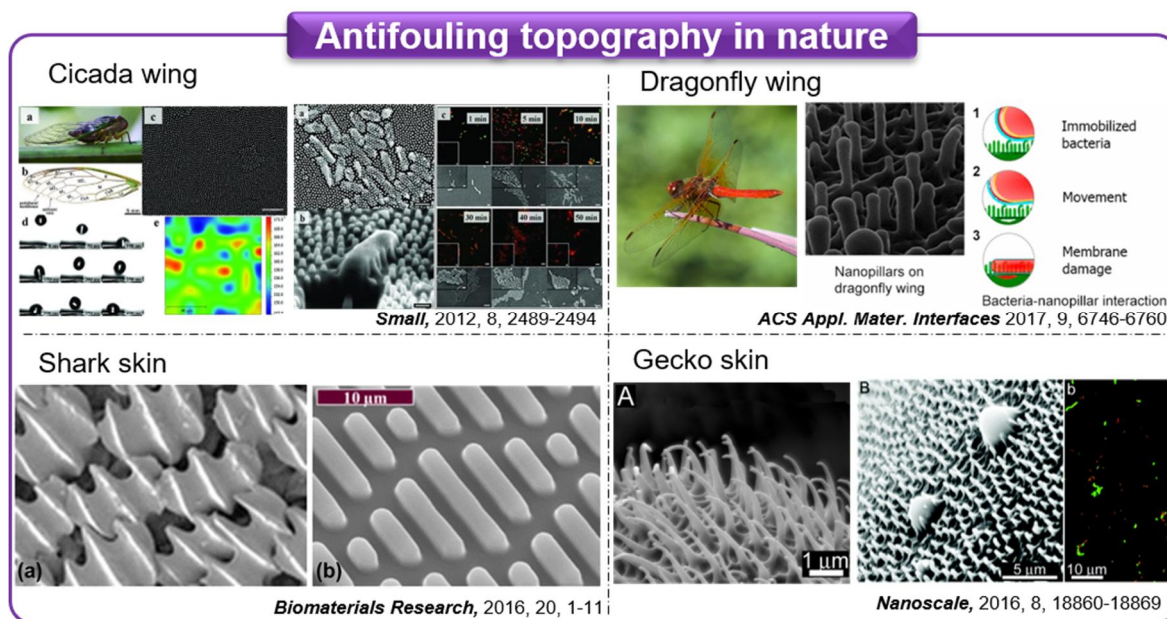


Figure 7. Micro/nanostructures for antifouling in nature.

Recently, research has been underway actively to find that the pointy nanoscale structure mimicking cicada and dragonfly wings can effectively kill bacteria by rupturing the bacterial cell membrane. The bactericidal effects of these surfaces are due to the presence of sharp nanostructures (nano-pillar shaped structure with diameter 50–250 nm, height 80–250 nm, and pitch 100–250 nm) [18]. Such a physical bactericidal method has become an attractive approach to potentially tackle multi-antibiotic resistant bacteria. The bactericidal surface using nanostructures is made of solid inorganic materials such as black silicon and titanium oxide (Figure 8) [19, 20]. However, it is easily damaged by external mechanical stimuli and the accumulation of dead bacteria easily deteriorated antimicrobial performance and has a limitation that is difficult to apply to curved surfaces or large areas. To overcome many of the current limitations of antifouling surfaces, we need a surface that is biocompatible, mechanically durable and applicable to a variety of curved surfaces. In particular, it is required to enable minimization of bacterial attachment and killing the attached bacteria at the same time regardless of the type of bacteria is required.



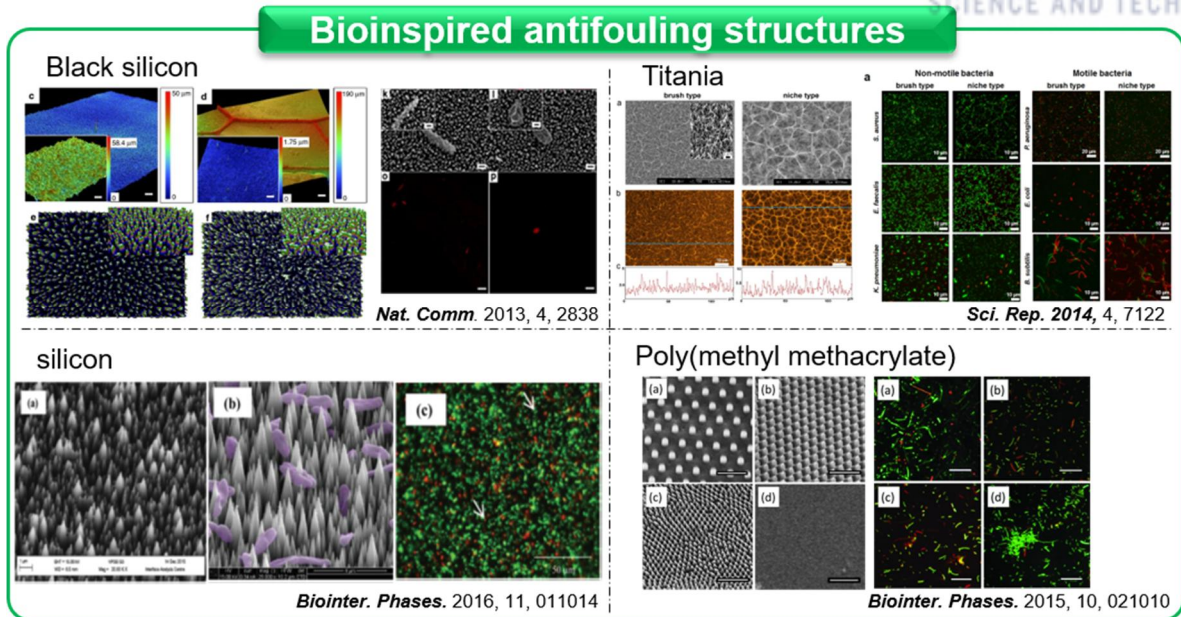


Figure 8. Existing researches on structure-based antifouling approach.

In total, researches have been studied a lot that can interfere with the attachment of bacteria to the surface or kill bacteria. However, the previous studies have many limitations, such as toxicity, durability, and biological damage, because they implement only one function. To overcome the current limitations of the antifouling surface, we need a surface that is biocompatible, mechanically durable and applicable to a wide range of curves. In order to solve problems related to biofilm formation and overcome the limitations of existing antifouling researches, a new strategy of protection with two functions simultaneously, biofilm formation prevention and bacterial killing, is proposed. We have combined the antifouling function and the bactericidal function beyond the traditional one-performance strategy. This strategy uses chemical, mechanical methods, and is based on biocompatible antifouling materials, which fundamentally prevents the formation of early biomaterials formation. And with the fabricated antifouling nanostructures, we can minimize the attachment of bacteria, regardless of bacteria type, and at the same time destroy the attached bacteria.

## 1.2. Research objectives

The purpose of this study is to propose a novel approach to develop an anti-biofouling surface to overcome the limitations of the previous studies. The proposed anti-biofouling surface in this study is biocompatible, mechanical durability, and flexible enough to apply to curved surfaces. It can kill attached bacteria regardless of their type, especially at the same time as it can prevent biofilm formation early on.

The first goal of this study is to select biocompatible materials with antifouling function. Because antifouling and antibacterial materials in the previous studies cause biological damage due to the toxicity, it is important to minimize the toxic problem. Also, the base material should be flexible, because the fabricated surface should be applied to various 3D surfaces. Moreover, the base material should have good processability to fabricate antifouling nanostructures on a large area.

The second goal of this study is to fabricate mechanically durable nanostructures that mimic the nanostructures of a cicada wing that have a bactericidal function. Chemical killing methods can make bacteria having chemical resistance. Therefore, in this study, the structural approach was used to kill bacteria and nanostructures were fabricated with the material having high mechanical strength to ensure the killing of bacteria without resistance.

The third goal of this study is to enhance the antifouling and bactericidal function of the covalently bonded MPC and nanostructured surfaces for long term anti-biofouling durability. The proposed anti-biofouling technology, in this study, has two functions simultaneously.

The final goal of this study is to ensure the long-term anti-biofouling performance of hybrid surfaces with anti-biofouling function, as well as strong resistance to external stimuli.

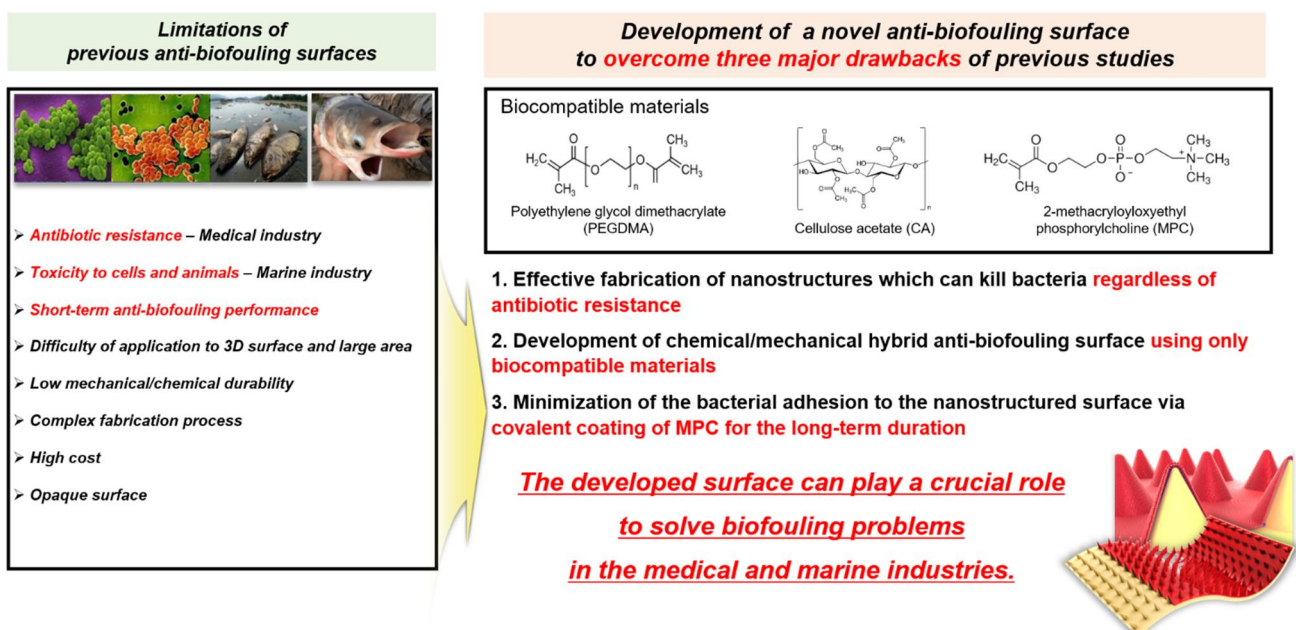


Figure 9. Research objectives.

### 1.3. Research concept and outline

To realize the proposed research objective, materials were chosen which is biocompatible, has high mechanical strength, and has an antifouling function. Using the selected materials, we mimicked the nanostructure of the cicada wing with bactericidal function and fabricated the nanostructure quickly and easily by using UV molding and soft lithography methods. The nanostructure spacing is adjusted and optimized to maximize antimicrobial function. Thinly fabricated surfaces are also very flexible, it can be applied to 3D surfaces or large area. In order to provide antifouling performance once more, amphiphilic material was coated thinly and stably through surface treatment technique, and chemical surface analysis was performed to verify this. To prove the function of the new eco-friendly anti-biofouling surface, gram-negative and gram-positive bacteria were cultured, and qualitative analysis was performed. To prove the durability of the anti-biofouling, we also conducted a long period of incubation and anti-biofouling function tests by external stimuli.

This paper is organized as follows to achieve the research purpose.

- 1) Selection of biocompatible antifouling material
- 2) Fabrication of nanostructures with high mechanical strength for bactericidal performance
- 3) Stable coating of amphiphilic material for maximum antifouling performance
- 4) bacterial test for the durability of long-term anti-biofouling and mechanical

## 2. Functionalized Poly(ethylene glycol) dimethacrylate nanoneedle array

### 2.1. Introduction

Surface contamination due to the development of bacterial films has been a recurring problem in global public health [1]. Extensive efforts have been devoted toward the development of ideal antifouling and antimicrobial materials that can efficiently suppress bacterial adhesion and biofilm formation. Representative examples include surfaces coatings with biocidal substances such as antibiotics, silver, and nitric oxide, which have demonstrated their effective antibacterial capabilities [13, 14, 21]. However, such biocidal materials possess several inherent limitations such as spread of drug-resistant microbes, low biocompatibility, and limited long-term activity [22]. These limitations severely hinder their use in biomedical applications where biocompatibility and long-term activity are critical. To this end, bactericidal surfaces based on nanotopography have been suggested as active biofilm-resistant materials. Recent studies showed that nanopillar structures with sharp tips can effectively kill bacteria by rupturing the cell membranes [16]. This approach has attracted much attention as it enables the active prevention of bacterial colonization based on only surface structural effects without the use of chemical substances. However, such bactericidal surfaces do not have antifouling ability, and therefore accumulate dead bacteria, and eventually lose their activity. Additionally, most previous nanostructured bactericidal surfaces were made of rigid inorganic materials, such as black silicon and titanium oxide [19, 20, 23]. Therefore, they were not only easily damaged under external mechanical stimuli and loss of bactericidal activity, but also could not be applied to nonplanar or curved surfaces. Although polymeric nanostructured surfaces have been reported with poly(methyl methacrylate) (PMMA) or polydimethylsiloxane (PDMS), they are hydrophobic or do not possess intrinsic antifouling properties [24, 25]. Therefore, they have limited antibacterial activity and long-term stability.

Bio-friendly antifouling polymers, such as polyethylene glycol (PEG) and 2-methacryloyloxyethyl phosphorylcholine (MPC), have strong potential as structural materials for nanotopography-based bactericidal surfaces due to their intrinsic antifouling properties and mechanical flexibility [21]. PEG is a biocompatible hydrogel polymer with anti-biofouling properties based on steric repulsion and a hydration layer formed on the surface associated with its hydrophilic nature [7, 26, 27]. MPC is also a biocompatible zwitterionic polymer with antifouling property, which has phosphorylcholine side chains mimicking the hydrophilic headgroup of phosphatidylcholine in cell membranes [28]. The negatively and positively charged groups of MPC can form a dense hydration layer, which efficiently prevents nonspecific protein adsorption, and adhesion of bacteria and mammalian cells [29]. Surfaces treated with PEG or MPC display noticeable fouling-resistance against various microbes compared to untreated surfaces. However, despite their remarkable antifouling properties, they have been barely utilized for the development of nanostructured surfaces with bactericidal properties. Instead, most previous studies have utilized PEG or MPC as a surface grafting material over planar surfaces without nanostructures, based on covalent immobilization, physical adsorption, or gas phase treatment, rather than using them as structural materials [29, 30]. Although the grafted PEG or MPC are covalently tethered to the surfaces,

they typically have a molecular-level thickness. This means that such antifouling layers are mechanically less durable and easily damaged under external physical and chemical stimuli, which could result in the loss of antifouling activity at the damaged sites, and ultimately lead to subsequent bacterial colonization [22]. Considering the fact that surface damages by external stimuli frequently occur with many coating materials, pronounced mechanical durability needs to be established for biofilm-resistant materials. Also, such antifouling coatings on planar surfaces without nanostructures become ineffective against bacteria once the cells adhere to the surface, because even a few adherent bacteria will rapidly proliferate and eventually form a biofilm [31]. Despite much research, few studies have addressed the development of robust and efficient biofilm-resistant materials with pronounced mechanical durability and flexibility, based on the integration of heterogeneous antifouling polymers and nanotopography.

In this study, we present lipid-hydrogel-nanostructure hybrids that integrate heterogeneous biocompatible polymers of MPC and PEG hydrogel, which possess an intrinsic antifouling nature, into a nanoscale topography as biocompatible, flexible, and mechanically robust biofilm-resistant materials. In this approach, we prepared nanoscale needles, the structures of which are entirely made using PEG-based hydrogel. The PEG nanoneedle (NN) is further grafted with zwitterionic polymer of MPC to further maximize the antifouling activity. Based on the unique lipid-hydrogel-nanostructure configuration, the hybrid shows superior dual functionalities of antifouling and microbicidal activity against gram-negative and -positive bacteria. In addition, it maintains robust anti-biofilm activity even when the MPC layer or PEG NN is damaged under external perturbations.



## 2.2. Experimental

### 2.2.1. Fabrication of the MPC-grafted PEGDMA NN hybrids

A Si master with nanohole array was first prepared by photolithography with a stepper (PAS500/700D, ASML, Netherlands). The Si master was treated with a fluorinated self-assembled monolayer solution (trichloro(1H,1H,2H,2H-perfluorooctyl)silane, Sigma Aldrich, USA) for surface hydrophobization. PEGDMA (MW ~ 550, Sigma Aldrich, USA) solutions (80, 90, 100 wt% in deionized (DI) water) with 0.2 wt% of photoinitiator (Irgacure 2959, Sigma Aldrich, USA) were filtered using a syringe filter with a 0.2  $\mu\text{m}$  pore size. Then, a drop of the PEGDMA solution was dispensed onto the master and the drop was covered with a polyethylene terephthalate (PET) film. The PEGDMA drops were cured by UV exposure ( $\lambda = 365 \text{ nm}$ , dose =  $200 \text{ mJ cm}^{-2}$ ) and subsequently removed from the master, which resulted in flexible PEGDMA NN arrays. Subsequently, the samples were cleaned with ethanol and DI water followed by drying in a convection oven. For the MPC grafting, the prepared PEGDMA NN samples were exposed to oxygen plasma for 1 min ( $\text{O}_2$  flow rate: 100 sccm, power: 100 W). Then, MPC (Sigma Aldrich, USA) dissolved in DI water to a concentration of 0.25 mol/L was spin-coated on the samples at 3000 rpm for 30 s, and then dried in an oven at 70  $^{\circ}\text{C}$  for 1 h. Finally, the grafted specimens were washed with ethanol and DI water, followed by drying. PUA (311 RM, Minuta Tech, Korea) specimens were prepared based on the same procedure with the PEGDMA samples.

### 2.2.2. SEM, TEM, AFM, and 3D Micrograph imaging

Scanning electron microscopy (SEM) images of the samples were obtained using a HITACHI S-4800 microscope (Hitachi, Japan). To avoid charging effects, the samples were coated with a Pt layer (~5 nm thick) by metal sputtering (K575X sputter coater, Quorum Emitech, UK). Environmental scanning electron microscopy (ESEM) images of the swollen samples were obtained using Quanta FEG 650 microscope (FEI, USA). Before the ESEM imaging, the samples were submerged in DI water for 18 h. The relative humidity of the ESEM chamber was maintained at 100 % during the imaging (environmental mode). Samples for transmission electron microscopy (TEM) imaging were prepared using focused ion beam (FIB) methods (Helios 450 HP, FEI) with both ion and electron beams. FIB-prepared samples were measured by high-resolution (HR) TEM (JEM-2100, JEOL, Japan). Atomic force microscopy (AFM) images were obtained using a Veeco Multimode V microscope (tapping mode, scan rate: 1.0 Hz, Veeco, USA). 3D micrographs of the samples were obtained with a 3D measurement instrument (NV-3000, Nanosystem, Korea). AFM images of the swollen samples were directly obtained from the submerged samples using a Veeco Nanoscope III microscope (Veeco, USA). Before the imaging, the samples were submerged in DI water for 18 h.

### 2.2.3. Attenuated total reflectance-Fourier transform infrared (ATR-FTIR) spectroscopy measurements

Fourier transform infrared spectroscopy was performed on a Cary 670 (Agilent) instrument with a Ge 45  $^{\circ}$

single reflection attenuated total reflectance crystal (PIKE MIRacle, Germany). The spectra were recorded using Agilent resolution software with an average of 32 scans in the wavenumber range of 650–4000  $\text{cm}^{-1}$  at a resolution of 4  $\text{cm}^{-1}$ .

#### 2.2.4. X-ray photoelectron spectroscopy (XPS) measurements

Surface elemental analysis was carried out by X-ray photoelectron spectroscopy (ESCALAB 250XI, Thermo Fisher Scientific, USA) with an Al  $K\alpha$  source and the employed take off angle was 90 °.

#### 2.2.5. Contact angle measurements

The contact angles (CAs) of the water droplets on various PEGDMA and PUA samples were measured using a drop shape analyzer (SDLAB 200TEZD, FEMTOFAB, Korea) at room temperature (25 °C, relative humidity 50 %). The measurement for each sample was repeated five times at random positions on the specimen to obtain the average CA.

#### 2.2.6. Anti-biofilm assay

To evaluate the antibacterial properties of the PEGDMA and PUA samples, gram-negative *Escherichia coli* (*E. coli*, ATCC25404) and gram-positive *Bacillus subtilis* (*B. subtilis*, ATCC21332) bacteria were purchased from American Type Culture Collection (ATCC, Manassas, VA). Before the anti-biofilm tests, each species was cultured overnight in 5 mL of Luria broth (LB Broth Miller, BD Difco, USA) within a shaking incubator (VS-8480, Vision Scientific, Daejeon, Korea) operating at 37 °C and 200 rpm. Bacterial growth of the cultures was monitored using optical density measurements at 600 nm ( $\text{OD}_{600}$ ) with a GENESYS 20 spectrophotometer (Thermo fisher Scientific, USA) until the  $\text{OD}_{600}$  value reached 0.1(log phase). Then, PEGDMA and PUA samples sterilized by UV exposure and with 70 % ethanol were immersed in the bacterial suspensions followed by incubation for 3, 18, 24 and 30 h at 37 °C. Next, the samples were stained with a fluorescent labeling reagent (live/dead bacterial viability kit, BacLight™, L7012, Molecular Probes, Invitrogen, Grand Island, NY). The stained samples were incubated for 15 min in the dark at room temperature and then rinsed twice with PBS. Subsequently, the samples were examined with a multi-photon confocal microscope (LSM 780 Configuration 16 NLO, Carl Zeiss, Germany). The areal coverage of the cells was determined using Image J software (NIH, Bethesda, MD, USA). A colony-forming unit (CFU) assay was also performed to quantify the antibacterial activities of the samples. Samples of  $1 \times 1 \text{ cm}^2$  were placed in 24-well plates and incubated with 2 mL of the bacterial suspension ( $\text{OD}_{600} = 0.1$ ) for 18 h at 37 °C. After incubation, the samples were rinsed with PBS to remove nonadherent bacteria, transferred to conical tubes containing 1 mL of sterile PBS, and vortexed for 5 min to remove all bacteria from the sample surface. This bacterial solution was then diluted serially and plated on LB agar plates. These plates were incubated for 18 h, and colonies were counted to calculate the CFUs of bacteria grown on the sample surface.

## 2.3. Results and Discussion

### 2.3.1. Fabrication of the MPC-grafted PEGDMA NN hybrids

Figure 10 shows the procedure for the preparation of the MPC-grafted hydrogel nanostructure hybrids. Firstly, the hydrogel NN was prepared by an ultraviolet (UV) replica molding technique with poly(ethylene glycol) dimethacrylate (PEGDMA). PEGDMA not only possesses outstanding antifouling ability and biocompatibility, but also can be rapidly cured by exposure to UV light, which enables a rapid and scalable fabrication of precise nanoscale structures [10, 32, 33]. Previously, PEG-based polymers have been utilized as a grafting material for antifouling coatings, which typically has a molecular-level thickness [34]. Therefore, such PEG-grafted surfaces were mechanically less-durable under external mechanical or chemical stimuli. In contrast to the PEG-grafted surfaces, our NN array was fully made of PEG-based polymer. Therefore, our NN array had high mechanical stability and durability. After preparing the PEGDMA NN array, its surface was covalently tethered with MPC to maximize antifouling performance (Figure 10).

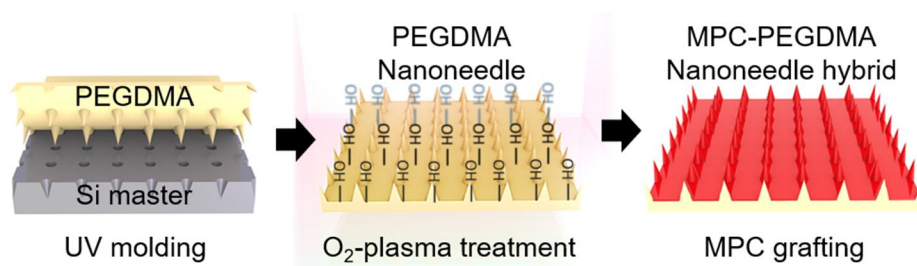


Figure 10. Schematic of the fabrication procedure of the MPC-PEGDMA-nanoneedle hybrid.

The resulting structure was in the form of MPC-PEGDMA-NN triple structural hybrids, of which MPC and PEGDMA would play key roles for maximizing the antifouling activity, whereas the nanotopography would exhibit the bactericidal activity simultaneously (Figure 11, 12). MPC can form a denser hydration layer than PEG, and therefore exhibits better antifouling properties than that of PEG [9]. However, MPC typically has poor mechanical strength and is difficult to use as a structural material for fabricating nanostructures.



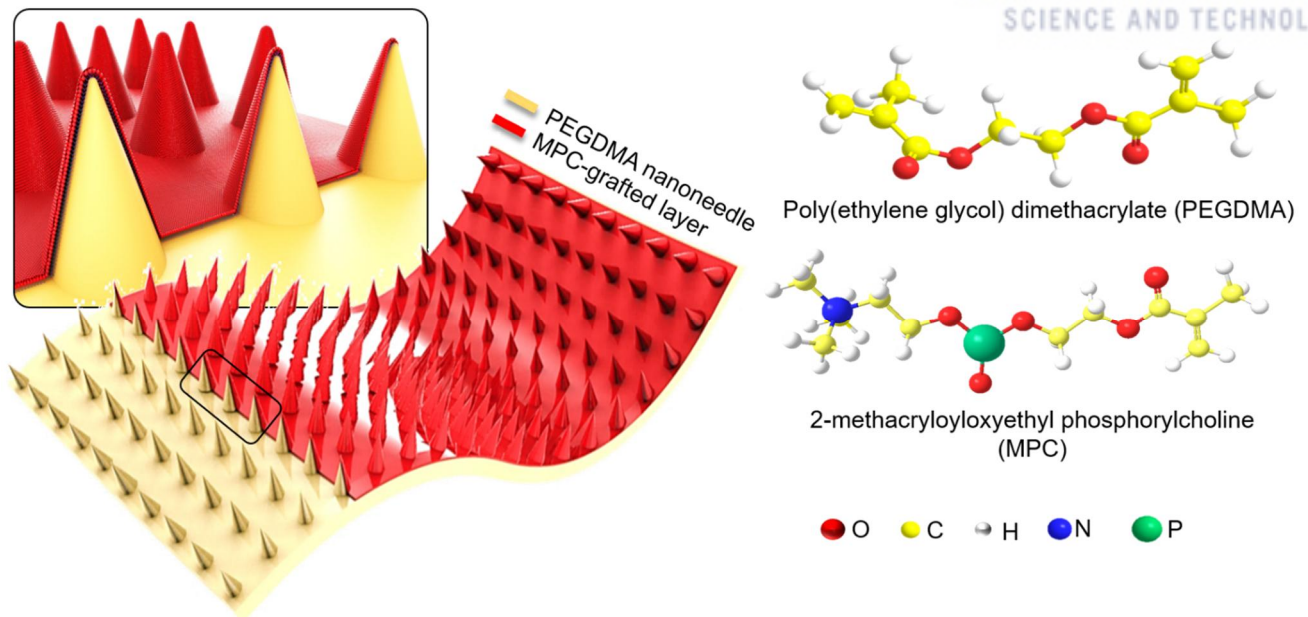


Figure 11. Conceptual illustration of the hybrid structure in which the PEGDMA nanoneedle arrays with covalently tethered zwitterionic MPC molecules are uniformly formed on the surface.

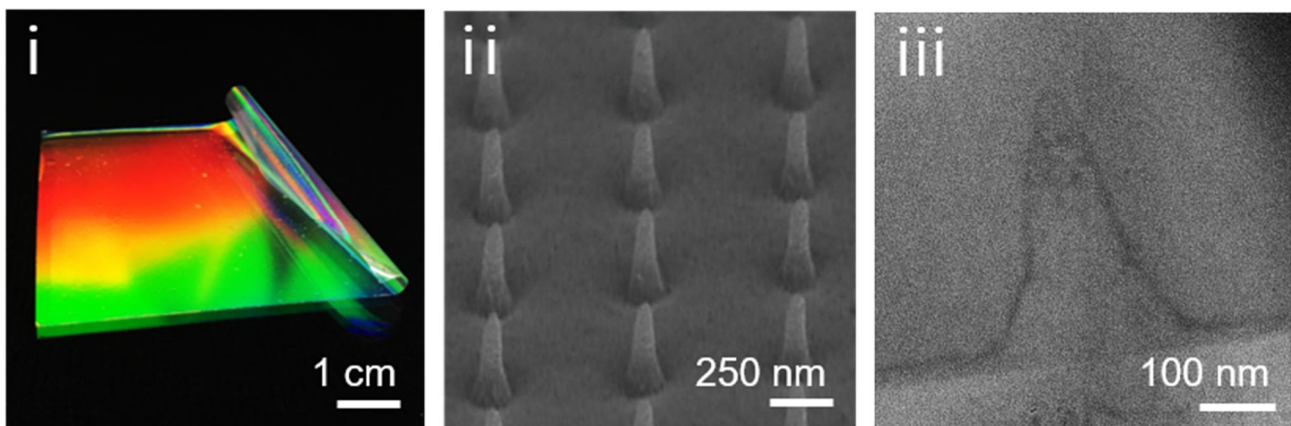


Figure 12. (i) Photograph of the fabricated MPC-PEGDMA-nanoneedle hybrid showing its high flexibility, (ii) an SEM image of the MPC-grafted PEGDMA nanoneedle arrays and, (iii) a TEM image of the cross section of the MPC-grafted PEGDMA nanoneedle. Thickness of the grafted MPC layer is 5 nm.

In contrast, cross-linked PEGDMA has pronounced mechanical strength ( $E$ : 40-50 MPa, Figure 13) and is suitable for nanopatterning [32, 33]. Also, MPC reportedly exhibits reduced biofilm-resistance to *Staphylococcus aureus* that can adhere to human tissue with its unique membrane proteins [1, 35]. This indicates that MPC alone cannot be guaranteed to prevent fouling activity of diverse microorganisms. The co-utilization of PEGDMA and MPC could act synergistically to maximize antifouling activity, while enabling facile nanopatterning and preserving high mechanical strength. Macroscopically, the resulting structure is in the form of an ultrathin and flexible film on which the hybrid nanostructures were uniformly generated (Figure 12-i). The NN was 50 nm in tip diameter, 200 nm in bottom diameter, 300 nm in height, and 500 nm in center-to-center pitch (Figure 12-ii). The transmission electron microscopy (TEM) image in Figure 12-iii represents a thin layer of MPC (~5 nm) uniformly grafted over the PEGDMA NN. The NN structure was also prepared using polyurethane acrylate (PUA) as a control sample. PUA is a UV-curable polymer with a slightly hydrophobic nature (~80°, Figure 14), which is widely utilized for nanopatterning. It does not have intrinsic antifouling properties [36].

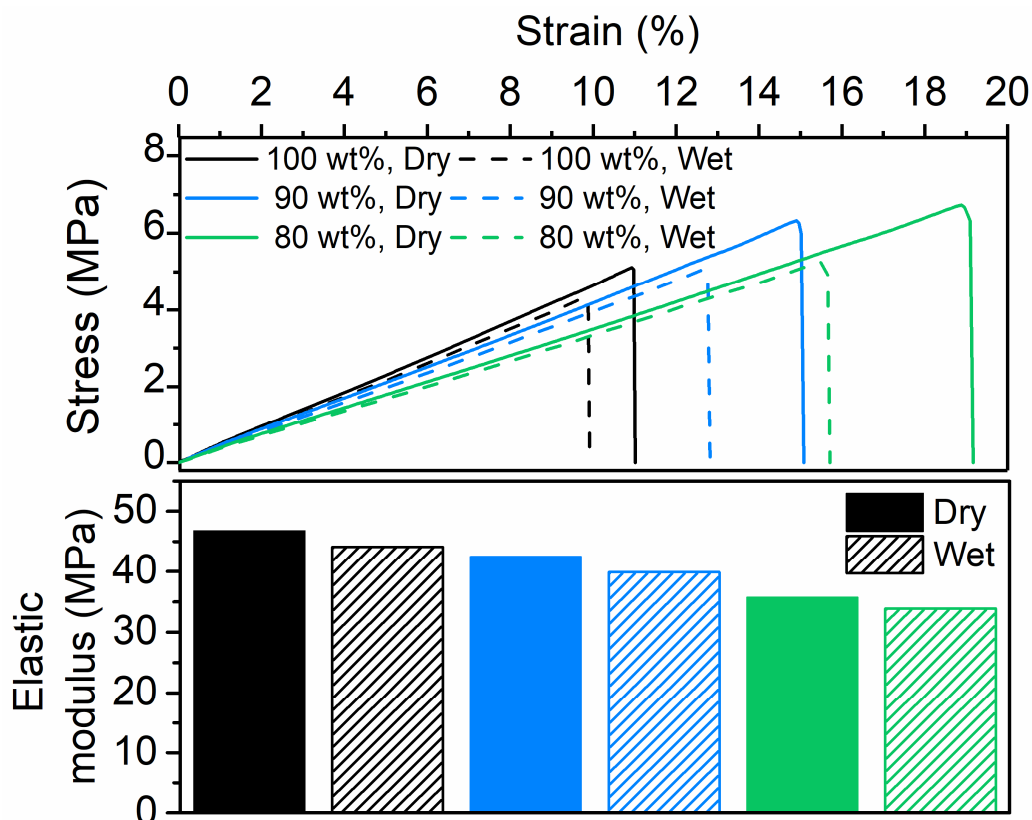


Figure 13. Mechanical properties of the PEGDMA (MW: 550) with different concentrations (80 wt%, 90 wt% and 100 wt%) in the dried and swollen states. The swollen samples were submerged in DI water for 18 h before the measurements.

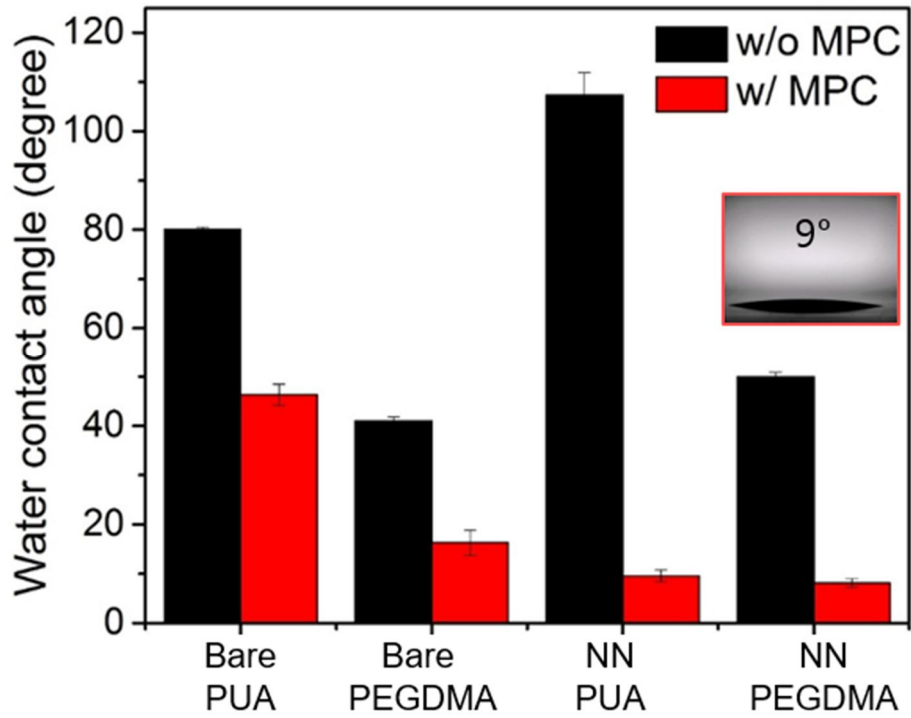


Figure 14. Contact angle measurements of the planar and nanostructured PUA and PEGDMA (80 wt%) samples before and after MPC grafting.

### 2.3.2. Chemical mechanism of the MPC-grafted PEGDMA NN hybrids

To examine the surface chemistry of the hybrids, we performed the attenuated total reflection-Fourier transform infrared (ATR-FTIR) spectra and X-ray photoelectron spectroscopy (XPS) analyses. Figure 15 and 16 show the ATR-FTIR and XPS spectra of the pristine, O<sub>2</sub>-plasma treated, and the MPC-tethered PEGDMA samples (see Figure 17 for the PUA samples). When the PEGDMA sample was treated with the O<sub>2</sub>-plasma, the peak of C=C at 730 cm<sup>-1</sup> vanished (Figure 15), whereas the peaks at 1100 cm<sup>-1</sup> (C-O), 1720 cm<sup>-1</sup> (C=O), and 2840 cm<sup>-1</sup> (CH) were enhanced. When the plasma-treated samples were grafted with MPC, five additional peaks at 970, 1080, 1240, 1620, and 3400 cm<sup>-1</sup> were observed, which corresponded to N<sup>+</sup>-(CH<sub>3</sub>)<sub>3</sub>, P-O, O=P-O<sup>-</sup>, N-H, and NH<sub>2</sub>, respectively [37, 38]. The results indicated that the MPC layer was successfully grafted over the PEGDMA samples. In this approach, it was presumed that the MPC molecules were covalently bonded with the PEGDMA via a plasma polymerization. Upon O<sub>2</sub>-plasma exposure, the alkene of the methacrylate group within the PEGDMA generated radicals and the activated site reacted to the alkene of the methacrylate group of the MPC (Figure 18). Because the alkene is more reactive than other covalent bonds, the alkene of the methacrylate is expected to be the most available covalent bonding site between the MPC and the PEGDMA. To confirm the existence of the MPC molecules on the PEGDMA, surface elemental compositions were analyzed with XPS. XPS analyses revealed that the contents of nitrogen (N) and phosphorous (P) noticeably increased for the MPC-grafted samples compared to the samples without MPC grafting (Table 1 for PEGDMA samples, and Table 2 for PUA samples), which showed that the MPC molecules were successfully grafted over the PEGDMA. In addition to the ATR-FTIR and XPS analyses, the contact angle (CA) measurements were performed on PEGDMA and PUA samples before and after MPC grafting (Figure 14). The MPC-grafted samples exhibited greater hydrophilic wetting properties compared to the pristine samples, which further indicated that MPC was well-tethered on the samples by our approach.

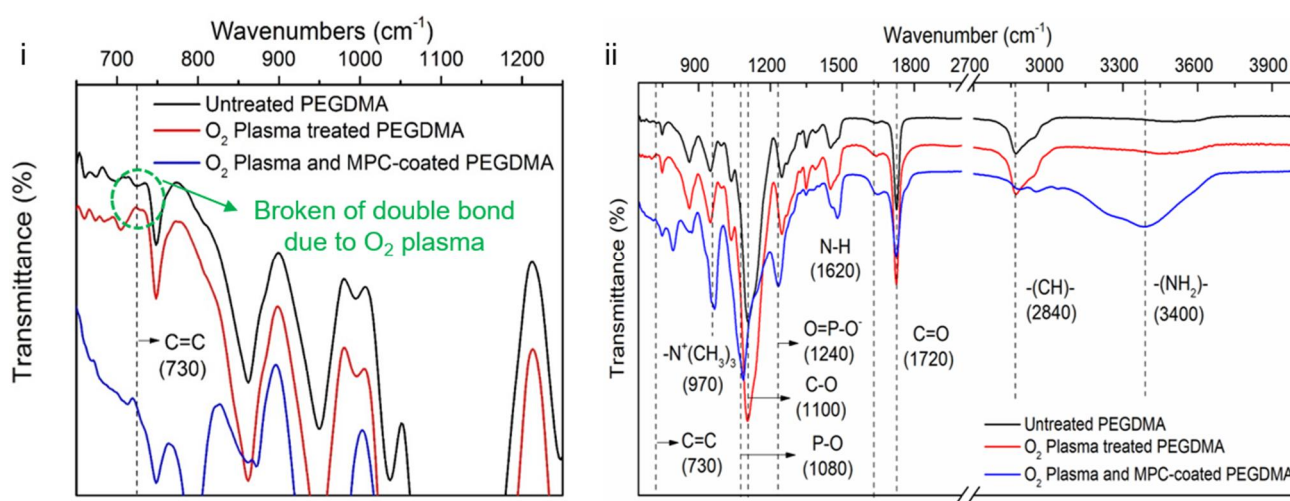


Figure 15. ATR-FTIR spectra of the pristine (i) oxygen-plasma treated, and MPC-grafted PEGDMA samples showing detailed peak at 730 cm<sup>-1</sup>. (ii) oxygen-plasma treated, and MPC-grafted PEGDMA samples in the wavenumber range of 650-4000 cm<sup>-1</sup>.

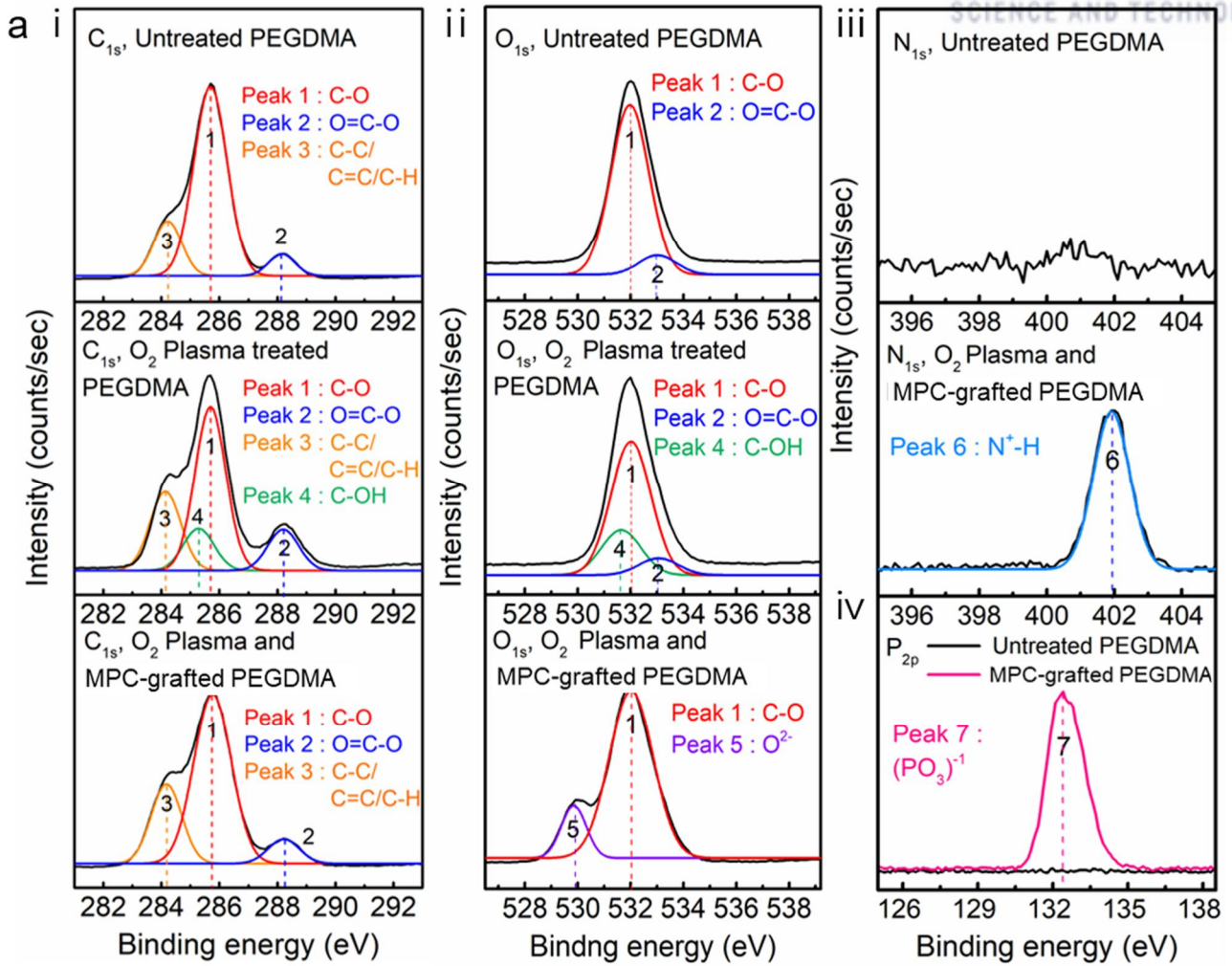


Figure 16. Deconvoluted peaks of (i)  $C_{1s}$ , (ii)  $O_{1s}$ , (iii)  $N_{1s}$ , (iv)  $P_{2p}$  of XPS spectra of the pristine, oxygen-plasma treated, and MPC-grafted PEGDMA samples.



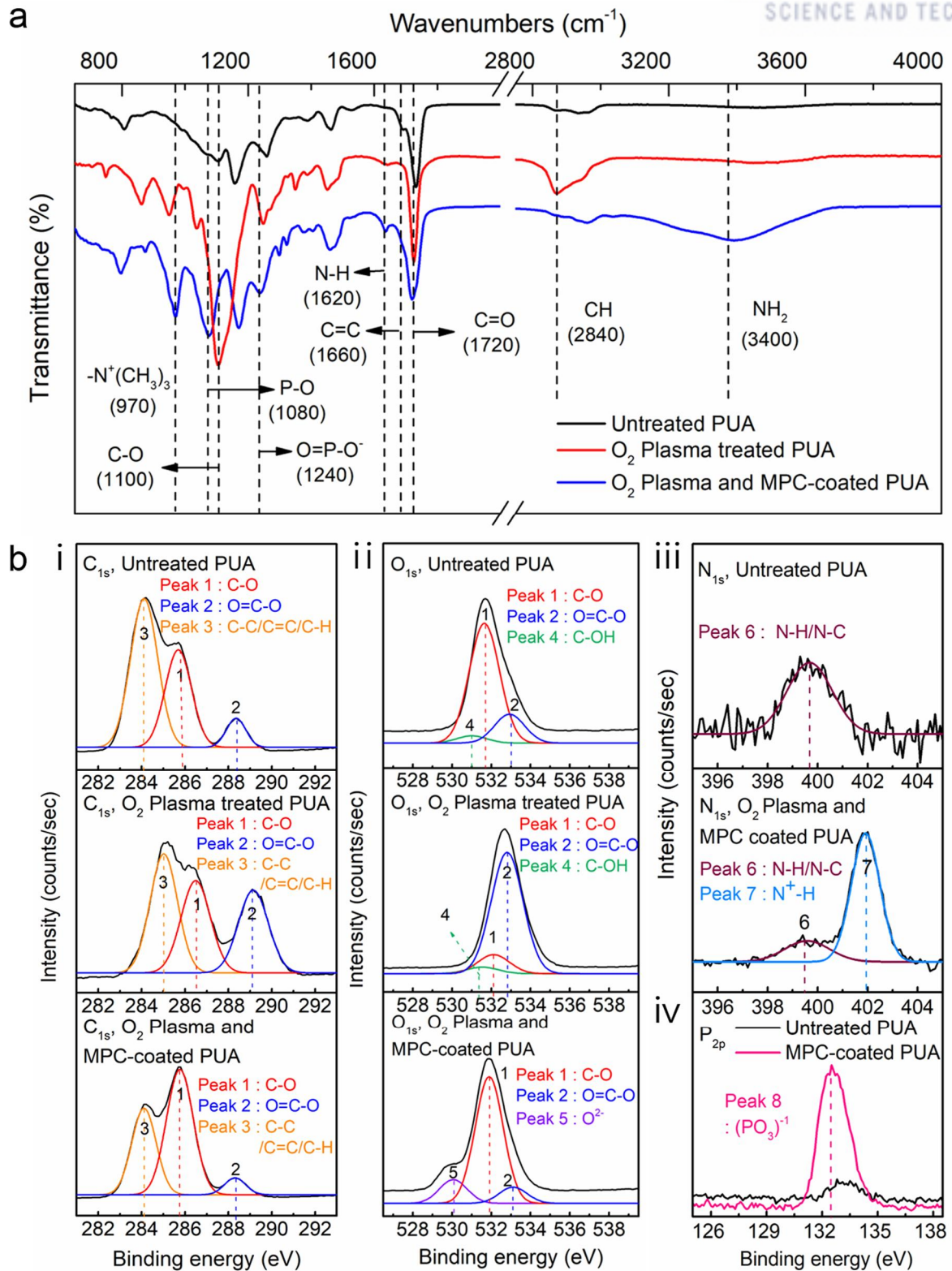


Figure 17. (a) ATR-FTIR spectra of the pristine, oxygen-plasma treated, and MPC-grafted PUA samples in the wavenumber range of 650-4000  $\text{cm}^{-1}$ . (b) Deconvoluted peaks of (i) C<sub>1s</sub>, (ii) O<sub>1s</sub>, (iii) N<sub>1s</sub>, and (iv) P<sub>2p</sub> of XPS spectra of the pristine, oxygen-plasma treated, and MPC-grafted PUA samples.

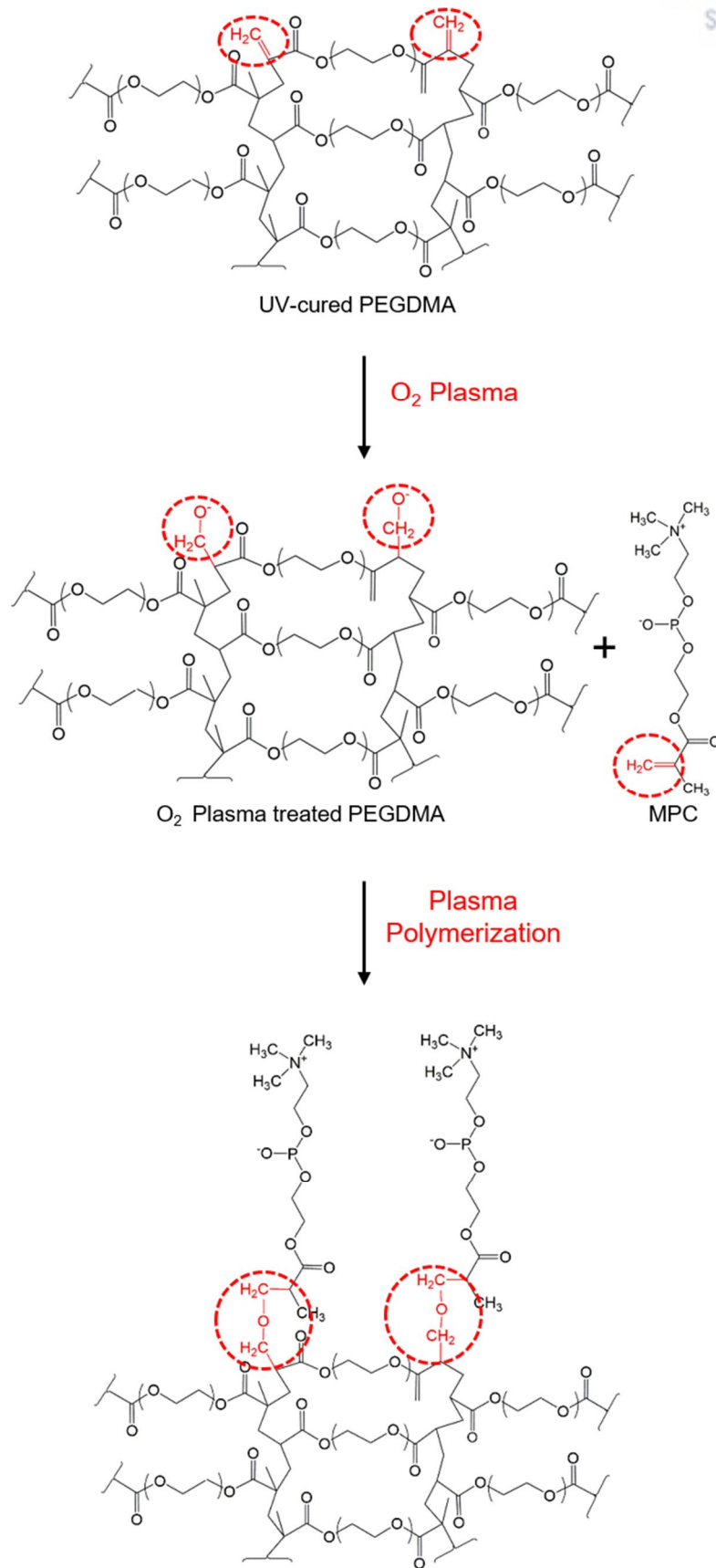


Figure 18. Chemical reaction mechanism of PEGDMA and MPC via oxygen plasma treatment.

Table 1. Surface elemental compositions of C<sub>1s</sub>, O<sub>1s</sub>, N<sub>1s</sub>, and P<sub>2p</sub>, and their relative ratios for the pristine, O<sub>2</sub>-plasma treated, and MPC-grafted PEGDMA samples measured by XPS.

Sample	Atomic composition (%)				Atomic ratio		
	C <sub>1s</sub>	O <sub>1s</sub>	N <sub>1s</sub>	P <sub>2p</sub>	O/C	N/C	P/C
Untreated	66.9	33.0	0.006	0.004	0.493	0.000	0.000
O <sub>2</sub> Plasma treated	63.7	36.3	0.000	0.000	0.571	0.000	0.000
O <sub>2</sub> Plasma and MPC-grafted	60.0	32.4	3.23	4.34	0.540	0.054	0.071

Table 2. Surface elemental compositions of C<sub>1s</sub>, O<sub>1s</sub>, N<sub>1s</sub>, and P<sub>2p</sub>, and their relative ratios for the pristine, O<sub>2</sub>-plasma treated, and MPC-grafted PUA samples measured by XPS.

Sample	Atomic composition (%)				Atomic ratio		
	C <sub>1s</sub>	O <sub>1s</sub>	N <sub>1s</sub>	P <sub>2p</sub>	O/C	N/C	P/C
Untreated	61.900	37.400	0.698	0.002	0.604	0.011	0.000
O <sub>2</sub> Plasma treated	44.300	57.300	1.430	0.000	1.310	0.032	0.000
O <sub>2</sub> Plasma and MPC-grafted	59.100	35.000	2.880	3.020	0.592	0.049	0.050



### 2.3.3. Structural stability properties of the PEGDMA NN

We also examined the swelling behavior and structural integrity of PEGDMA NN under the wet condition. PEGDMA with lower concentrations (wt% in water) exhibited higher swelling ratio (SR), which is defined as  $(W_s - W_d) / W_d \times 100$  ( $W_s$  and  $W_d$  are the weights of the PEGDMA in the swollen and dried states, respectively) (Figure 19). This is because incorporation of water during the photopolymerization reaction can increase the intermolecular distances between monomeric chains [39, 40]. Accordingly, PEGDMA with higher water content (lower concentrations of PEGDMA) has a smaller  $W_d$ , leading to enhanced SR [39]. PEGDMA with higher concentrations had a higher Young's moduli (Figure 13). This is because the water in the PEGDMA decreases the crosslinking density of the hydrogel during the curing process [39]. Figure 20 shows the *in-situ* atomic force microscopy (AFM) images of the swollen PEGDMA NN under the wet condition (see Figure 21 for environmental scanning electron microscopy (SEM) images). Interestingly, PEGDMA NN could maintain their structural integrity even when in the swollen state, presumably due to the relatively high elastic modulus of PEGDMA ( $E$ : 40 – 50 MPa) and low SR.

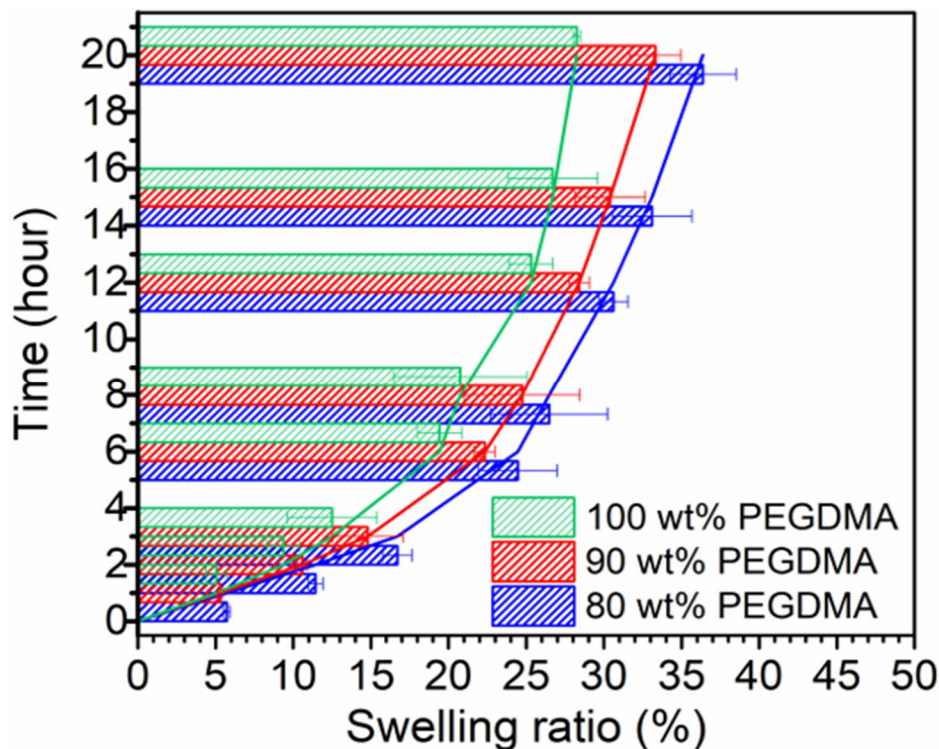


Figure 19. Swelling ratio of the PEGDMA with different concentrations as functions of the water-exposure time.

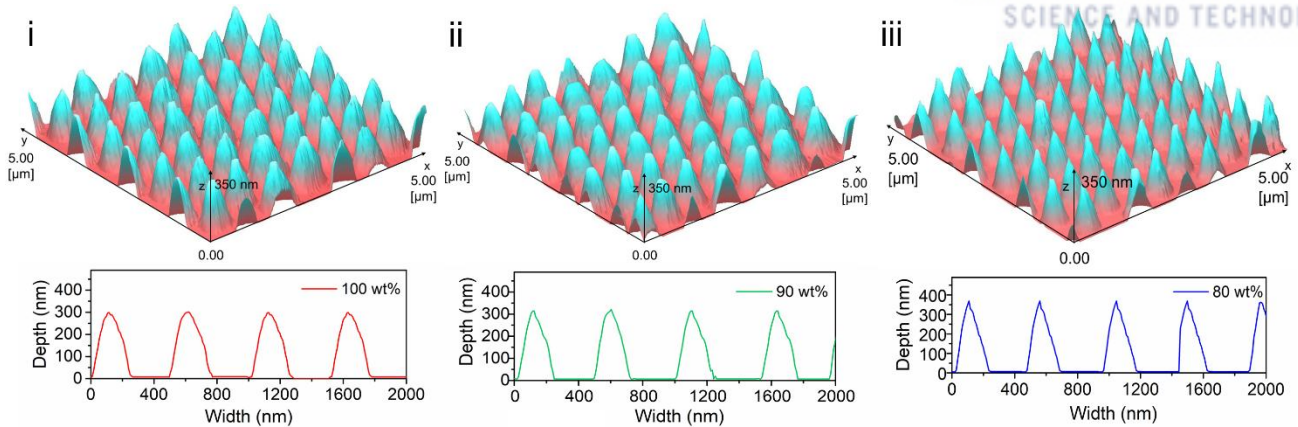


Figure 20. *In-situ* AFM images of swollen PEGDMA NN applied at concentrations of (i) 100 wt%, (ii) 90 wt%, and (iii) 80 wt%. Before the AFM imaging, the samples were submerged in DI water for 18 h. AFM images of the swollen samples were directly obtained from the submerged samples.

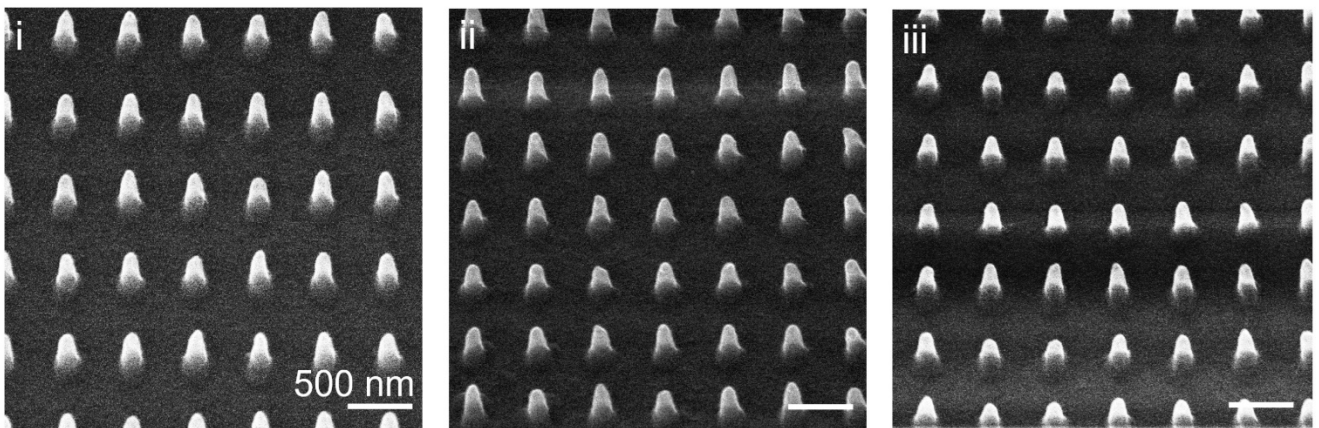


Figure 21. Environmental SEM (ESEM) images of swollen PEGDMA NN applied at concentrations of (i) 100 wt%, (ii) 90 wt%, and (iii) 80 wt%. Before the ESEM imaging, the samples were submerged in DI water for 18 h. The relative humidity of the ESEM chamber was maintained at 100% during the imaging (environmental mode).

### 2.3.4. Anti-biofouling properties of PEGDMA nanoneedle arrays

The bactericidal effect on the NN array decreased with the increase of the array pitch from 500 nm to 4  $\mu\text{m}$  (Figure 22), because bacteria can adhere on the bottom surface, rather than on the NN, for arrays with larger pitches (Figure 23 and 24). Also, NN arrays with a lower AR showed a reduced bactericidal effect than that of the arrays with a higher AR (Figure 23 and 25). *E. coli* on the PEGDMA NN decreased with the decrease of the PEGDMA concentrations, as was the case with the planar surfaces. This illustrated that the PEGDMA NN exhibited dual functions of bacteria-repelling and -killing activities in a simultaneous manner. PEGDMA with a MW of 550 used in this study displayed a relatively high Young's modulus (40–50 MPa, Figure 13) [32, 33, 39]. Therefore, the PEGDMA NN can induce damage on the bacterial membrane with an elastic modulus of 50–200 MPa by penetrating or stretching the cell membrane [16].

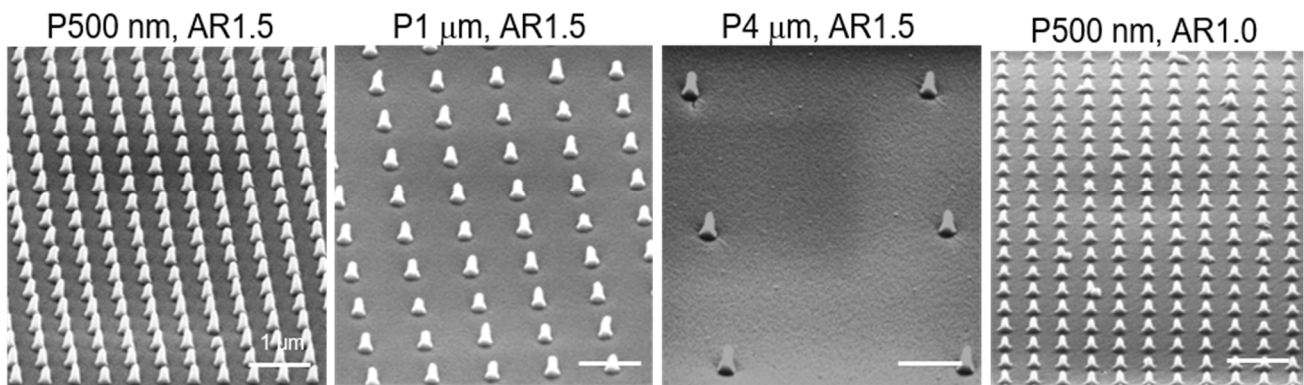


Figure 22. SEM images of the nanoneedle arrays with different pitches (500 nm, 1  $\mu\text{m}$ , and 4  $\mu\text{m}$ ) and ARs (1.5 and 1.0).



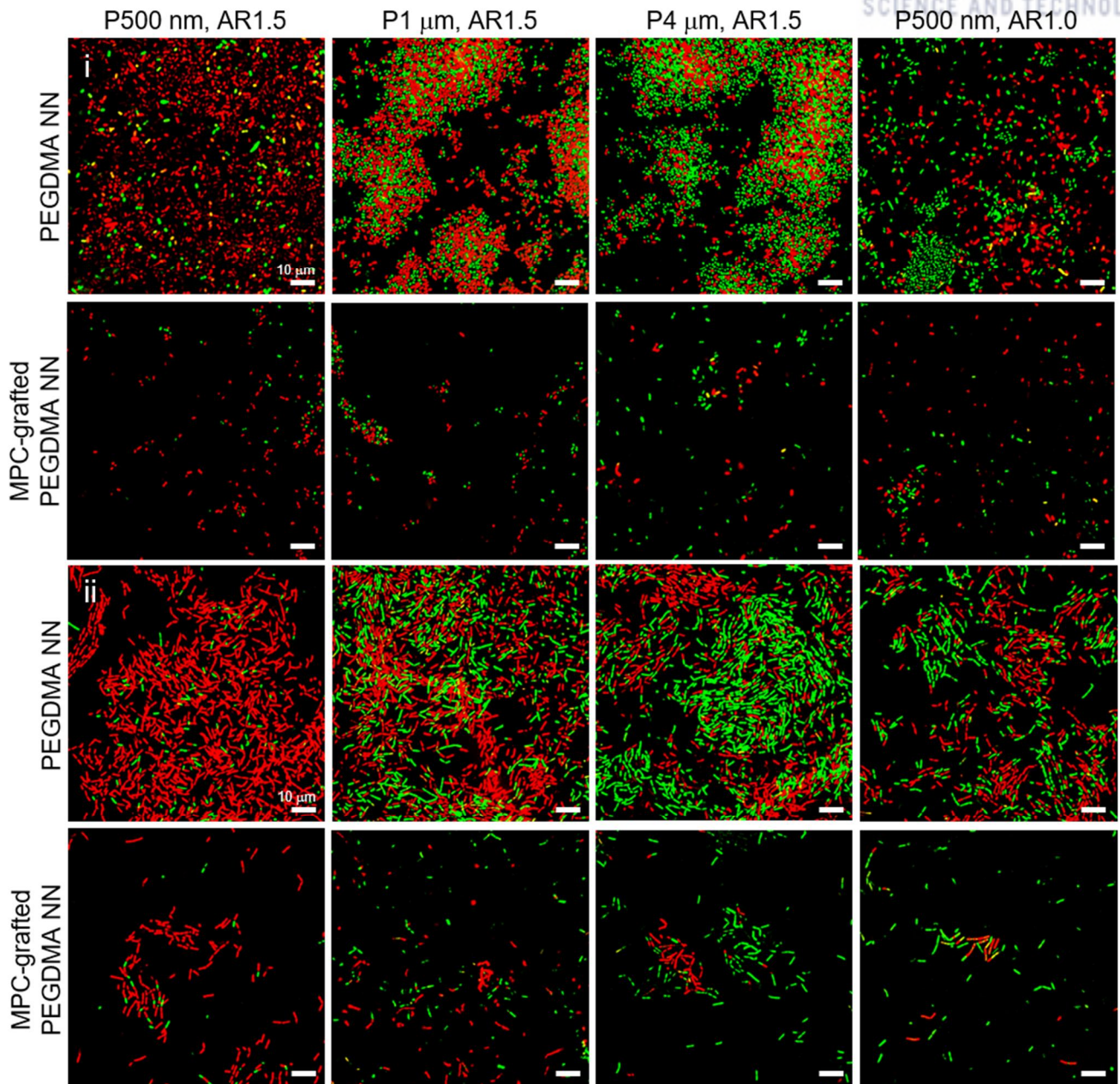


Figure 23. Confocal microscopy images of (i) *E. coli* and (ii) *B. subtilis* cultured on the PEGDMA and MPC-grafted PEGDMA nanoneedle arrays with different pitches and ARs for 18 h. The bacteria were stained with a fluorescent labeling reagent (live/dead bacterial viability kit).

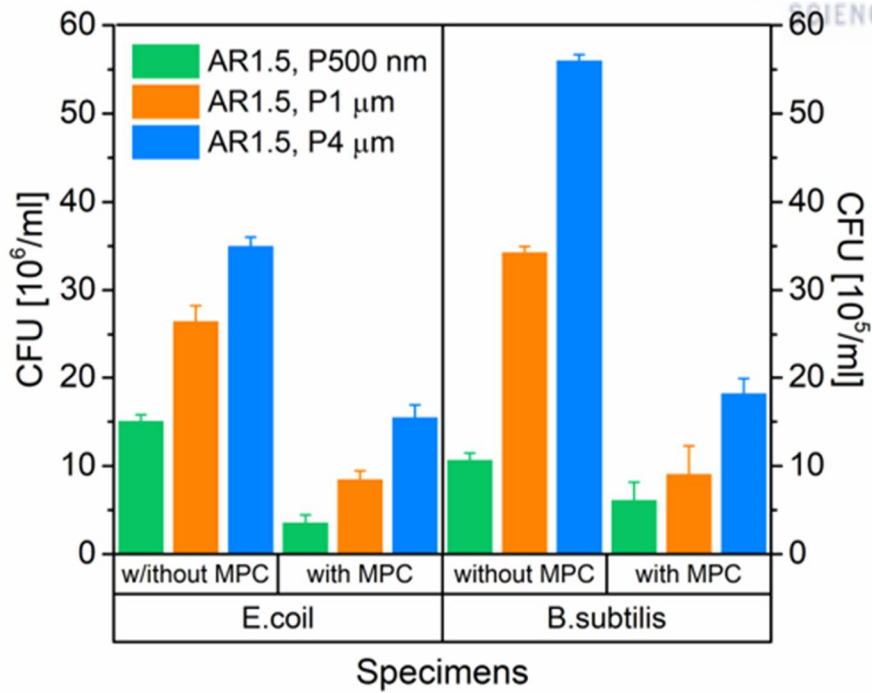


Figure 24. CFU of *E. coli* and *B. subtilis* grown on various PEGDMA samples with different pitches (AR: 1.5).

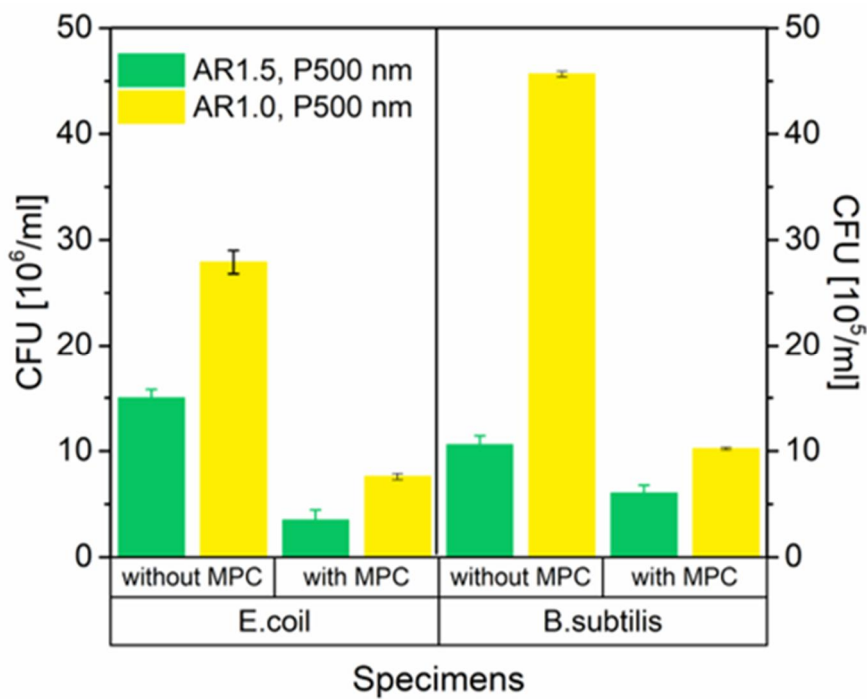


Figure 25. CFU of *E. coli* and *B. subtilis* grown on various PEGDMA samples with different ARs (pitch: 500 nm).



To evaluate the antifouling and antimicrobial activity of the hybrids, we cultured gram-negative (*Escherichia coli*, *E. coli*) and gram-positive (*Bacillus subtilis*, *B. subtilis*) bacteria on various hybrid and control surfaces (Figure 26). After an 18 h incubation, *E. coli* cultured on the planar PEGDMA surface showed notably decreased adhesion compared to that of *E. coli* grown on the planar PUA surface (Figure 26-i), demonstrating the intrinsic antifouling nature of the PEGDMA.

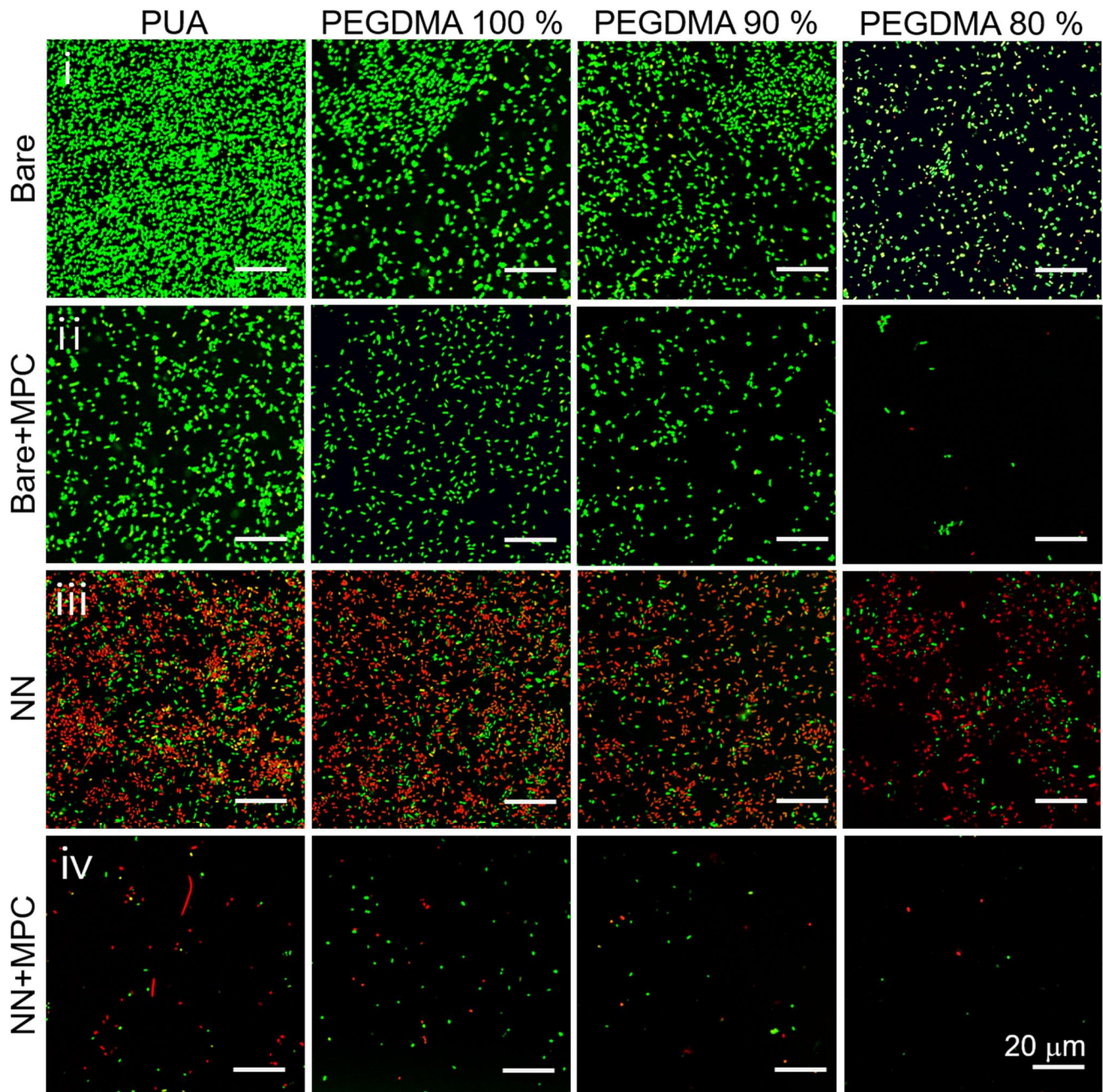


Figure 26. Confocal microscopy images of *E. coli* cultured on the (i) planar, (ii) MPC-grafted planar, (iii) nanoneedle, and (iv) MPC-grafted nanoneedle samples made of PUA, 100 wt%, 90 wt%, and 80 wt% PEGDMA for 18 h. The bacteria were stained with a fluorescent labeling reagent (live/dead bacterial viability kit).

Quantitative analyses of the bacterial area of coverage (Figure 27) and colony-forming unit (CFU) (Figure 28) further confirmed the nonfouling property of the PEGDMA. Bacteria were also cultured on glass for comparisons (Figure 27 and Figure 29). Among PEGDMA samples, lower concentrations of PEGDMA exhibited higher antifouling activity against *E. coli*. Bacteria on 80% PEGDMA (80 wt% PEGDMA and 20 wt% water) showed a much lower area of coverage (Figure 26-i, 27) than those on the PEGDMA with higher concentrations. This was because the lower elastic modulus of the PEGDMA at lower concentrations induced a higher antifouling effect [8, 41]. It is notable that most *E. coli* on the planar PEGDMA surfaces were alive, as evidenced by the green fluorescence emitted (Figure 26-i). This indicated that PEGDMA hydrogel suppressed the bacterial attachment with its antifouling capability, rather than killing the bacteria. When the planar PUA or PEGDMA surfaces were grafted with MPC, the bacterial attachment was remarkably reduced when compared with that of counterpart surfaces without MPC (Figure 26-ii, 27, 28). PEGDMA grafted with MPC exhibited higher antifouling effects than MPC-grafted PUA. It seemed that the MPC-tethered PEGDMA with a higher P/C ratio (0.071) was more effective for the prevention of bacterial attachment compared to the MPC-grafted PUA with a lower P/C ratio (0.05) (Table 1, 2) [42]. This result indicates that the antifouling performance could be amplified by integrating the PEGDMA and MPC into the hybrid configuration. Figure 26-iii shows fluorescence images of *E. coli* cultured on the PUA and PEGDMA NN array. The total number of bacteria on the PUA NN (Figure 26-iii) was much higher than that on the MPC-grafted planar PUA (Figure 26-ii).

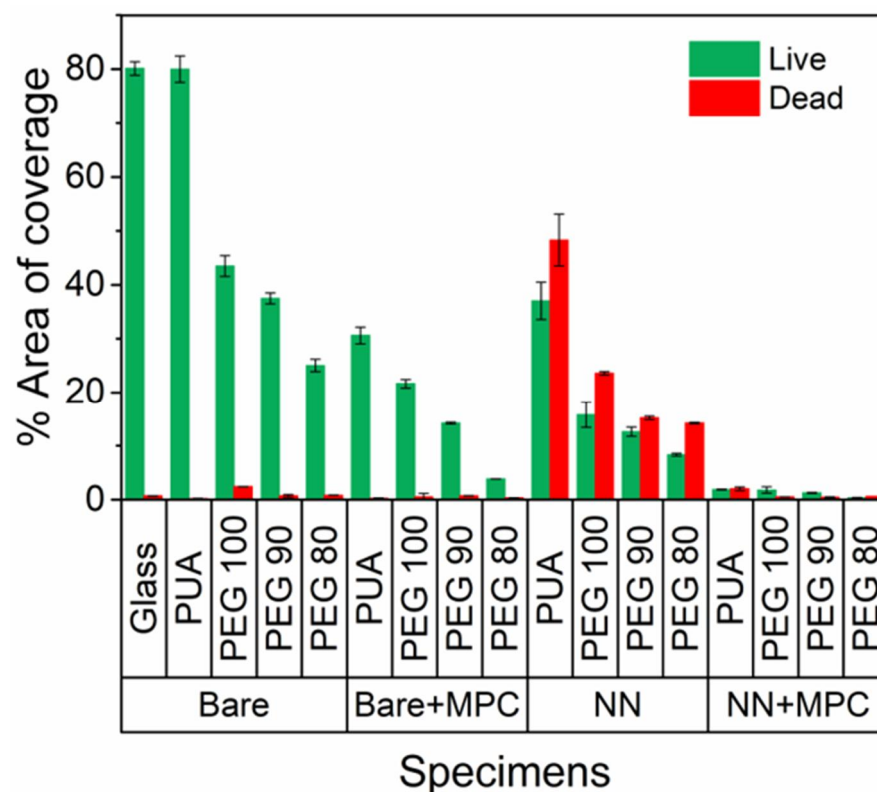


Figure 27. Quantification of area coverage of the live (green) and dead (red) cells cultured on various PUA and PEGDMA samples.



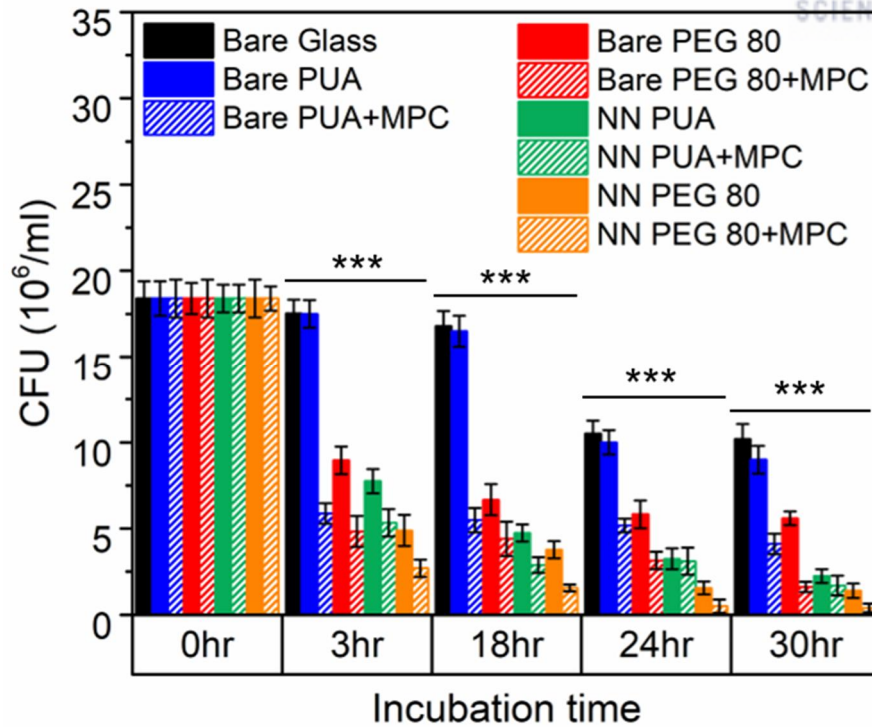


Figure 28. CFU of the *E. coli* grown on various PUA and PEGDMA samples after 0, 3, 18, 24, and 30 h culture. ( $n=9$ ,  $*p < 0.05$ ,  $**p < 0.01$  and  $***p < 0.001$  compared to bare PUA, data was analyzed by a one-way ANOVA).

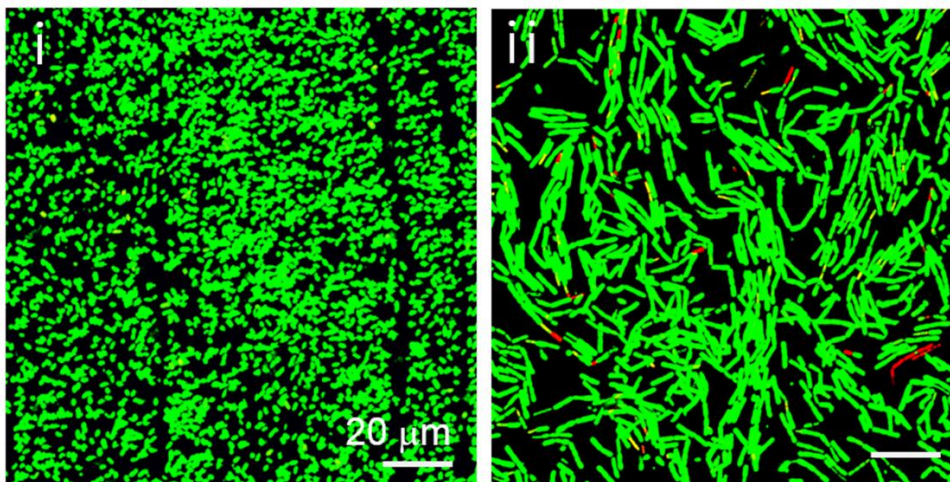


Figure 29. Confocal microscopy images of (i) *E. coli* and (ii) *B. subtilis* cultured on the planar glass for 18 h. The bacteria were stained with a fluorescent labeling reagent (live/dead bacterial viability kit).



However, majority of them were dead cells as indicated by the red fluorescence. This showed that the NN array displayed a strong bactericidal effect based on the physical disturbance of the cell membrane integrity with its nanotopography through the SEM images (Figure 30). To gain more insight into the membrane damage, further investigations of the bacterium-nanoneedles interfaces were performed using transmission electron microscopy (TEM) and FIB. At this stage bacterial membrane is intact and no puncture by the nanoneedles was observed, although bending of the interacting taller nanopillars can be seen at far ends of bacteria as in Figure 31. The induced strong van der Waals forces between bacterial membrane and nanoneedles result in the membrane being stretched when the immobilized bacterium attempts to move on the nanoneedles surface (Figure 32). Therefore, the PEGDMA NN can induce damage on the bacterial membrane with an elastic modulus of 50–200 MPa by penetrating or stretching the cell membrane [16]. AFM images and height profiles of bacterial cells on nanoneedles and flat surface are shown in Figure 33. We also determined that the cells' thicknesses decreased as the cell lysis, indicating that some of the cytoplasm leaked out of the cell.

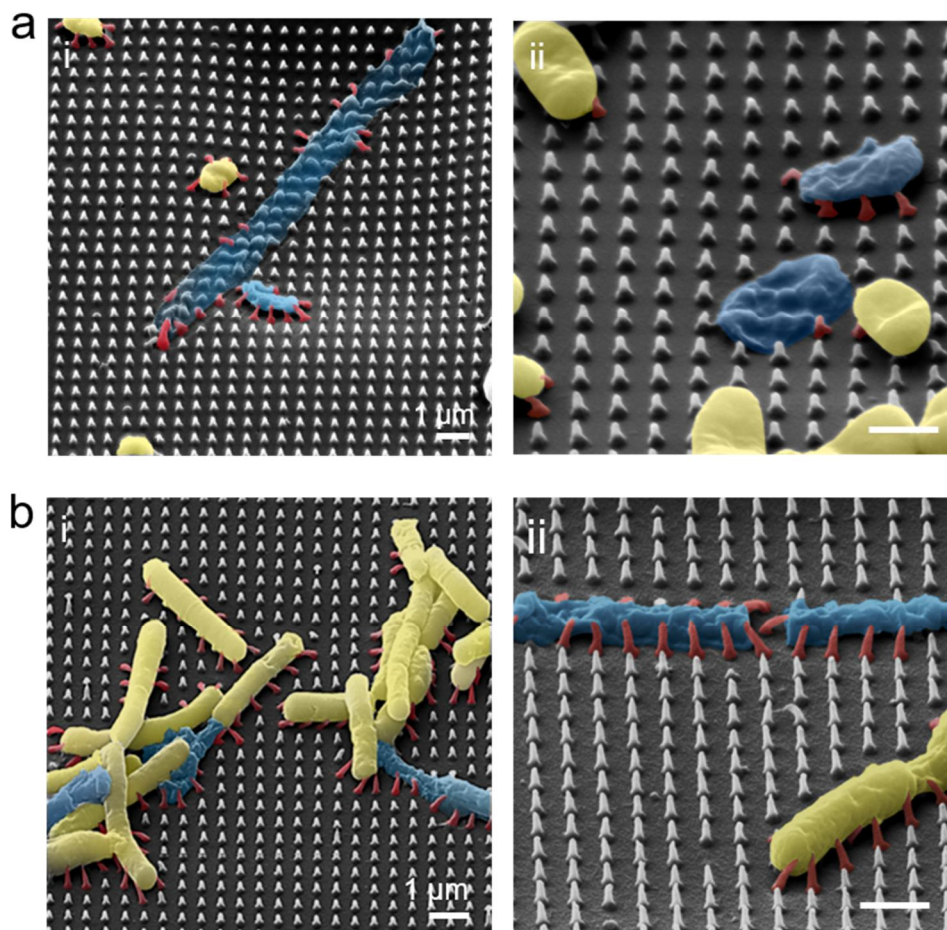


Figure 30. SEM images of (a) *E. coli* and (b) *B. subtilis* cultured on the PEGDMA NN for 18 h.

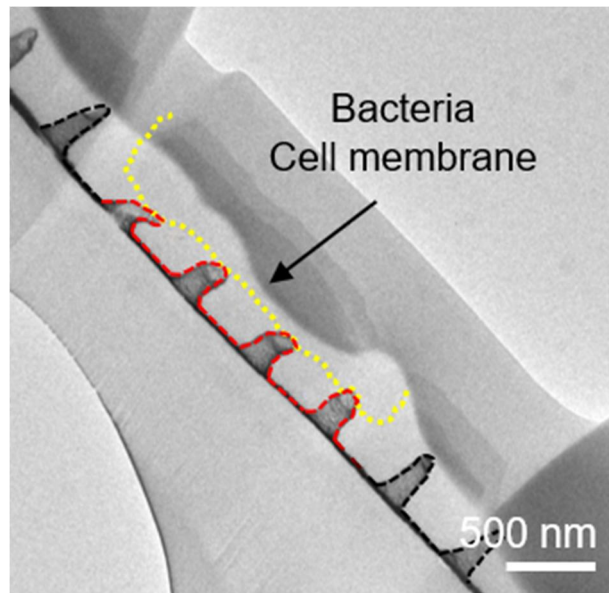


Figure 31. TEM image of *E. coli* cultured on the PEGDMA NN for 18 h.

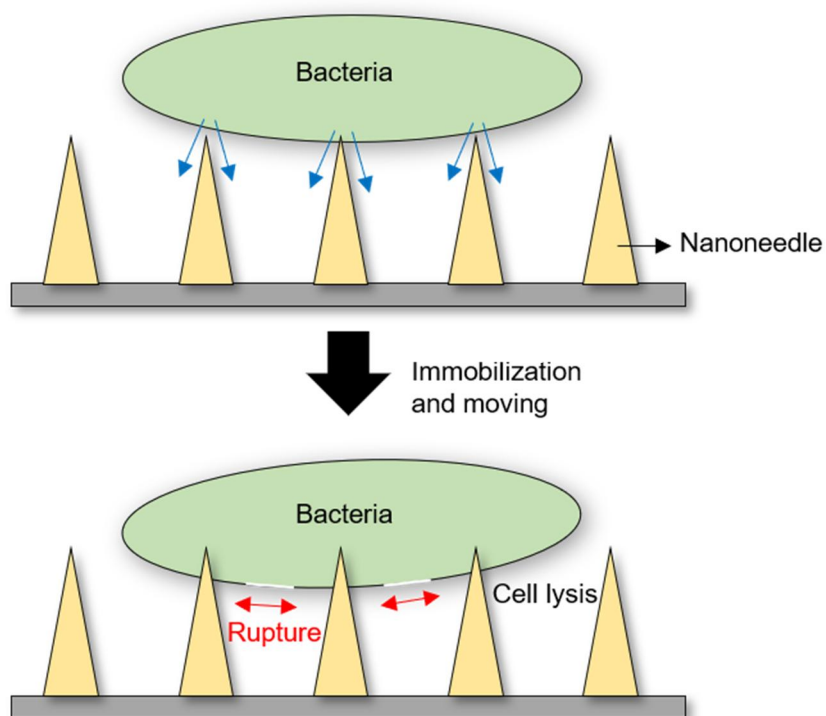


Figure 32. Rupture and lysis of bacterial cell as the bactericidal mechanism of nanoneedle structure.

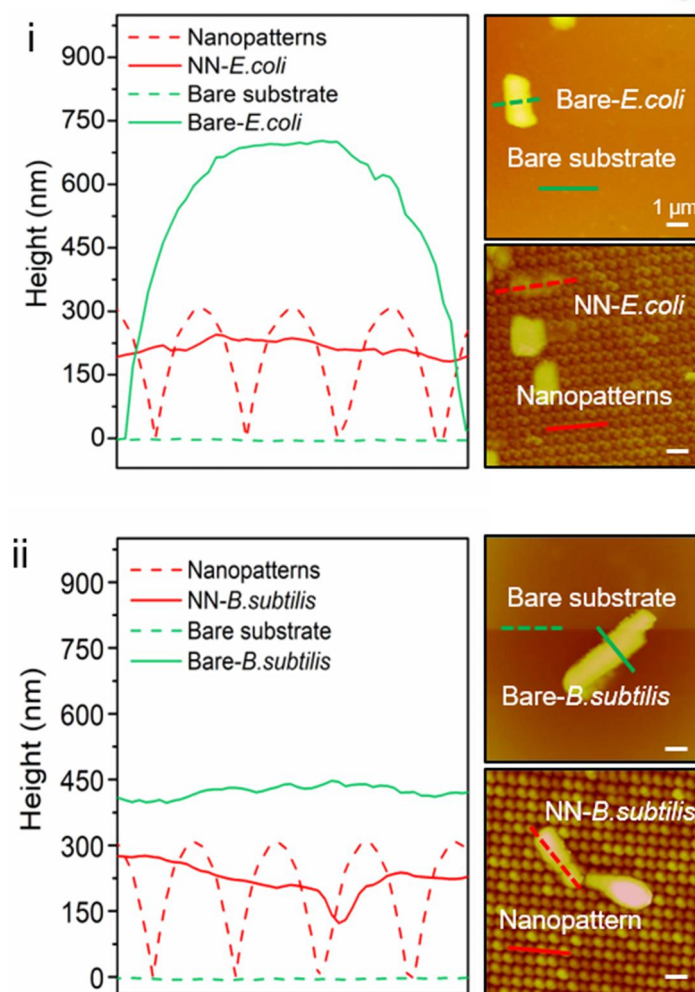


Figure 33. AFM images of (i) *E. coli* and (ii) *B. subtilis* cultured on the planar PEGDMA and PEGDMA NN for 18 h.

As with the PUA NN, the PEGDMA NN also exhibited noticeable bactericidal effects. However, the total number of the adhered *E. coli* on the PEGDMA NN was much lower than that on the PUA NN (Figure 26-iii, 27, 28). When the NN arrays were grafted with MPC, the antifouling and antimicrobial activities were further enhanced (Figure 26-iv, 27, 28). In particular, the MPC-grafted hydrogel NN hybrid made of 80% PEGDMA showed the most superior capability of the anti-biofilm formation. Over the 30 h incubation, the MPC-grafted PEG NN hybrid demonstrated the best performance compared to that of other surfaces (Figure 28). The hybrid surface also maintained good antifouling and microbicidal activities against the gram-positive bacteria *B. subtilis* with overall similar trends for *E. coli* (Figure 34). Among PEGDMA samples, lower concentrations of PEGDMA exhibited higher antifouling activity against *B. subtilis*. Bacteria on 80% PEGDMA showed a much lower area of coverage (Figure 34-i, 35) on the PEGDMA with higher concentrations. MPC grafted PEGDMA exhibited higher antifouling performance than MPC-grafted PUA (Figure 34-ii, 35). It seemed that the MPC-tethered PEGDMA was more effective for the repelling of bacterial attachment compared to the MPC-grafted PUA. The majority of them were dead cells as indicated by the red fluorescence (Figure 34-iii, 35). This showed that the NN array displayed a strong bactericidal effect based on the physical disturbance of the cell membrane



integrity with its nanotopography. When the NN arrays were grafted with MPC, the antifouling and antimicrobial activities were further enhanced (Figure 34-iv, 35, 36). In particular, the MPC-grafted NN hybrid made of 80% PEGDMA showed the most superior capability of the anti-biofilm formation. Over the 30 h incubation, the MPC-grafted PEG NN hybrid demonstrated the best performance compared to that of other surfaces (Figure 36).

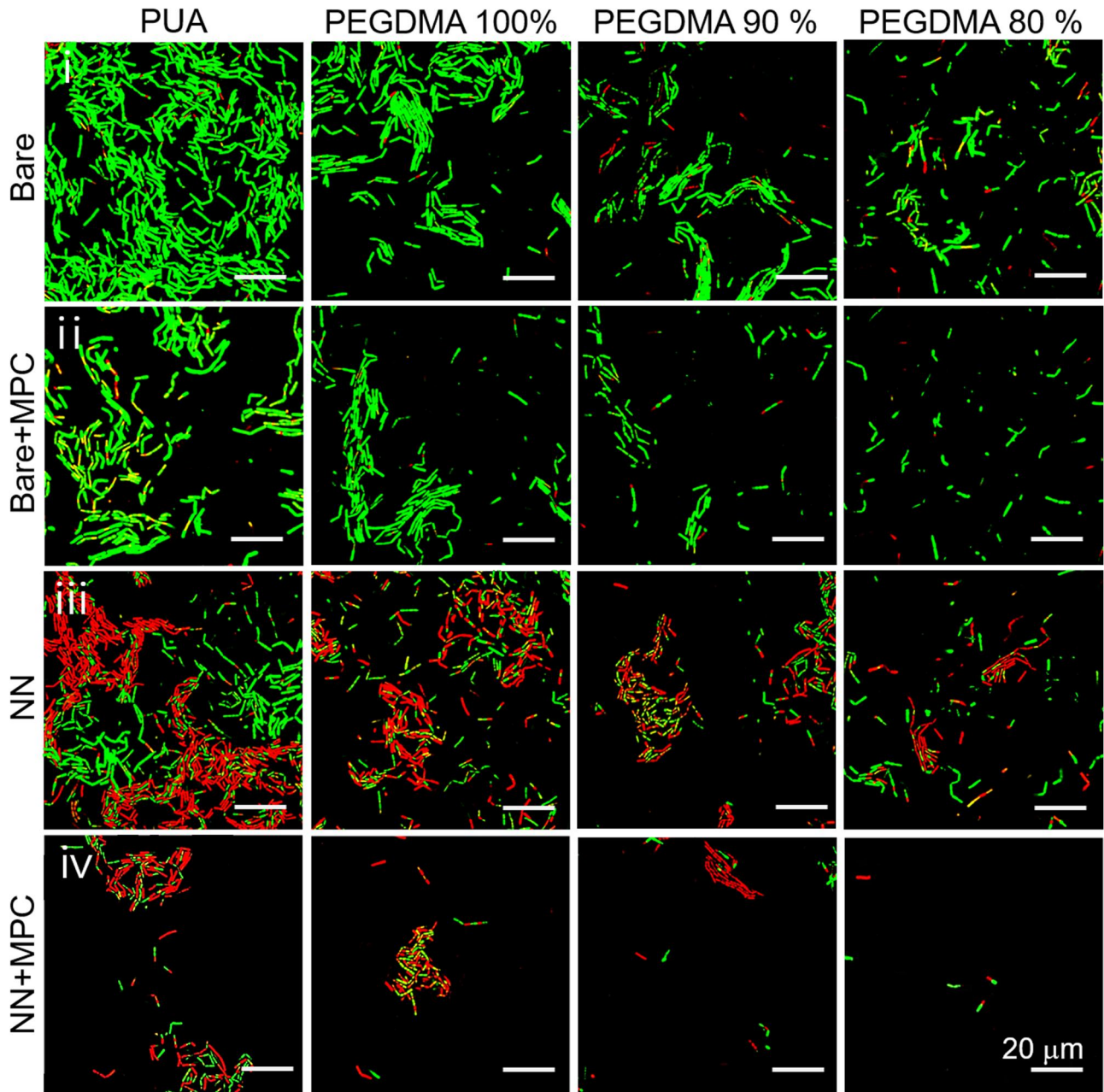


Figure 34. Confocal microscopy images of *B. subtilis* cultured on the (i) planar, (ii) MPC-grafted planar, (iii) nanoneedle, and (iv) MPC-grafted nanoneedle samples made of PUA, 100 wt%, 90 wt%, and 80 wt% PEGDMA for 18 h. The bacteria were stained with a fluoresce labeling reagent (live/dead bacterial viability kit).

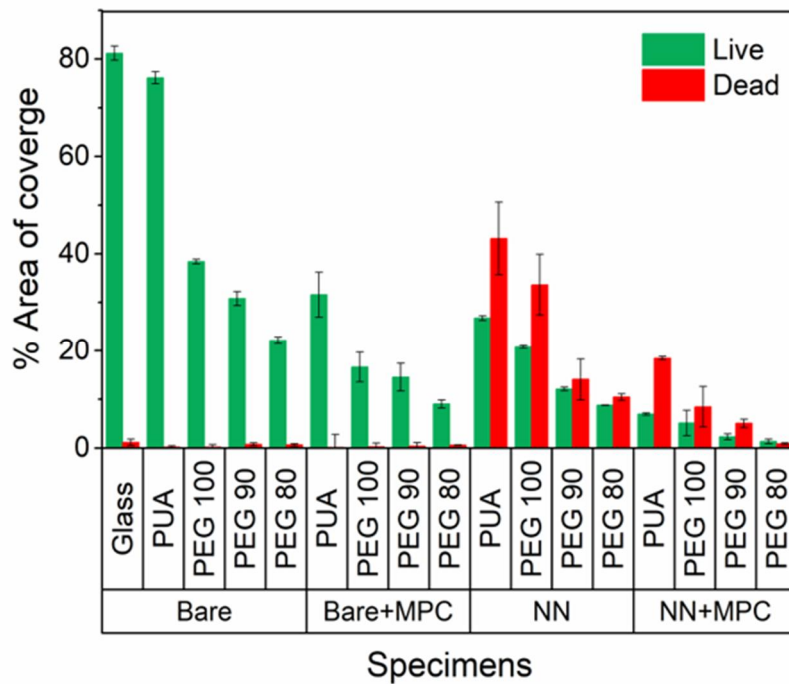


Figure 35. Quantification of area coverage of the live (green) and dead (red) cells cultured on various PUA and PEGDMA samples.

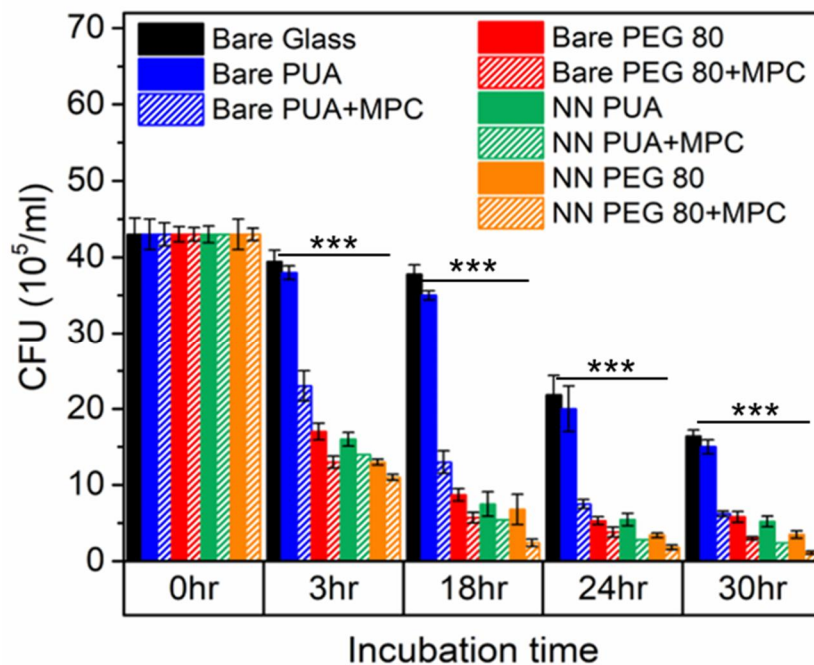


Figure 36. CFU of *B. subtilis* grown on various PUA and PEGDMA samples after 0, 3, 18, 24, and 30 h culture. ( $n=9$ , \*  $p < 0.05$ , \*\*  $p < 0.01$  and \*\*\*  $p < 0.001$  compared to bare PUA, data was analyzed by a one-way ANOVA).

### 2.3.5. Durability properties of MPC-PEGDMA-NN hybrid by external stimuli

The MPC-PEGDMA-NN hybrid was designed to not only maximize the dual functions of the antifouling and bactericidal activities, but also preserve the anti-biofilm formation capability even if the hybrid structures are damaged under external perturbations. To examine its robustness of the biofilm-resistance capability, we prepared MPC-grafted PUA and PEGDMA NN hybrids having damaged regions by mechanical scribing (Figure 37a, 38a). The defect was  $\sim 20\ \mu\text{m}$  in width and  $\sim 60\ \mu\text{m}$  in depth. Therefore, the MPC layer and NN structures were completely destroyed on the sites. Subsequently, we cultured the *E. coli* and *B. subtilis* on the surfaces. The *E. coli* and *B. subtilis* cultured on the MPC-grafted PUA NN showed a significant colonization along the damaged site as shown in Figure 37b. This is because the MPC layer and PUA NN were totally damaged, and the underlying bare PUA backing layer without anti-bacterial activity was exposed to the bacteria, allowing their attachment and subsequent proliferation. In contrast, the *E. coli* and *B. subtilis* showed significantly lower adhesions at the defect sites of the PEGDMA hybrid surface (Figure 38b). This is because even when the MPC and PEGDMA NN are damaged, the underlying PEGDMA backing layer still could act as an effective antifouling material. A slightly higher number of bacteria were attached on the damaged site compared to the non-damaged region, which indicated that the MPC-PEGDMA-nanostructure hybrid has the most superior antifouling activity.

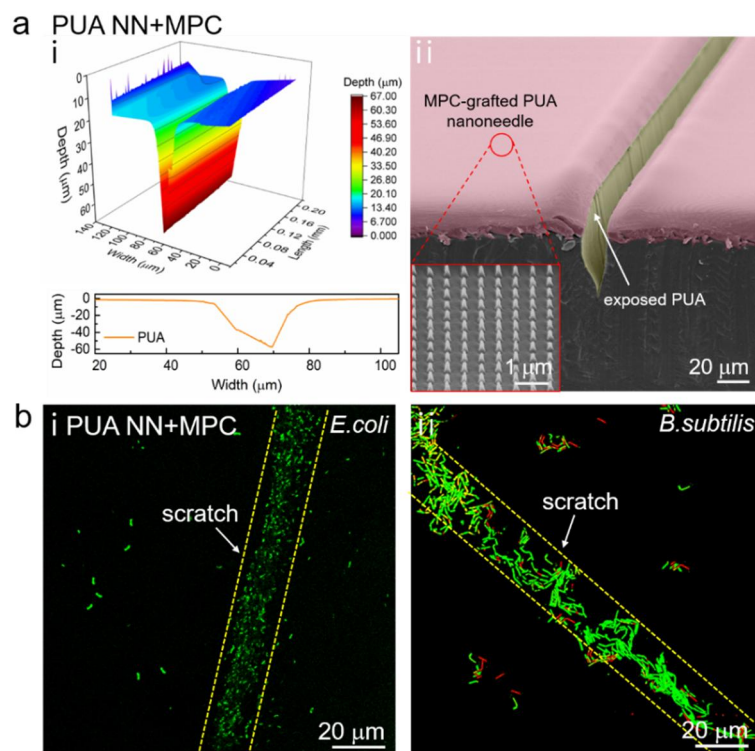


Figure 37. (a) (i) (top) 3D micrograph and (bottom) cross-section, and (ii) SEM images showing the damaged MPC-PUA-NN. False colors were used to emphasize the damaged sites. (b) Confocal fluorescence microscopy images of the (i) *E. coli* and (ii) *B. subtilis* grown on the damaged MPC-PUA-NN (culture hour: 18 h).

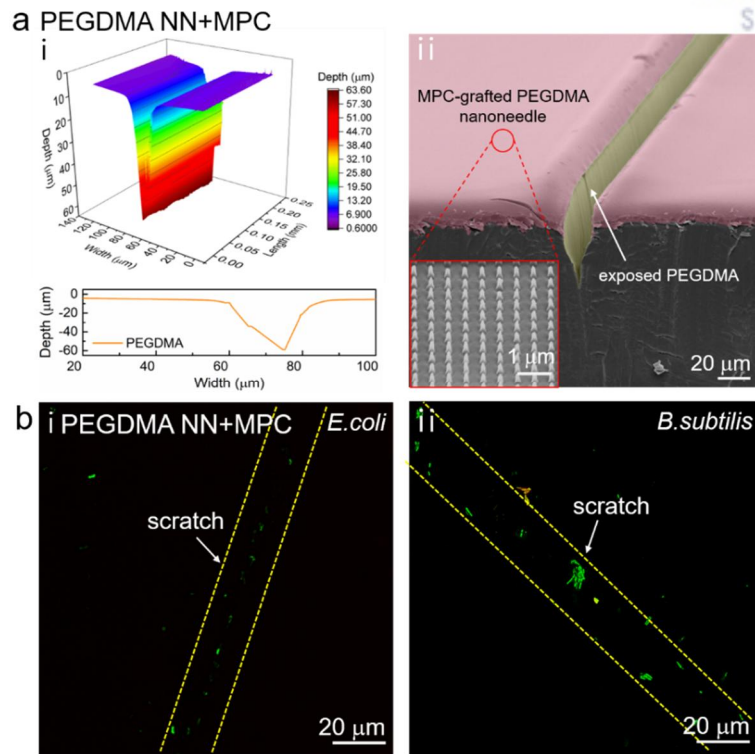


Figure 38. (a) (i) (top) 3D micrograph and (bottom) cross-section, and (ii) SEM images showing the damaged MPC-PEGDMA-NN. False colors were used to emphasize the damaged sites. (b) Confocal fluorescence microscopy images of the (i) *E. coli* and (ii) *B. subtilis* grown on the damaged MPC-PEGDMA-NN (culture hour: 18 h).



To compare the durable and robust anti-biofilm activity of the MPC-tethered PEGDMA with previously reported antifouling surfaces using PEG and MPC, we prepared PEG-grafted Si [43], MPC-grafted Si [29], and MPC-grafted PEGDMA on Si substrates (see Figure 39 for surface chemistry analysis of the samples).

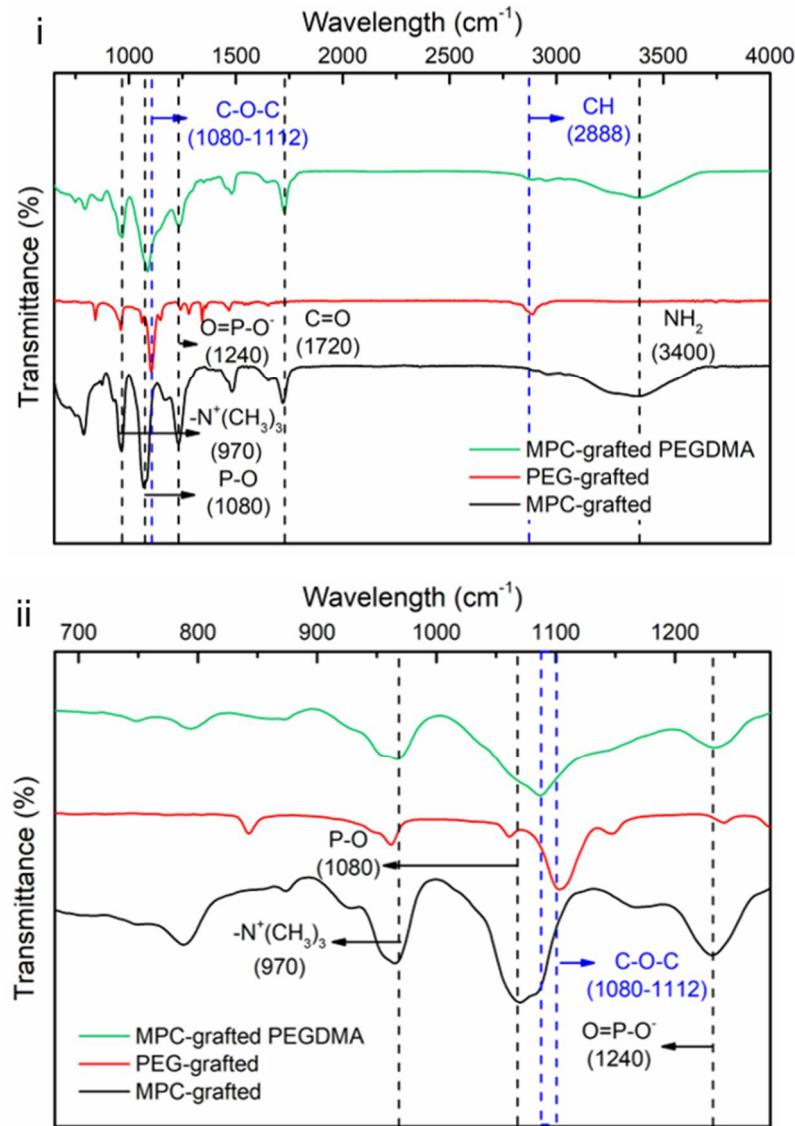


Figure 39. ATR-FTIR spectra of the PEG-grafted Si, MPC-grafted Si, and MPC-grafted PEGDMA on Si samples in the wavenumber ranges of (i) 650-4000  $\text{cm}^{-1}$  and (ii) 675-1275  $\text{cm}^{-1}$ . The PEG-grafted Si was prepared using PEG-aldehyde on a 3-aminopropyltriethoxysilane (APTES)-treated Si surface, which has been used in prior studies. The MPC-grafted Si was prepared based on the UV-induced free radical grafting method widely adopted in several prior studies. The MPC-grafted PEGDMA was prepared by covalently tethering MPC over 80% PEGDMA.



The prepared samples were mechanically scribed to generate defects on the surfaces, followed by culture of *E. coli* on the samples (Figure 40). On the PEG-grafted or MPC-grafted substrates, many a *E. coli* adhered and proliferated along the damaged site (Figure 41). This confirmed that the grafted PEG or MPC alone was prone to damage by external stimuli due to their low mechanical strength [29, 44]. As compared to the PEG or MPC grafting layers, the UV-crosslinked PEGDMA has a high elastic modulus. Accordingly, in contrast to the PEG-grafted or MPC-grafted substrates, the MPC-PEGDMA hybrid maintained effective biofilm resistance even when damaged (Figure 41, see Figure 42 for results against *B. subtilis*). Our MPC-grafted PEGDMA surface also displayed higher biofilm resistance than the MPC-PEGDMA mixture composite suggested in previous reports (Figure 43, 44, 45) [45]. This is because the MPC-grafted PEGDMA has higher MPC density at its surface than that of the MPC-PEGDMA mixture composite, as evidenced by the higher P and N ratio in the MPC-grafted PEGDMA (Table 3). The MPC-PEGDMA mixture composite also displayed a lower elastic modulus (0.0009–5 MPa) than that of the PEGDMA which lessened its mechanical durability [39].

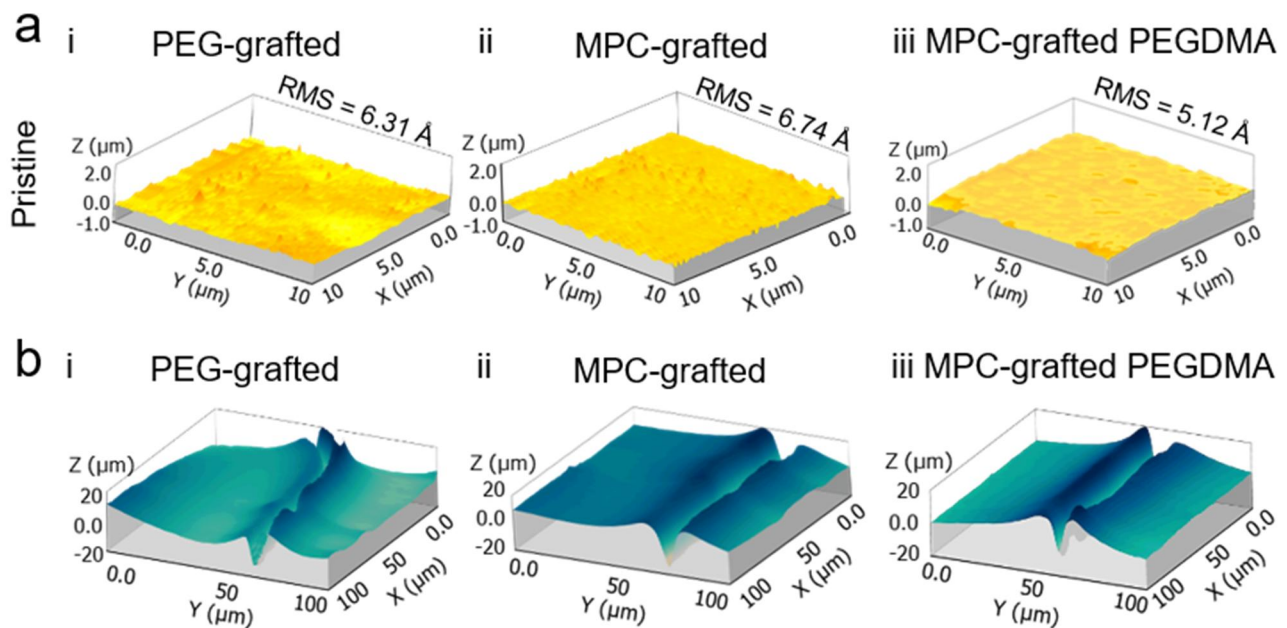


Figure 40. Three-dimensional micrographs showing the surfaces of the (i) PEG-grafted Si, (ii) MPC-grafted Si, and (iii) MPC-grafted PEGDMA (80 wt%) on Si substrates (a) before and (b) after applying mechanical stimuli.

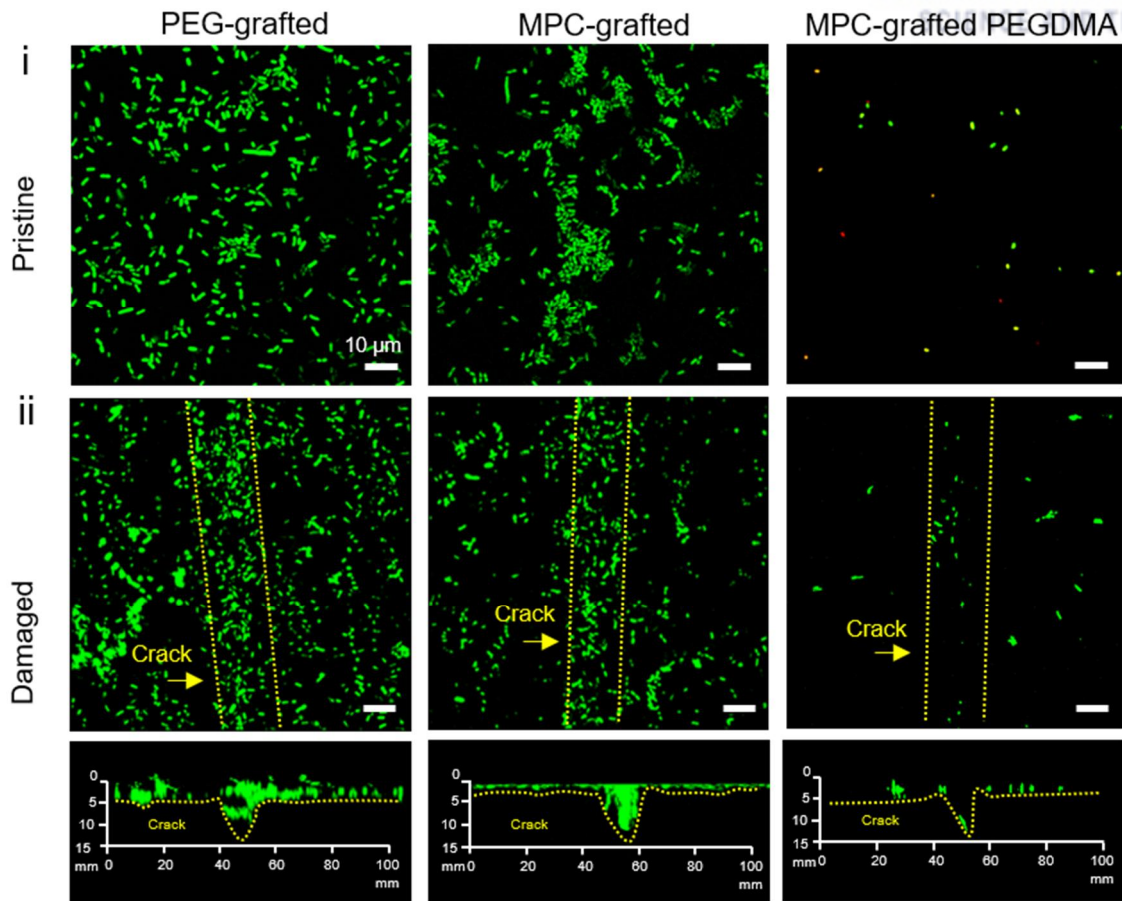


Figure 41. Confocal fluorescence microscopy images of *E. coli* on the PEG-grafted, MPC-grafted, and MPC-grafted PEGDMA samples (i) without- and (ii) with mechanical damages after 18 h of culture.

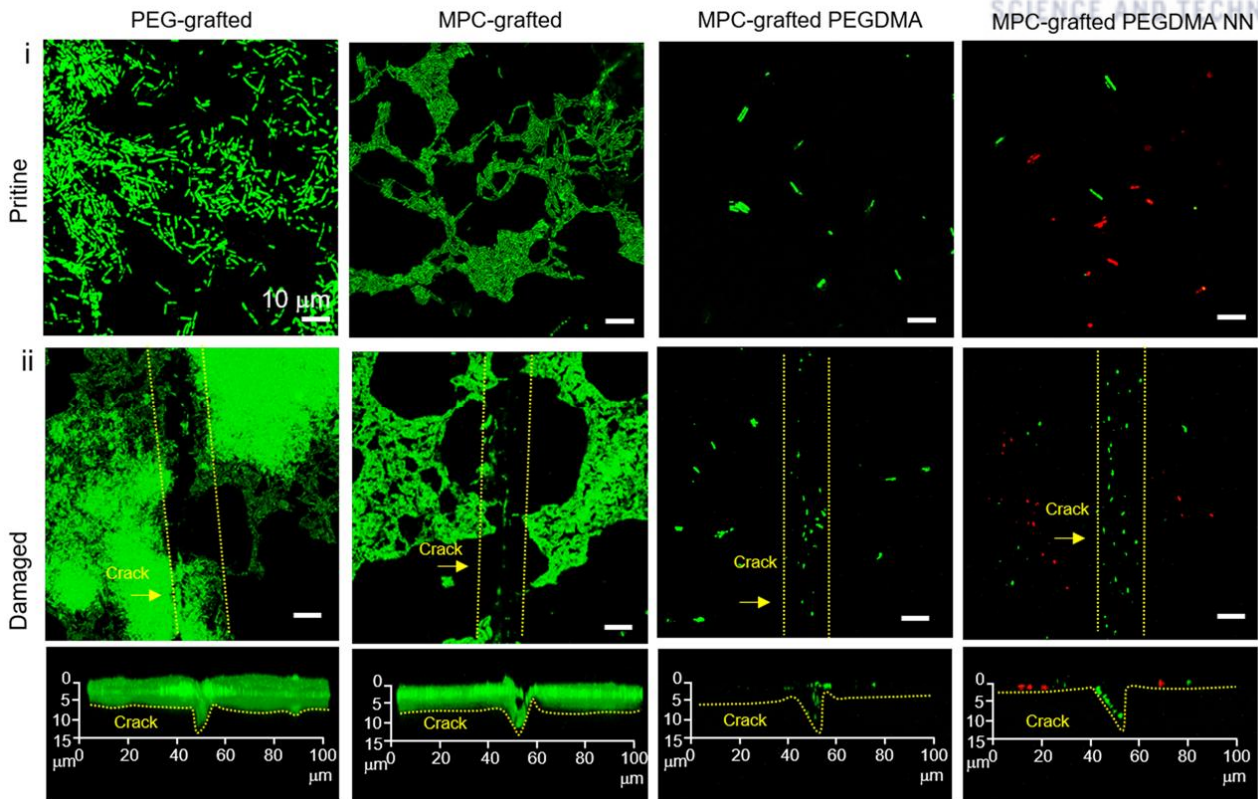


Figure 42. Confocal fluorescence microscopy images of *B. subtilis* on the PEG-grafted Si, MPC-grafted Si, MPC-grafted PEGDMA (80 wt%) on Si, and MPC-grafted PEGDMA (80 wt%) nanoneedles on Si substrates (i) without- and (ii) with mechanical damages after 18 h of culture.

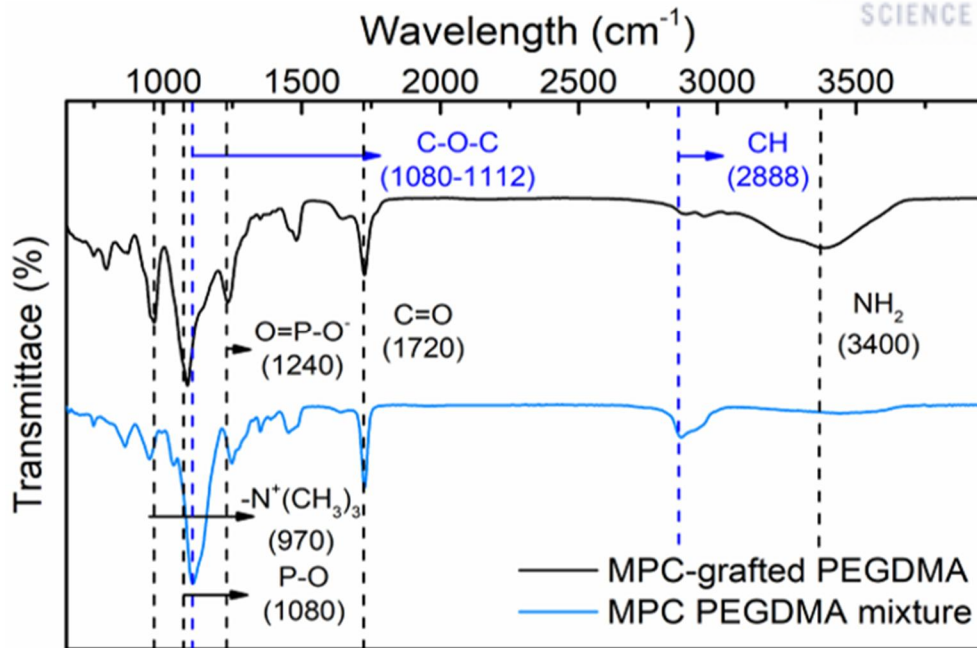


Figure 43. ATR-FTIR spectra of the PEGDMA-MPC mixture and MPC-grafted PEGDMA samples in the wavenumber ranges of (i) 650-4000 cm<sup>-1</sup>.

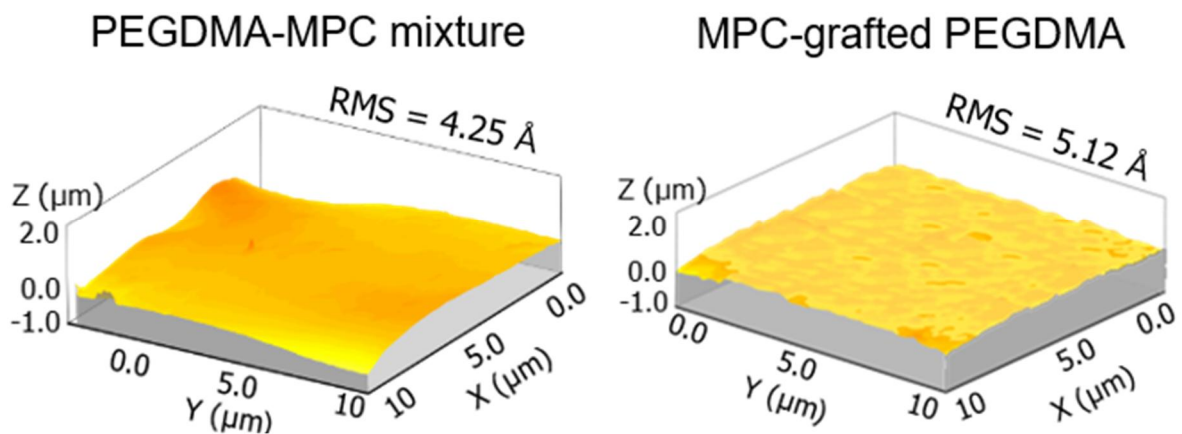


Figure 44. Three-dimensional micrographs showing the surfaces of the PEGDMA-MPC mixture (left) and MPC-grafted PEGDMA samples (right).

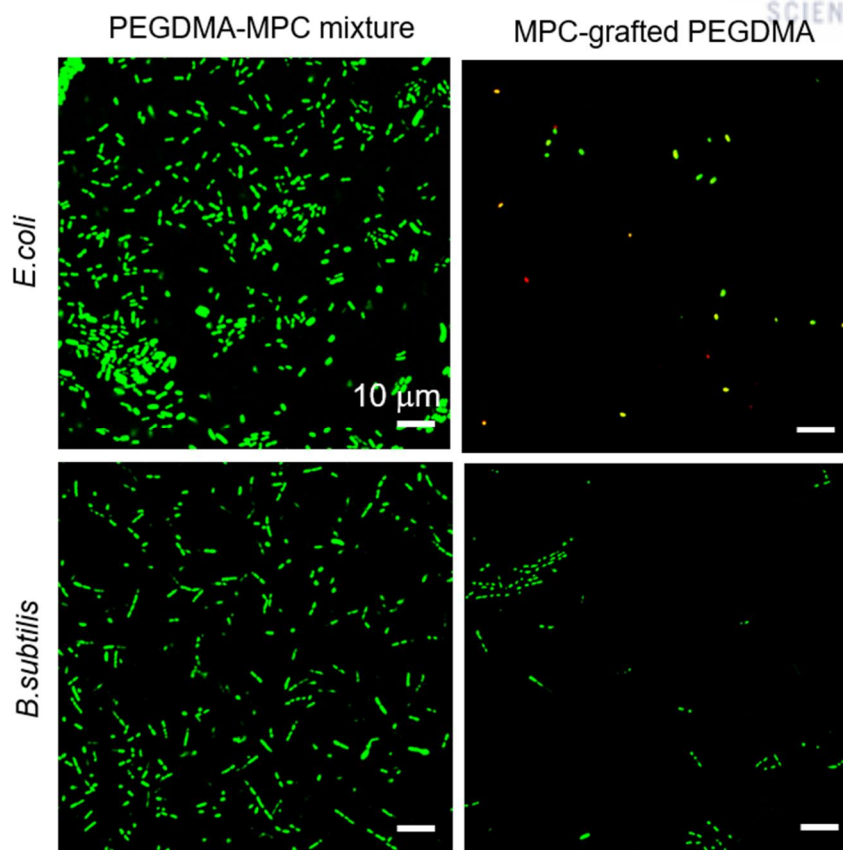


Figure 45. Confocal fluorescence microscopy images of *E. coli* and *B. subtilis* cultured on the PEG-MPC mixture and MPC-grafted PEGDMA samples for 18 h.

Table 3. Relative ratios of C, O, N, and P with respect to Si for the PEGDMA-MPC mixture and MPC-grafted PEGDMA samples measured by XPS.

Atomic ratio	Sample	
	PEGDMA-MPC mixture	MPC-grafted PEGDMA
C/Si	13.37	16.39
O/Si	6.090	7.750
N/Si	0.556	1.480
P/Si	0.823	1.527



### 2.3.6. Anti-biofouling performance against marine microorganism

The attachment of the most problematic algae in the marine industry is a serious problem. And antifouling is difficult due to attachment through spore. Figure 46 is the form of spore development in *Pyropia nezoensis*. The spore of *Pyropia nezoensis* was attached to the PEGDMA NN surface for 14 days. As shown in Figure 47 and 48-i, the attachment of the spore was very small on the PEGDMA surface. In particular, non-specific spores were only shown on the surface PEGDMA nanostructure. Additionally, the development of spore on nanostructure surface has significantly dropped (Figure 48-ii). This PEGDMA NN affects the attachment and the development of spore. If we apply the hybrid anti-biofouling surface to the marine industry, we will be able to solve the existing problems.

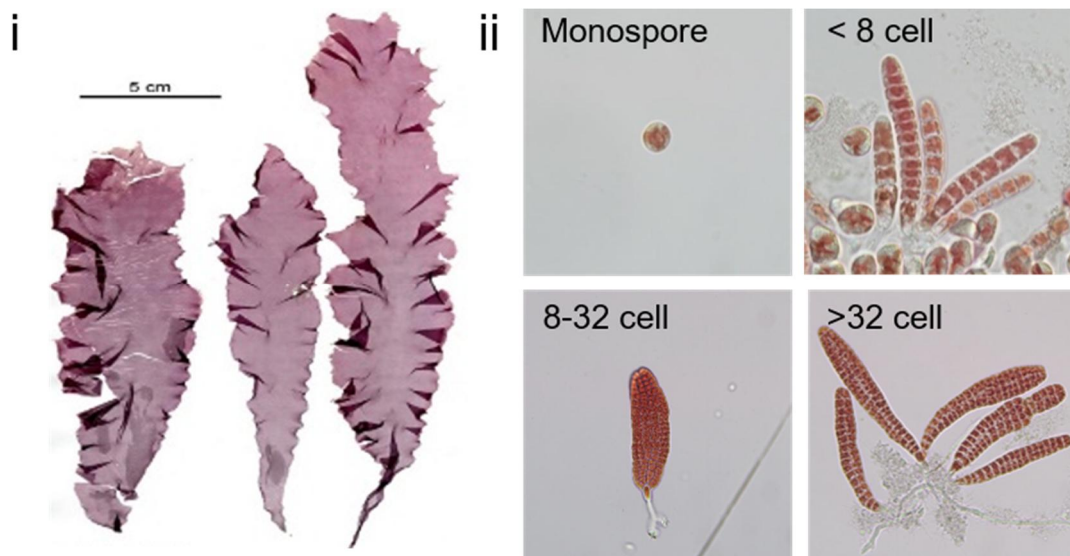


Figure 46. (i) Photograph of *Pyropia yezoensis* (ii) Development shape of *Pyropia yezoensis*.



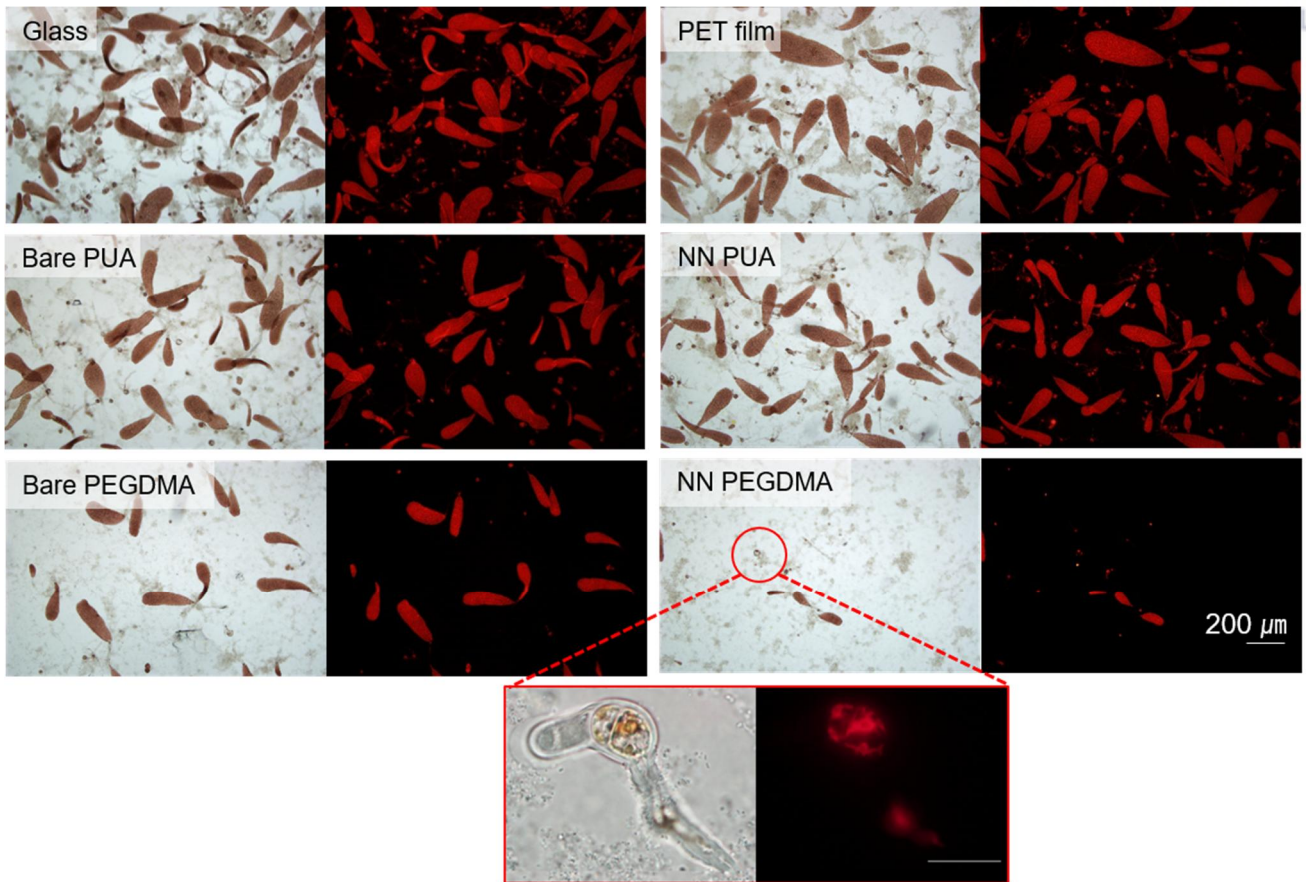


Figure 47. Attachment test of *Pyropia yezoensis* on various PUA and PEGDMA samples for 14 days.

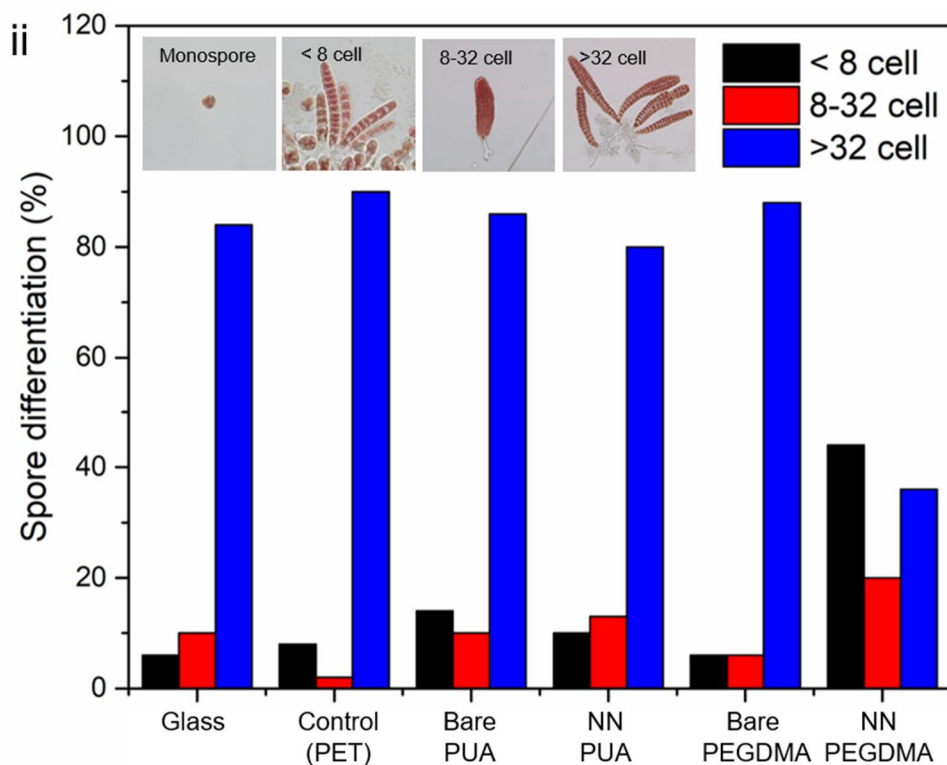
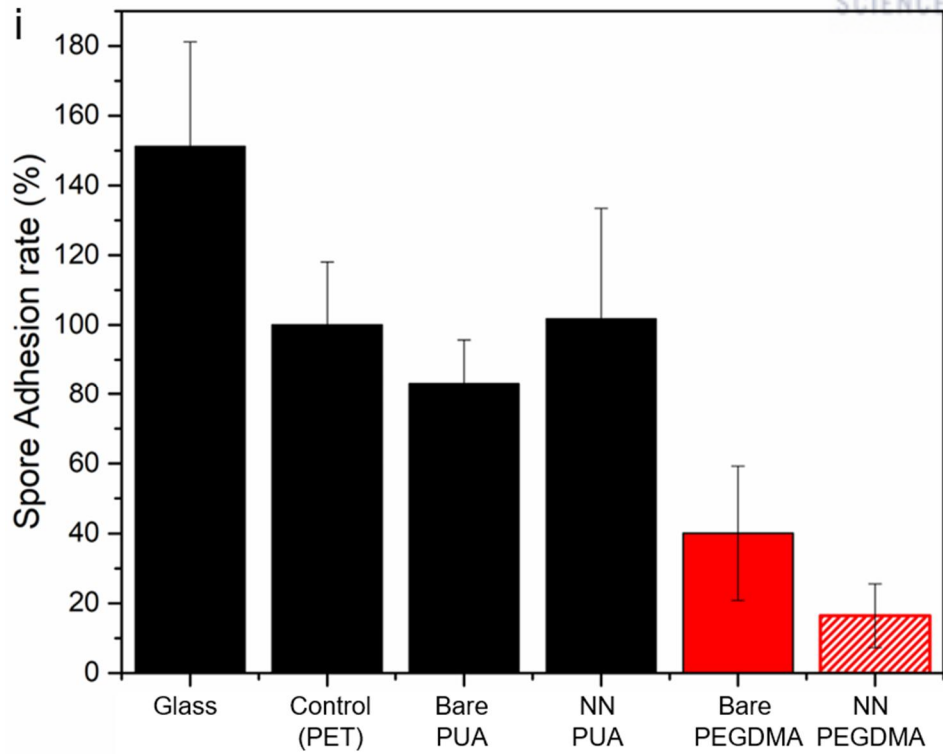


Figure 48. (i) Spore adhesion rate of *Pyropia yezoensis* spore, (ii) Development of *Pyropia yezoensis* spore on various PUA and PEGDMA samples for 14 days.

## 2.4. Summary

In summary, we developed a biocompatible, flexible, and robust anti-biofouling materials based on the MPC-PEGDMA-NN hybrids only with highly biocompatible polymers. By integrating the heterogeneous biocompatible polymers of PEGDMA and MPC with intrinsic antifouling nature into the nanoscale topological configuration, their hybrid not only exhibited maximized dual functions of antifouling and bactericidal activities against *E. coli* and *B. subtilis*, but also preserved the robust and superior anti-biofilm capability even when the hybrid was mechanically damaged. We believe that this lipid-hydrogel-nanostructure hybrid material could serve as a versatile material with superior antifouling activities for various daily, medical, and industrial applications.

### 3. Functionalized Cellulose acetate nanoneedle array

#### 3.1. Introduction

Exuberant growth of bacterial films on diverse surfaces has been a global problem in public health as well as in industry. Extensive endeavors have been devoted to developing biofilm-resistant materials that can effectively limit bacterial attachment and subsequent biofilm formation. Among the many different approaches, surface grafting or coating with biocidal materials such as antibiotics, silver, copper, nitric oxide, and carbon nanomaterials have demonstrated their effective resistance to biofilm formation [46-51]. However, these materials not only induce drug-resistance in bacteria but also display limited long-term activity [22]. More importantly, many of them are toxic, non-biocompatible, and environmentally harmful, which significantly hinders their uses in daily, biomedical, marine, and industrial applications [52, 53]. Biocompatible and biodegradable antifouling materials show unique advantages for a broad range of applications. For example, biodegradable marine-antifouling materials can reduce the disturbance of marine-ecosystem caused by non-biodegradable synthetic antifouling materials that accumulate in the aquatic environment [54, 55]. By considering recent interest towards safe and biocompatible antibacterial materials as well as biodegradable and eco-friendly materials, the development of highly biocompatible, and environmentally friendly materials with superior biofilm resistance is of great importance.

To this end, diverse polymeric materials have been suggested as efficient biocompatible antifouling materials. Among many different antifouling polymers, polyethylene glycol (PEG) represents one of the most widely used, well-known antifouling materials [12, 56-59]. The antifouling nature of the PEG polymer is attributed to the hydration layer formed on the surface and steric repulsion effect [60]. However, the antifouling performance of PEG can deteriorate in the presence of oxygen and transition metal ions as PEG is prone to oxidative damage [9]. MPC is also a well-known antifouling material, which mimics the phosphatidylcholine head group in the phospholipid bilayer of cell membranes. MPC can form a dense hydration layer through electrostatic interactions, which enables noticeable fouling-resistance to external contaminants [61]. However, MPC is mechanically less stable due to its poor mechanical strength [12].

Another type of biofilm-resistant materials —nanostructures with sharp tips (e.g., nanoneedles)— have been suggested as active bactericidal materials. Unlike antifouling materials that prevent attachment of bacterial cells, the sharp tipped nanostructured surfaces can kill bacteria by physically destroying the cell membranes [19, 62]. Prior studies documented that biofilm-resistant materials can be generated even using materials with limited antifouling properties. However, most of the previously described nanostructured surfaces were made of rigid and expensive materials, such as silicon, or non-degradable synthetic polymers, such as polydimethylsiloxane (PDMS) [63, 64]. Thus, they are susceptible to damage by external stimuli and difficult to apply onto curved or non-planar surfaces. They also have limited biodegradability (e.g., PDMS).

CA, one of the cellulose derivatives, has great potential as a biocompatible, environmentally friendly, and low-cost antifouling material as it is highly biocompatible, and biodegradable based on its inherent nature of

being produced from living organisms [65-67]. Hydrolysis by several enzymes is the principal mechanism of the biodegradation of CA (see Figure 49 for details). The abundant hydroxyl groups in CA impart a hydrophilic character [65, 68-71]. Moreover, CA is mechanically stable and flexible [65, 68, 71, 72]. However, CA does not have an inherent antifouling nature, and exhibit inferior resistance to biofilm formation [72, 73]. Consequently, several antifouling materials, including silver nanoparticles, copper nanoparticles, and polydopamine, have been incorporated into CA to generate CA-based antifouling materials [74-76]. However, most prior studies utilized planar, electrospun CA nanofiber mats, which do not have precisely defined surface nanostructures [75, 77, 78]. Despite several remarkable advantages of CA, few studies have addressed the development of biofilm-resistant materials based on the integration of biocompatible and eco-friendly CA and nanoscale architectures.

Herein, we present a highly effective and sustainable biofilm-resistant material that can suppress bacterial adhesion and biofilm formation based on a flexible nanostructured CA film. The nanostructured CA film is formed by shaping CA into a nanoscale needle array based on a simple nanomolding process. The CA nanoneedle array exhibits remarkable bactericidal performance for both gram-positive and gram-negative microbes by inducing physical lysis in the cell membranes despite limited antifouling nature of CA. To enhance the biofilm resistance of the CA nanostructures, MPC, a cell-membrane mimicking biocompatible monomer, is further coated over the CA array [79-82]. Based on the unique integration of the biocompatible and renewable CA, nanoneedle topography, and biocompatible antifouling MPC, the MPC-coated CA nanoneedle material shows remarkable antifouling and bactericidal behaviors simultaneously, and therefore enables the efficient and robust prevention of biofilm formation.

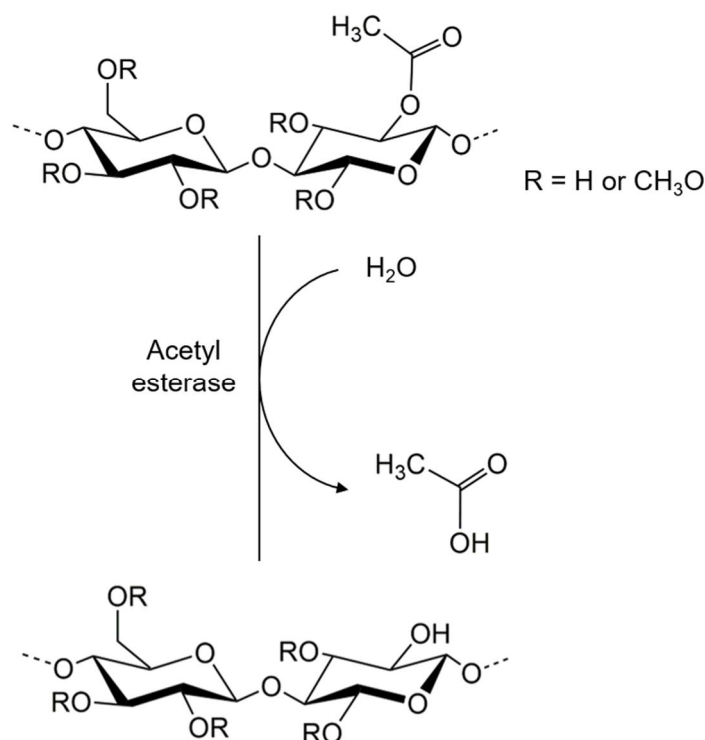


Figure 49. Biodegradation mechanism of CA.

## 3.2. Experimental

### 3.2.1. Fabrication of the MPC-coated cellulose acetate nanoneedle array

A silicon wafer (Si master mold) with nanohole array patterns was prepared by a conventional photolithographic process using a stepper (PAS 500/700D; ASML, the Netherlands). The nanoholes were 200 nm in diameter at the top (from the surface), 50 nm in diameter at the bottom, 300 nm in depth, and 500 nm in center-to-center pitch. Drops of polyurethane acrylate (PUA) prepolymer (311RM; Minuta Tech, Korea) were dispensed onto the Si master and a polyethylene terephthalate (PET) film (200  $\mu\text{m}$  thick; Chagnsung sheet, Korea) was placed over the drops. Subsequent exposure of the PET film-covered PUA drops to ultraviolet light ( $\lambda = 365 \text{ nm}$ , dose =  $200 \text{ mJ cm}^{-2}$ ) resulted in a PUA replica with nanoneedle patterns. The generated PUA replica was treated with oxygen plasma for 1 min ( $\text{O}_2$  flow rate: 100 sccm, power: 100 W) using a plasma generator (Cute; Femtosience, Korea) and subsequently functionalized with a trichloro(1H,1H,2H,2H-perfluorooctyl)silane (Cat No. 448931, Lot No. MKCF9461; Sigma Aldrich, USA) for surface hydrophobization. Subsequently, the fluorinated PUA replica was re-replicated with a hard polydimethylsiloxane (h-PDMS), which resulted in a h-PDMS master mold with nanohole arrays. In detail, a h-PDMS prepolymer was prepared by mixing 3.4 g of vinylmethylsiloxane-dimethylsiloxane (Cat No. VDT-731; Gelest, USA), 18  $\mu\text{L}$  of 2,4,6,8-tetramethyl-2,4,6,8-tetravinylcyclotetrasiloxane (Cat No. 396281, Lot No. MKBZ9752V; Sigma Aldrich, USA), and 18  $\mu\text{L}$  of platinum-divinyltetramethyldisiloxane (Cat No. SIP6831.1; Gelest, USA) in a glass vial at 500 rpm for 5 min using a magnetic stirrer (PC-410D; Corning, USA). One gram of trimethylsiloxy-terminated methylhydrosiloxane–dimethylsiloxane copolymer (Cat No. HMS-301; Gelest, USA) and 2 mL of toluene (Cat No. 244511, Lot No. STBG1996 V; Sigma Aldrich, USA) were added to the mixture and stirred at 500 rpm for 10 min. The prepared h-PDMS prepolymer was spin-coated over the fluorinated PUA replica at 1500 rpm for 30 s using a spin-coater (ACE-200; iNexus, Korea). Subsequent two-step curing at 25  $^{\circ}\text{C}$  for 1 h and 70  $^{\circ}\text{C}$  for 30 min resulted in the h-PDMS master mold with nanohole arrays. The arrays had almost identical geometries with that of the Si mater. A CA solution (20% w/v in acetone) was then drop-casted on the h-PDMS master mold. CA with a number average molecular weight of 30,000 and degree of substitution (DS) of 2.45 was used in this study (Cat No. 180955, Lot No. MKCB2731 V; Sigma Aldrich, USA). A PET film was placed on the CA drop. After drying the solvent at 25  $^{\circ}\text{C}$  (relative humidity: 35%) for 5 min, the solidified CA was removed from the master, which resulted in a flexible CA nanoneedle array. For MPC grafting, the CA nanoneedle array was treated with oxygen plasma to generate additional hydroxyl groups and carboxyl moieties on its surface ( $\text{O}_2$  flow rate: 100 sccm, power: 100 W, time: 60 s). Then, MPC (Cat No. 730114, Lot No. MKCF0806; Sigma Aldrich, USA) dissolved in deionized water (0.25 mol/L) was spin-coated on the array at 3000 rpm for 30 s, followed by drying in a convection oven (ON-11E; Jeiotech, Korea) at 70  $^{\circ}\text{C}$  for 1 h.

### 3.2.2. SEM, AFM, and TEM imaging

To obtain scanning electron microscopy (SEM) images of the samples, the samples were coated with Pt



(thickness: 5 nm) using a metal sputter (K575X, Quorum Emitech, UK). The Pt coated samples were then examined with a S-4800 SEM (Hitachi, Japan). Atomic force microscopy (AFM) images of the samples were obtained with a Multimode V AFM (Veeco, USA). To obtain transmission electron microscopy (TEM) images of the MPC-coated CA nanoneedle samples, the samples were first milled with a focused ion beam (FIB) (Helios 450 HP, FEI, USA) using gallium (Ga) ion. Before the FIB milling, an amorphous carbon layer was coated on the samples to protect them from ion beam damages. During the FIB milling, the accelerating voltage of Ga ion was 5 kV and the ion beam current was adjusted between 68 pA and 0.79 nA. The final milling was performed with Ga beam current from 80 pA to 0.23 nA at 3 kV of accelerating voltage. The samples were milled from both sides until the sample thickness was reduced to 90 nm. Then, the prepared samples were examined with a TEM (JEM-2100, JEOL, Japan) at 200 kV of accelerating voltage.

### **3.2.3. Attenuated total reflectance-Fourier transform infrared (ATR-FTIR) spectroscopy and X-ray photoelectron spectroscopy (XPS)**

Fourier transform infrared spectroscopy analysis was carried out on a Cary 670 instrument (Agilent, USA) using a Ge 45° crystal (PIKE MIRacle, Germany). The spectra were recorded in a wavenumber range of 650–4000  $\text{cm}^{-1}$  at a resolution of 4  $\text{cm}^{-1}$ . Surface element analysis was performed with an X-ray photoelectron spectroscope (ESCALAB 250XI, Thermo Fisher Scientific, USA) using an Al  $K\alpha$  source.

### **3.2.4. Contact angle measurements**

The surface wetting properties of the samples were investigated by measuring the contact angles of water droplets on each sample using a contact angle analyzer (SDLAB 200TEZD, FEMTOFAB, Korea) (temperature: 25 °C, relative humidity: 50%). The average contact angle values for each sample were obtained by repeating the contact angle measurement 5 times per sample.

### **3.2.5. Measurements of mechanical properties and optical transmittance**

The mechanical behavior of the pristine CA sample was analyzed with a universal testing machine (UTM, Instron 5982, Instron Corporation). Testing was performed based on the ASTM D638 mode using sample dimensions of 150 × 15 × 5 (length × width × thickness, mm). The measurements were repeated five times for each sample and the average value was used. Optical transmittance of the samples was measured in a wavelength range of 250–800 nm using a UV-Vis-NIR spectrophotometer (Cary 5000, Agilent, USA).

### **3.2.6. Anti-bacterial film assay**

Firstly, *Escherichia coli* (*E. coli*) and *Bacillus subtilis* (*B. subtilis*) were grown in Luria broth within a shaking incubator (temperature: 37 °C, rpm: 200) until optical density measurement at 600 nm (OD600) reached 0.1. Then, sterilized glass and CA samples were immersed in the precultured bacterial suspension and incubated at 37 °C for 3 – 30 h. Subsequently, the samples were stained with a live and dead bacterial viability kit (BacLight™, L7012, Molecular Probes, Invitrogen, NY, USA) according to the protocol suggested by the

manufacturer, followed by rinsing with phosphate-buffered saline (PBS). Fluorescence micrographs of the stained bacteria were obtained using a confocal laser scanning microscope (LSM 780, Carl Zeiss, Germany). The coverage area of the bacterial cells on each sample was evaluated with an image processing software (Image J, NIH, USA). For a colony forming unit (CFU) assay, samples were incubated with 2 mL of a bacterial suspension ( $OD_{600} = 0.1$ ) for 18 h at 37 °C, followed by rinsing with PBS. The washed samples were then moved to a conical tube with 1 mL PBS and vortexed for 5 min to remove all bacterial cells from the samples. After serial dilution, this bacterial mixture was added on LB agar plates. Finally, the agar plates were incubated for 18 h at 37 °C and bacterial colonies were counted.

### 3.3. Results and Discussion

#### 3.3.1. Preparation and structures of the cellulose acetate nanoneedle array

Figure 50 shows the fabrication procedure of the nanoneedle array using CA as a base material. Among the diverse cellulose derivatives, we employed CA as it is stable inside or in the presence of water, which is an important consideration for practical and robust antifouling applications. To generate the CA nanoneedle array, we adopted a series of sequential replica molding processes (Figure. 50). Briefly, a positive mold with nanoneedles was prepared from a silicon wafer with nanohole array pattern (Si master mold) using a PUA. PUA is a UV-curable material, which enables rapid and precise nanopatterning [83, 84]. Then, a negative mold with a nanohole array was prepared from the as-prepared positive PUA mold by utilizing a h-PDMS. Subsequently, a drop of CA solution was drop-dispensed on the h-PDMS nanohole pattern, followed by evaporation of the solvent. After complete solvent evaporation, the cured CA was removed from the h-PDMS mold, resulting in a CA nanoneedle array. Note that it was difficult to replicate CA nanoneedles directly from the Si master as the non-permeable nature of the Si substrate prevents solvent evaporation and therefore hinders CA solidification. Finally, the surface of the CA nanoneedle was coated with MPC via oxygen plasma treatment, which equips the CA array with an antifouling capability. Consequently, the resulting structure is fully made of biocompatible and eco-friendly materials of CA and MPC without using any toxic or environmentally harmful materials.

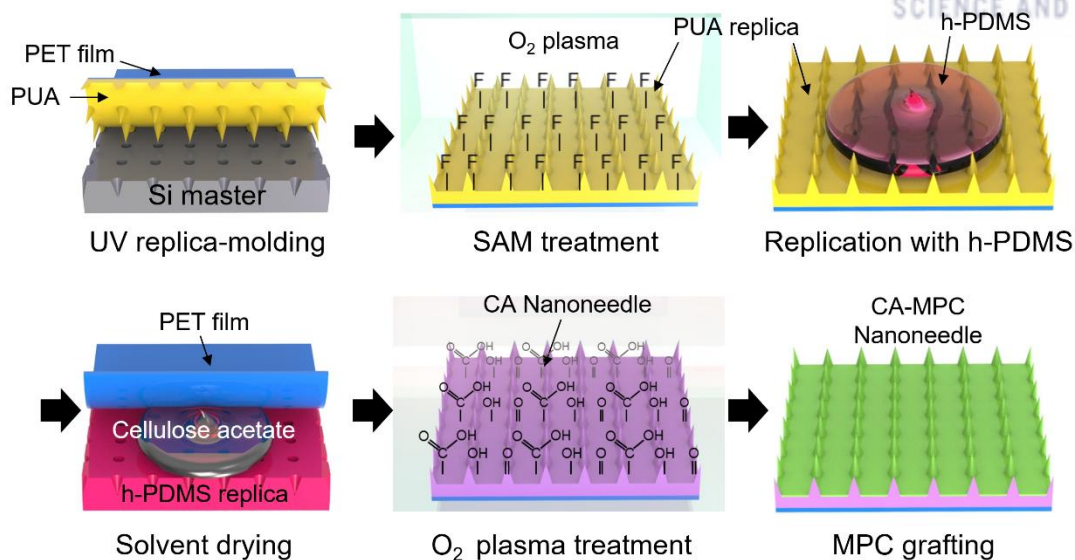


Figure 50. Schematic of the fabrication procedure for the cellulose acetate (CA) nanoneedle array grafted with 2-methacryloyloxyethyl phosphorylcholine (MPC).

In this hybrid material, the CA nanoneedle functions as a biocompatible, eco-friendly, and mechanically robust bactericidal material that can induce physical damage in the cell membrane. However, CA has limited fouling resistance to biofilm formation. In contrast, MPC has pronounced antifouling properties [85]. However, MPC typically shows poor mechanical strength and is difficult to use as a structural material for preparing nanostructures [12]. Thus, we expected that the co-utilization of CA nanoneedle and MPC could act synergistically to maximize biofilm resistance against diverse gram-negative and gram-positive bacteria, while preserving structural integrity.

Figure 51 shows the resulting CA nanoneedles arranged in a regular rectangular array. CA nanostructures with sharp tips were uniformly formed over a large area (Figure 51 and Figure 52-i, ii). The nanostructures were 50 nm in tip diameter, 200 nm in diameter at the base, 300 nm in height, and 500 nm in center-to-center pitch (Figure 52-ii, iii). The surface of individual nanoneedles was uniformly coated with the 5 nm thick MPC, as evident from TEM analysis (Figure 52-iii) [86, 87]. On a macroscopic scale, the resulting CA is in the form of a highly flexible film, which enables the versatile application of the nanostructured CA on diverse surfaces with varying surface curvatures and roughness (Figure 52-i). The rainbow-like colors of the nanostructured CA were caused by the structural color of the periodic nanopattern array that interferes with light [88].

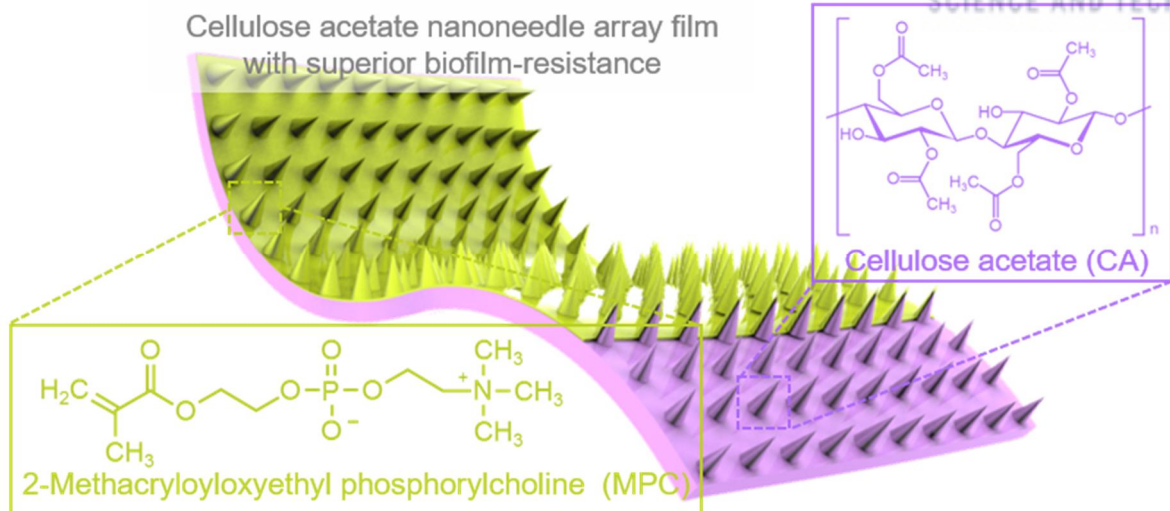


Figure 51. Conceptual illustration of the flexible CA nanoneedle array on which MPC is uniformly coated.

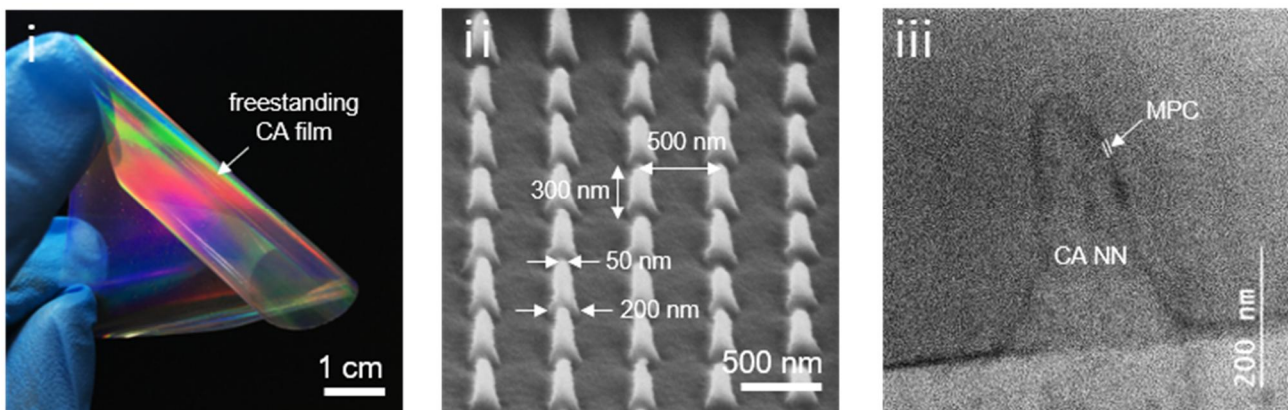


Figure 52. (i) Photograph of the fabricated MPC-coated CA nanoneedle film, (ii) an SEM image of the CA nanoneedle array, (iii) a TEM image of the single CA nanoneedle coated with MPC. The dark coating layer around the nanoneedle represents the MPC layer with a thickness of 5 nm.

### 3.3.2. Chemical mechanism of the MPC-grafted cellulose acetate nanoneedle array

Surface chemistry of the CA nanoneedle array coated with MPC was examined with ATR-FTIR spectroscopy and XPS. The IR spectra of the pristine, O<sub>2</sub> plasma-treated, and MPC-coated CA were shown in Figure 53. The pristine CA exhibited several characteristic peaks in the IR spectra. The peaks at 1050 cm<sup>-1</sup>, 1370 cm<sup>-1</sup>, and 1753 cm<sup>-1</sup> corresponded to C-O stretching, C-H bending vibration of CH<sub>3</sub>, and C=O stretching of the acetyl group, respectively (Figure 53a). The peak at 3465 cm<sup>-1</sup> was attributed to O-H stretching, which was much weaker than the same peak for pure cellulose due to acetylation [89, 90]. The peak related to C-O-C was at 1232 cm<sup>-1</sup>. After O<sub>2</sub> plasma treatment, these characteristic peaks were enhanced (Figure 53a). Pronounced changes were also observed in the XPS results for the O<sub>2</sub> plasma-treated CA (Figure 54a). The O=C-O peak (binding energy [BE] = 288.3-288.7 eV), C=O/O-C-O peak (BE = 287.2-288.0 eV) of C<sub>1s</sub> were enhanced while the C-H (or C-C) peak (BE = 284.2 eV) of C<sub>1s</sub> was reduced after the plasma treatment [91]. The enhanced peak of O=C-O indicates that carboxyl group was generated on the CA surface via plasma treatment (Table 4). Several previous studies have similarly reported the O<sub>2</sub> plasma-induced generation of carbonyl groups on cellulose mediated by free radical formation [92-95]. In detail, the O<sub>2</sub> plasma treatment can result in the chain cleavage and radical generation at various positions of CA. These radical intermediates further oxidize to become carboxylic acid and ketone for primary and secondary oxygenated groups, respectively (Figure 56). This generation of hydrophilic carbonyl groups significantly enhanced the surface energy of CA, as identified by reduced water contact angle (Figure 57). When O<sub>2</sub> plasma treated CA was treated with MPC, the radical intermediates generated on CA during O<sub>2</sub> plasma, prior to becoming more stable carbonyl groups, reacted with the methacrylic group on MPC either via addition or oligomerization, thereby covalently linking MPC onto CA surface (Figure 55c,d, 58). This explanation was supported by the significant reduction of O=C-O peak in XPS spectra for O<sub>2</sub> plasma treated CA after MPC treatment, compared to that of O<sub>2</sub> plasma treated CA without MPC treatment (Table 4, Figure 54a). The stable MPC linkage to CA was also confirmed with FT-IR and XPS spectra. When the O<sub>2</sub> plasma-treated CA sample was coated with MPC, five distinctive peaks were observed at 970 cm<sup>-1</sup>, 1080 cm<sup>-1</sup>, 1240 cm<sup>-1</sup>, 1620 cm<sup>-1</sup>, and 3400 cm<sup>-1</sup> in the FTIR spectra, which were attributed to N<sup>+</sup>-(CH<sub>3</sub>)<sub>3</sub>, P-O, O=P-O, N-H and NH<sub>2</sub>, respectively (Figure 53b) [12]. Also, the peaks of nitrogen (N<sub>1s</sub>) and phosphorous (P<sub>2p</sub>) in the XPS spectra notably increased for the MPC-coated CA samples compared with the CA samples without MPC treatment (Figure 54c, d and Table 5). These results confirm that the MPC moieties were uniformly coated over the CA surface via plasma polymerization.



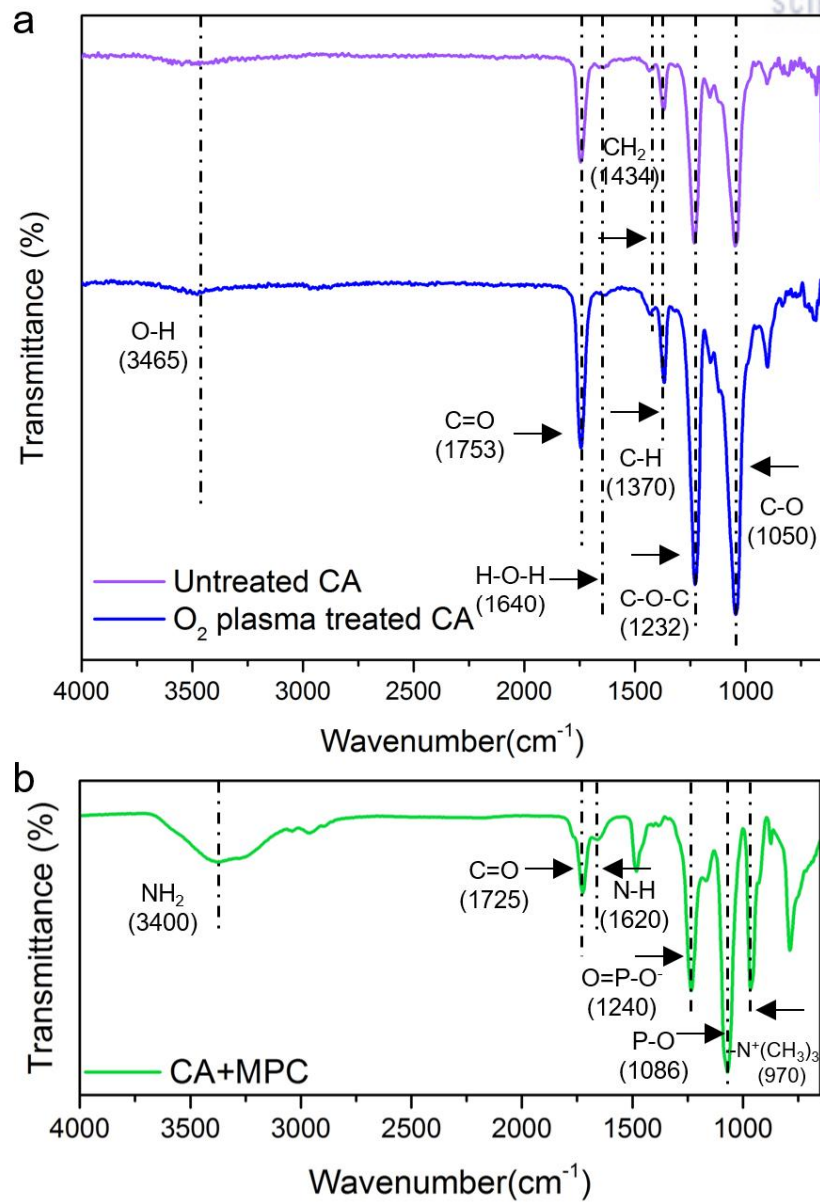


Figure 53. (a) ATR-FTIR spectra of the pristine and  $\text{O}_2$  plasma-treated CA in the wavenumber range of 650-4000  $\text{cm}^{-1}$ . (b) ATR-FTIR spectra of the MPC-coated CA in the wavenumber range of 650-4000  $\text{cm}^{-1}$ .



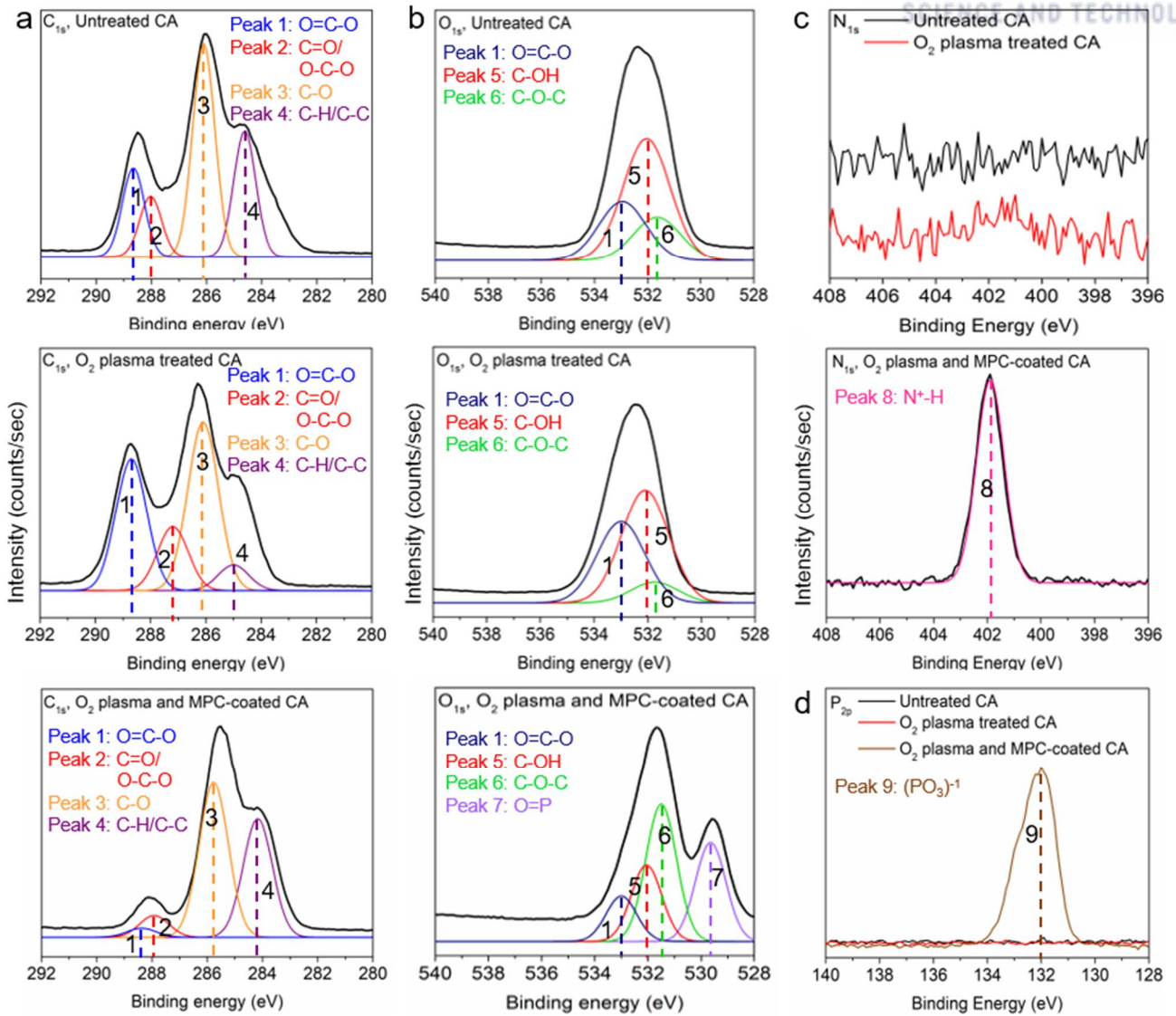


Figure 54. Deconvoluted peaks of (a) C<sub>1s</sub>, (b) O<sub>1s</sub>, (c) N<sub>1s</sub>, and (d) P<sub>2p</sub> of XPS spectra of the pristine, O<sub>2</sub> plasma-treated, and MPC-coated CA samples.

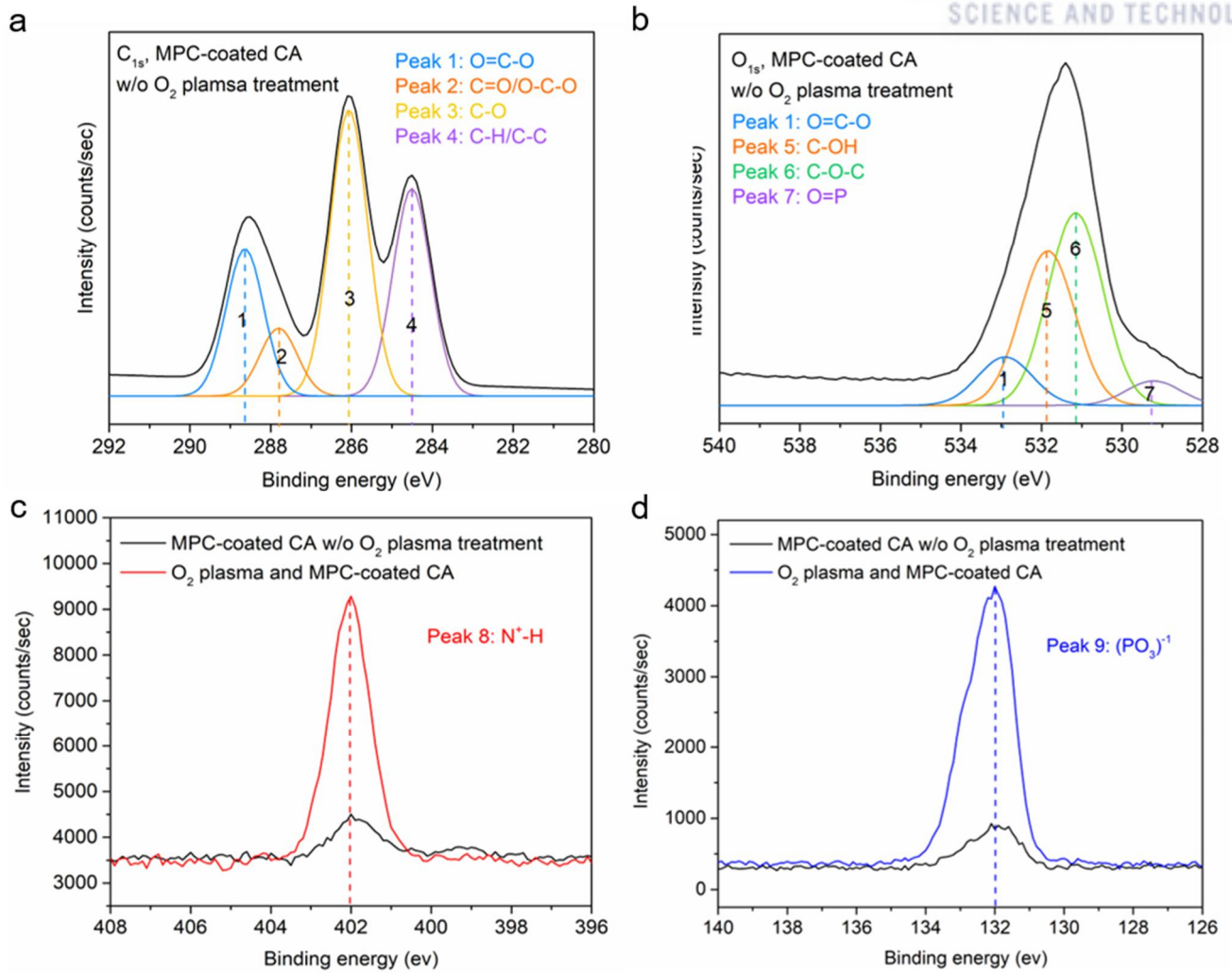


Figure 55. Deconvoluted peaks of (a)  $C_{1s}$ , (b)  $O_{1s}$ , (c)  $N_{1s}$ , and (d)  $P_{2p}$  of XPS spectra of the  $O_2$  plasma-treated and MPC-coated CA samples and MPC-coated CA samples without  $O_2$  plasma treatment.

Table 4. Relative concentrations of the functional groups from deconvoluted  $C_{1s}$ ,  $O_{1s}$ ,  $N_{1s}$ , and  $P_{2p}$  peaks of the XPS spectra of the untreated,  $O_2$  plasma-treated,  $O_2$  plasma-treated and MPC-coated, and MPC-coated without  $O_2$  plasma treatment samples.

Atomic Composition	$C_{1s}$ (%)				$O_{1s}$ (%)				$N_{1s}$ (%)	$P_{2p}$ (%)
	Peak 1 [O=C-O]	Peak 2 [C=O/ O-C-O]	Peak 3 [C-O]	Peak 4 [C-H/ C-C]	Peak 5 [C-OH]	Peak 1 [O=C-O]	Peak 6 [C-O-C]	Peak 7 [O=P]		
Binding energy (eV)	288.4	288.0	286.1	284.2	532.0	533.0	531.6	529.8	402	132
Untreated	18.8	11.8	43.9	25.5	69.5	17.8	12.7	-	-	-
$O_2$ plasma-treated	33.0	13.5	44.5	9.0	59.6	35.7	4.7	-	-	-
$O_2$ plasma-treated and MPC-coated	1.7	7.0	53.8	37.5	18.8	10.8	40.8	29.6	100	100
MPC-coated without $O_2$ treatment	20.7	9.6	42.4	27.3	36.7	11.5	45.9	5.8	100	100

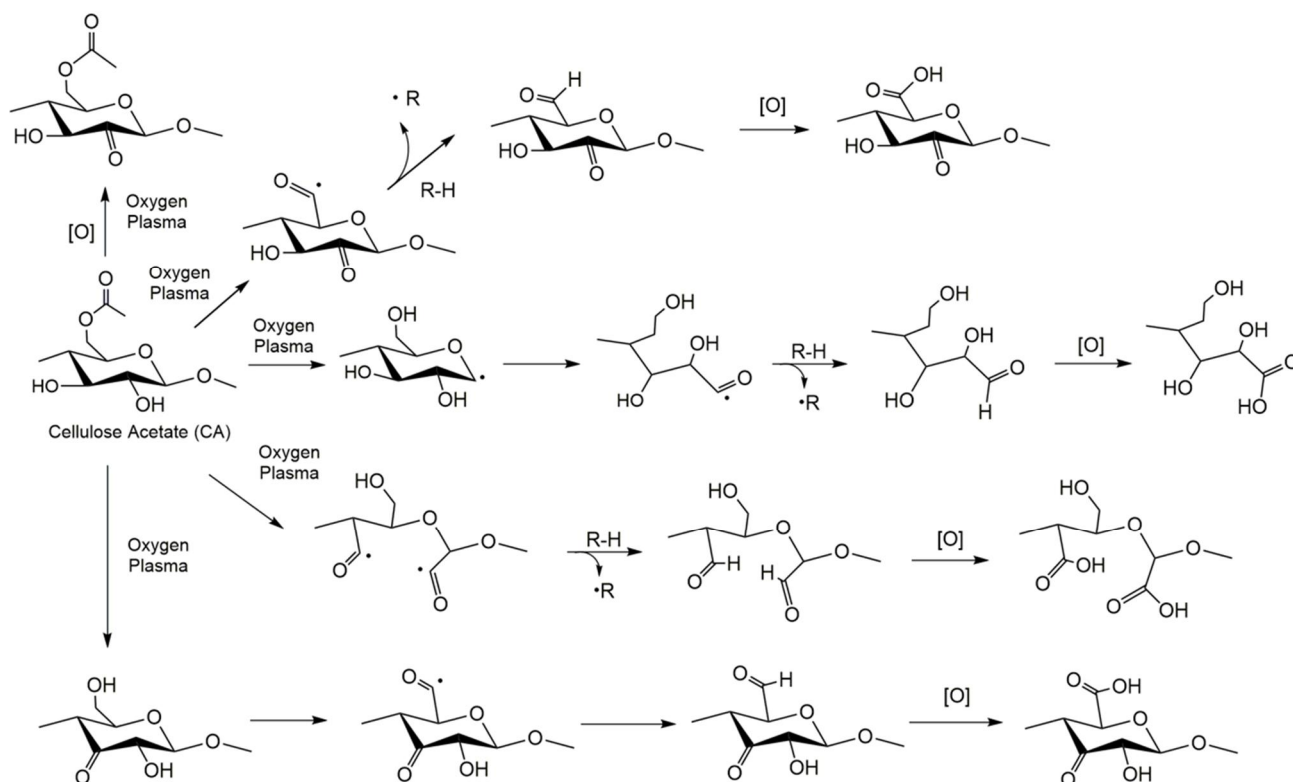


Figure 56. Carbonyl groups (carboxylic acid and ketone) were generated on various positions of CA unit.

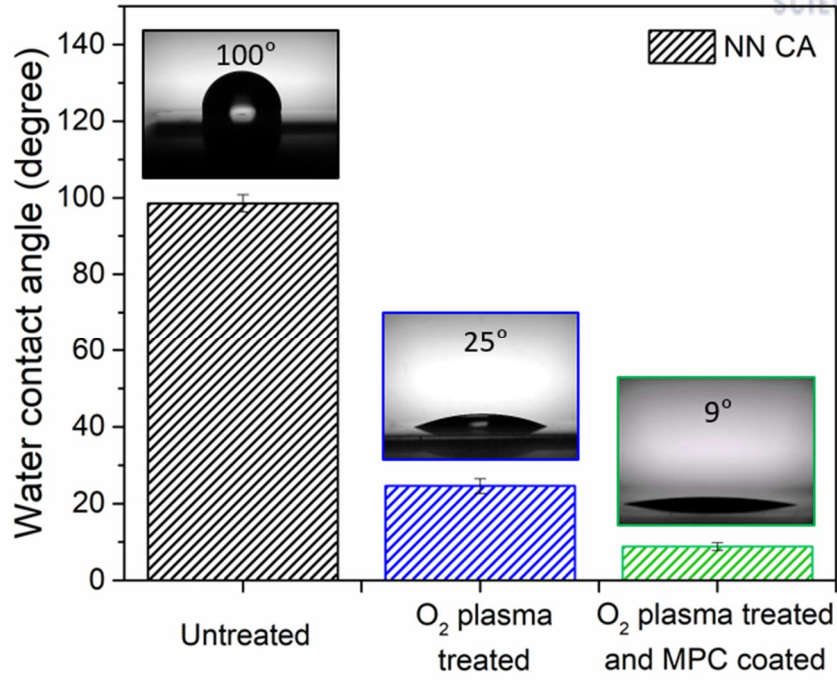


Figure 57. Contact angle of water droplet on untreated, O<sub>2</sub> plasma treated and O<sub>2</sub> plasma treated and MPC coated surfaces.

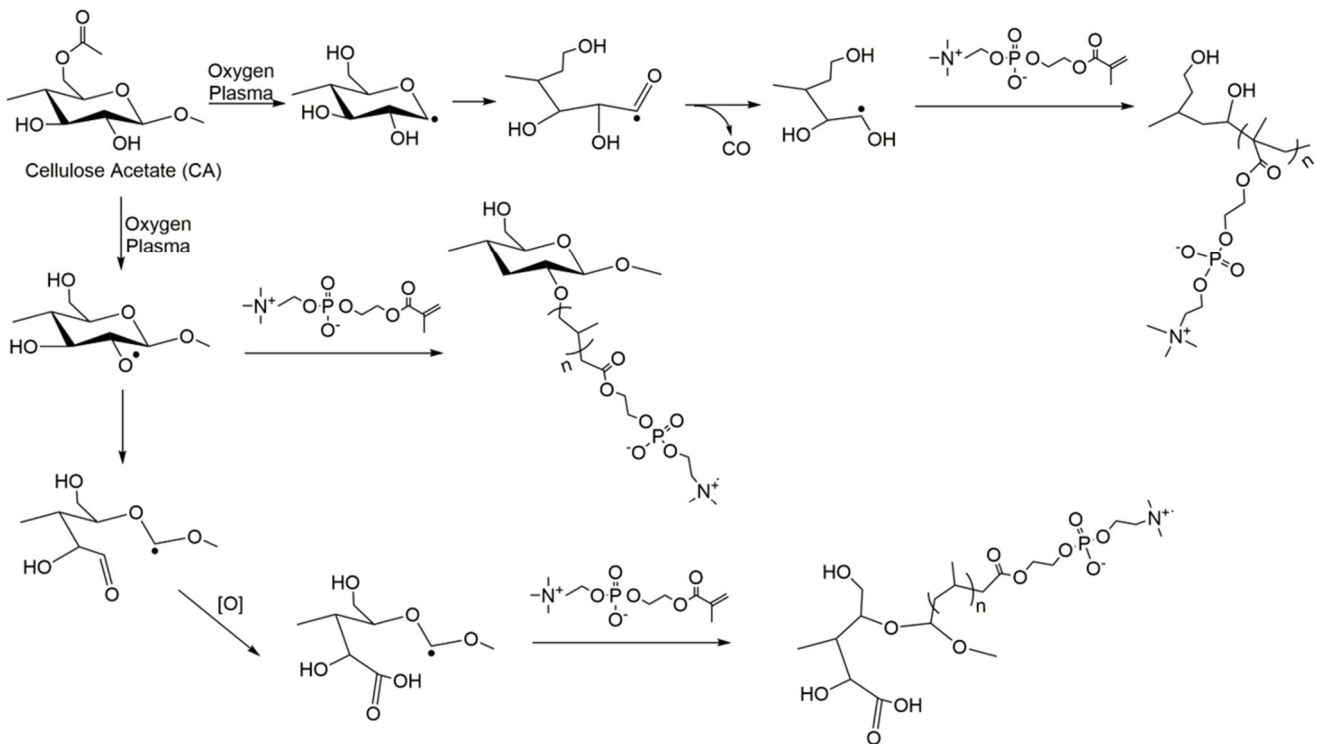


Figure 58. MPC reacted with radical intermediates of CA via addition or oligomerization.

Table 5. Surface elemental compositions of C<sub>1s</sub>, O<sub>1s</sub>, N<sub>1s</sub>, and P<sub>2p</sub>, and their relative ratios for the untreated, O<sub>2</sub> plasma-treated, O<sub>2</sub> plasma-treated and MPC-coated, and MPC-coated without O<sub>2</sub> plasma treatment samples measured by XPS.

Sample	Atomic Composition (%)				Atomic ratio		
	C <sub>1s</sub>	O <sub>1s</sub>	N <sub>1s</sub>	P <sub>2p</sub>	O/C	N/C	P/C
Untreated	62.4	37.6	0.00	0.00	0.603	0.000	0.000
O <sub>2</sub> plasma-treated	51.2	48.8	0.00	0.00	0.953	0.000	0.000
O <sub>2</sub> plasma-treated and MPC-coated	59.1	30.0	5.6	5.3	0.507	0.096	0.090
MPC-coated without O <sub>2</sub> treatment	60.8	35.5	1.9	1.7	0.584	0.0312	0.028

### 3.3.3. Surface, mechanical, and optical properties of the MPC-grafted cellulose acetate nanoneedle array

Figure 59 shows the contact angles of DI water on the planar CA, CA nanoneedles, and MPC-coated CA nanoneedle samples. The pristine, planar CA exhibited a hydrophilic nature with a water contact angle of 70°. Nanostructured CA showed an enhanced contact angle of 100° due to its surface roughness. However, when the CA nanoneedle was coated with MPC, the contact angle drastically decreased to 9°, which indicates that the CA nanostructure was stably functionalized with MPC via the simple oxygen plasma treatment. To further evaluate the stability of the MPC layer coated over the CA nanoneedle array, we submerged the MPC-coated CA nanoneedles in DI water for different periods of 0 – 28 d. Then, water contact angle and FTIR measurements were performed for the MPC-coated samples with different periods of water exposure. The water contact angle on the MPC-coated samples remains at 9 – 10° even after 28 d-submersion in water (Figure 60). FT-IR analysis results also showed consistent, characteristic MPC spectra regardless of the water-exposure time (Figure 61). These results confirm that the polymerized MPC layer is stable in water.

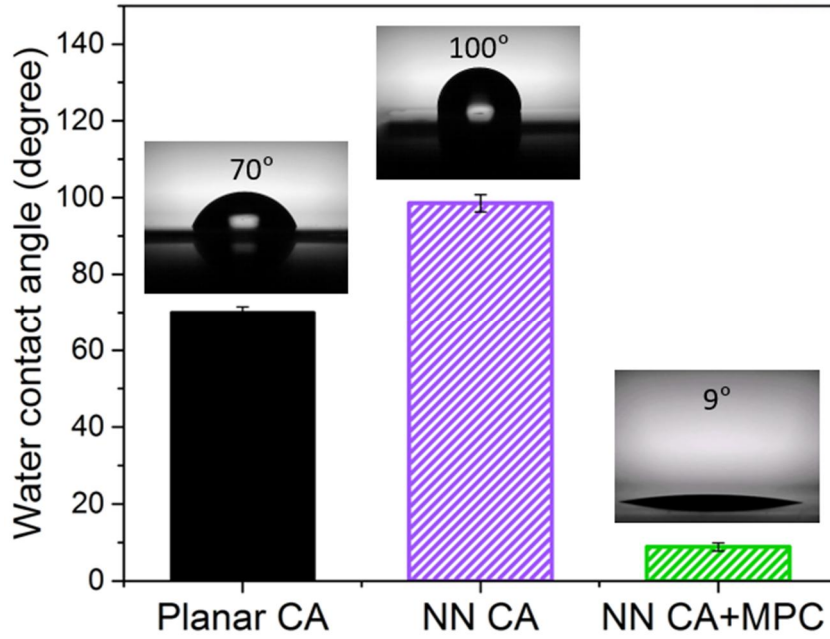


Figure 59. Contact angle of water droplet on the planar CA, CA nanoneedle, and MPC-coated nanoneedle surfaces.

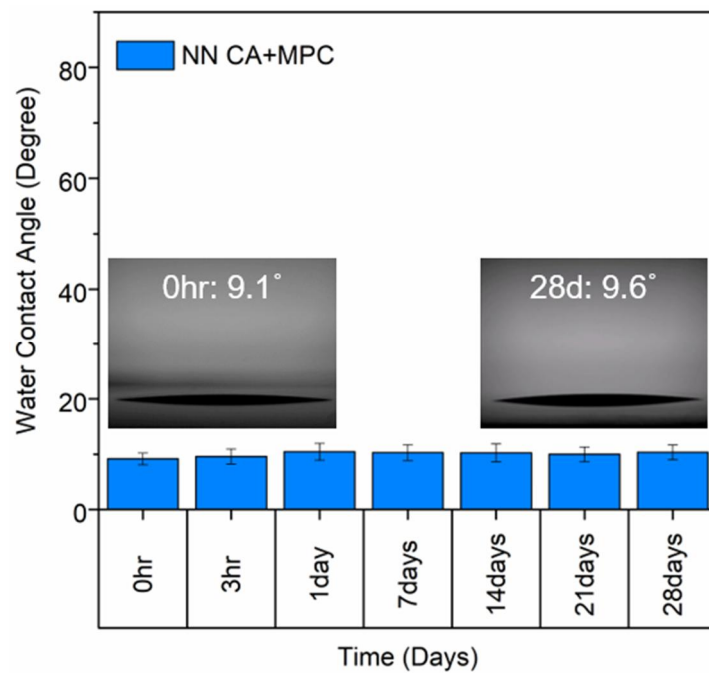


Figure 60. Contact angle measurements of the O<sub>2</sub> plasma-treated and MPC-coated nanoneedle samples, which were submerged in DI water for different periods of 0 – 28 d.



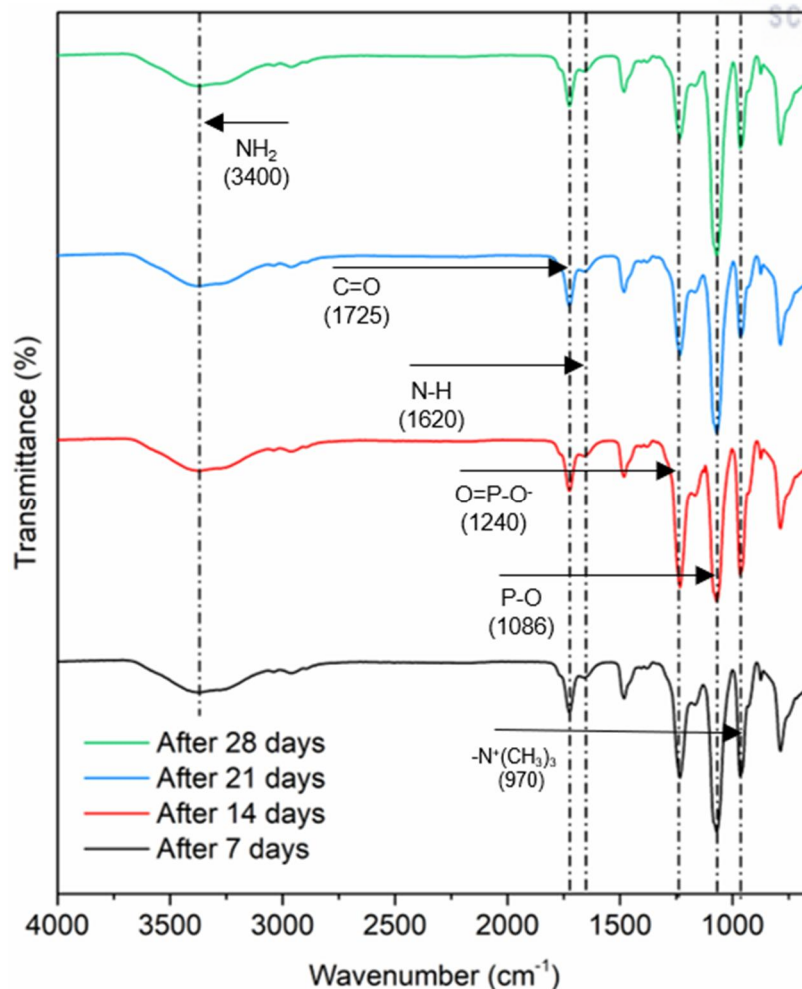


Figure 61. ATR-FTIR spectra of the O<sub>2</sub> plasma-treated and MPC-coated nanoneedle samples, which were submerged in DI water for different periods of 0 – 28 d.

We also examined the mechanical properties of the CA samples. Figure 62 is the stress-strain curve of the CA film obtained using a universal testing machine. The measured elastic modulus of the CA was 419 MPa. With the relatively high elastic modulus, the nanostructured CA was stable in the water. Figure 63 represents the *in-situ* AFM image of the CA nanoneedle array submerged in DI water for 18 h. As shown, the CA nanoneedle could maintain its structural integrity even in underwater conditions without noticeable structural deformation. By considering the fact that antifouling materials are exposed to wet environments for a prolonged time, such mechanical stability is highly beneficial for the CA nanoneedle array to be used as a robust antifouling material. Furthermore, the fabricated film possessing the CA nanoneedle array was not only flexible but was also highly transparent (Figure 64). Therefore, our CA nanoneedle film can be used for a broad range of applications that require optical transparency and three-dimensional conformal attachment of anti-biofouling or anti-pathogenic film.

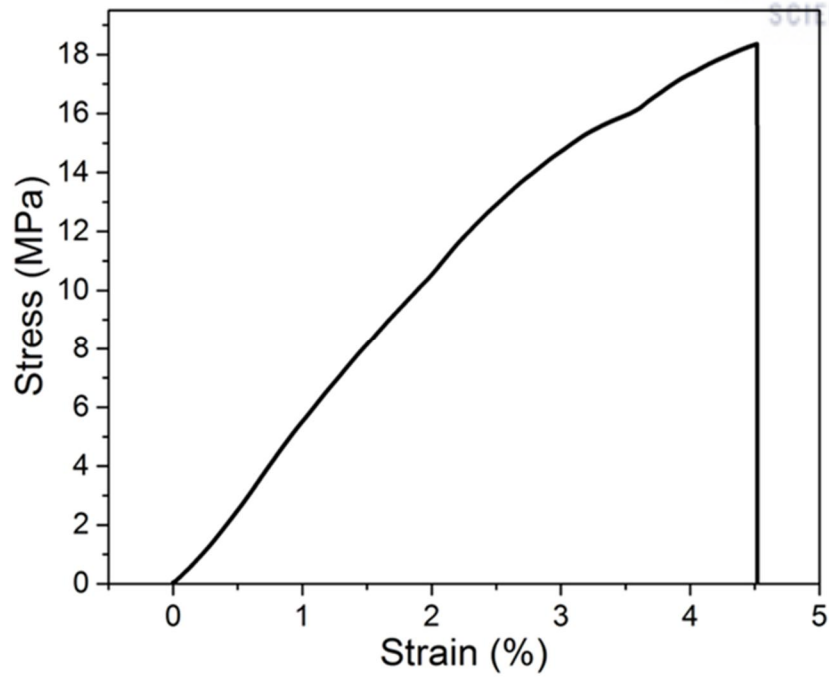


Figure 62. A stress-strain curve of the CA sample.

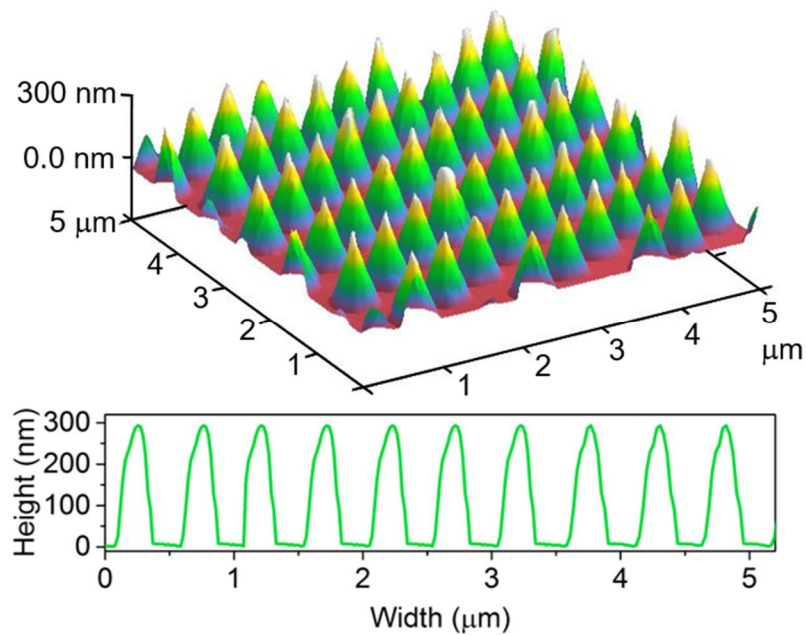


Figure 63. *In-situ* AFM image of the CA nanoneedle submerged in DI water for 18 h. The image was directly acquired from the submerged sample.

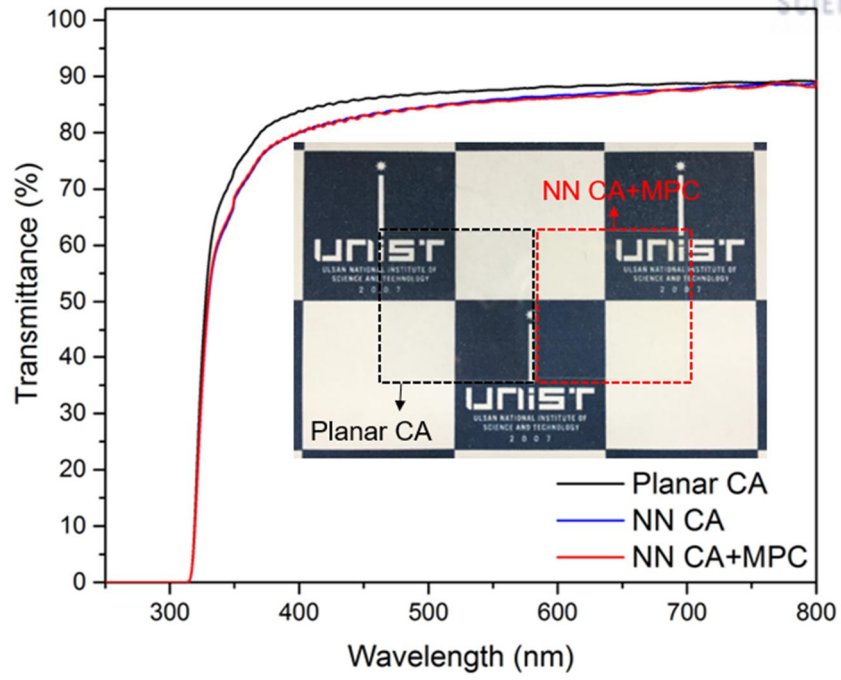


Figure 64. Optical transmittance of the pristine CA, CA nanoneedle, and MPC-coated CA nanoneedle samples in the wavelength range of 250-800 nm.

### 3.3.4. Evaluation of the biofilm-resistance of the MPC-coated cellulose acetate nanoneedle array

To evaluate the biofilm-resistance of the CA nanotopography, gram-negative (*E. coli*) and gram-positive (*B. subtilis*) bacteria were cultured on the planar glass, planar CA, CA nanoneedle, and MPC-coated CA nanoneedle samples. Figure 65 shows the fluorescence confocal microscopy images of *E. coli* grown on different substrates. As shown, after 18 h culture on the planar glass, a large number of live *E. coli* were adhered to the surface, as indicated by the green fluorescence (Figure 65-i). A slightly lower density of *E. coli* was observed on the planar CA sample as compared with that on the planar glass (Figure 65-ii), yet the difference was trivial. This indicates that CA does not possess noticeable, intrinsic bacterial repelling or killing properties [70, 73]. However, when the CA was shaped into a nanoscale needle-like architecture, very different bacterial behavior was observed on the nanostructured CA surface (Figure 65-iii). A high density of *E. coli* was observed on the nanostructured CA substrate. However, many of the attached *E. coli* were revealed as dead ones as evidenced by the red fluorescence (Figure 65-iii), indicating that strong bactericidal effects can be obtained only with the natural CA biopolymer by transforming the morphology of CA into a proper nanoscale architecture. This is because the nanostructured CA with sharp tips, with dimensions that are smaller than single microbes, induces physical damage and lysis in the cell membrane by penetrating or stretching the cell membrane [19]. Interestingly, when the CA nanoneedle array was coated with MPC via simple plasma polymerization, the number of adhered *E. coli* was remarkably reduced as compared to that on the flat CA or even the CA nanoneedle sample (Figure 65-iv). Although a few attached bacteria were observed on the MPC-treated CA nanoneedle, the majority of them were dead as indicated by the red fluorescence. These results show that nanostructured CA can simultaneously exhibit pronounced antibacterial (bacteria-killing) and antifouling (bacteria-repelling) properties, which could be simply achieved by integrating the MPC with the nanostructured CA. The remarkable bacterial film-resistant ability of the nanostructured CA was also observed against gram-positive bacteria of *B. subtilis* with an overall similar tendency with *E. coli* (Figure 66).

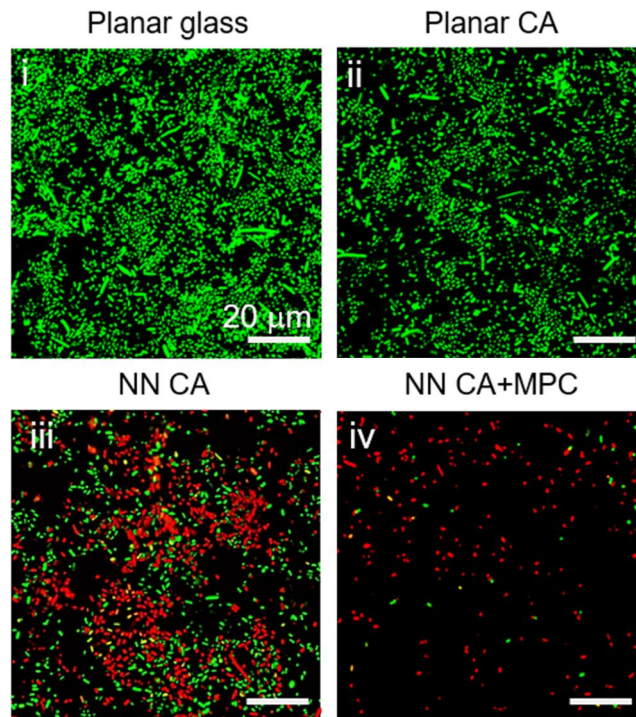


Figure 65. Confocal microscopy images of *E. coli* grown on the planar glass, planar CA, CA nanoneedle, and MPC-coated CA nanoneedle surfaces for 18 h. The bacteria were stained with a fluorescent labeling reagent.

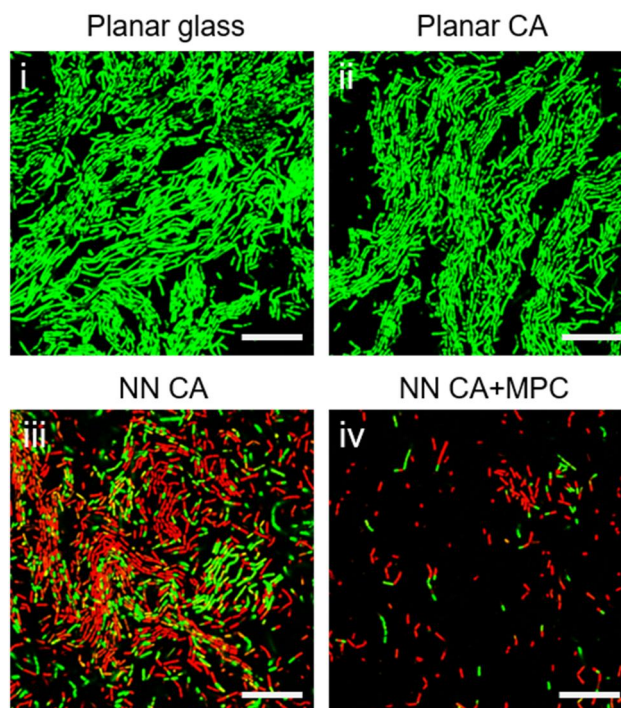


Figure 66. Confocal microscopy images of *B. subtilis* grown on the planar glass, planar CA, CA nanoneedle, and MPC-coated CA nanoneedle surfaces for 18 h. The bacteria were stained with a fluorescent labeling reagent.



For quantitative evaluation of the biofilm-resistant behavior of the CA nanoneedle array, we performed analysis of the areal coverage of bacteria and a colony forming unit (CFU) assay, as shown in Figure 67-i and 67-ii for *E. coli* and Figure 68-i and 68-ii for *B. subtilis*, respectively. The coverage area of live *E. coli* and *B. subtilis* on the CA nanoneedle were 59.8% and 64.7% lower as compared to those of each bacterial species on the planar CA. The coverage area of live *E. coli* and *B. subtilis* on the MPC-coated CA nanoneedle were further reduced to 0.394% and 1.041%, which is 97.8% and 97.2% lower compared with those on the planar CA, respectively. In addition, the CA nanoneedle and MPC-coated CA nanoneedle maintained its effective anti-biofilm performance during the 30 h of bacterial culture (Figure 67-ii, 68-ii). These fluorescence microscope imaging and quantitative analysis results clearly demonstrate that superior and robust antibiofilm properties are attainable with sustainable cellulose derivatives having proper nanoscale topographies.

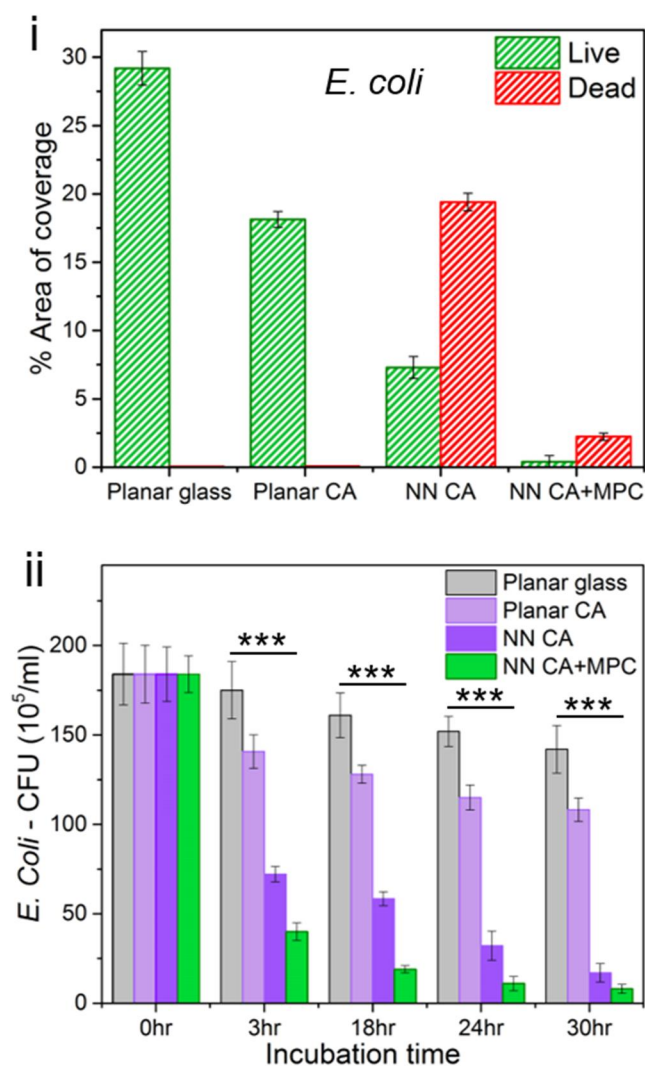


Figure 67. (i) Coverage area of the live (green) and dead (red) *E. coli* cultured on the control and various CA samples. (ii) CFU of the *E. coli* grown on the control and various CA samples after 0, 3, 18, 24, and 30 h culture ( $n = 9$ , \*  $p < 0.05$ , \*\*  $p < 0.01$ , and \*\*\*  $p < 0.001$  compared to control; data was analyzed by a one-way ANOVA).

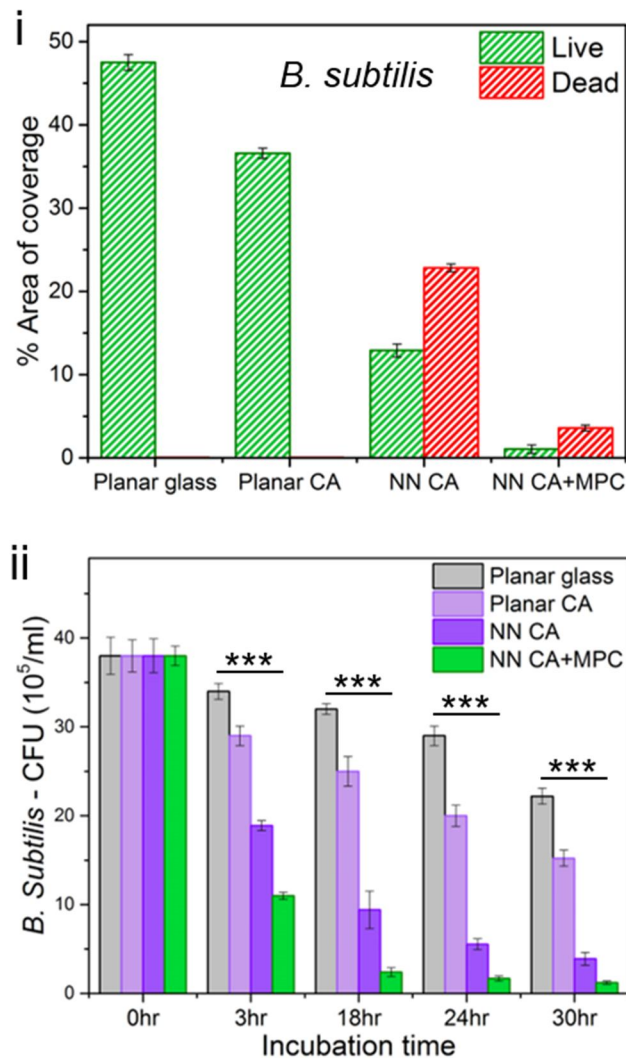


Figure 68. (i) Coverage area of the live (green) and dead (red) *B. subtilis* cultured on the control and various CA samples. (ii) CFU of the *B. subtilis* grown on the control and various CA samples after 0, 3, 18, 24, and 30 h culture ( $n = 9$ , \*  $p < 0.05$ , \*\*  $p < 0.01$ , and \*\*\*  $p < 0.001$  compared to control; data was analyzed by a one-way ANOVA).

### 3.3.5. Long-term evaluation of anti-biofouling performance on the MPC-grafted cellulose acetate nanoneedle

For long-term evaluation of the biofilm-resistant behavior of the MPC-grafted CA nanoneedle array, we performed analysis of the fluorescence confocal microscopy images of bacteria and a colony forming unit (CFU) with a new strain of bacteria. *Pseudomonas aeruginosa* (*P. aeruginosa*) is a gram-negative, ubiquitous environmental bacterium which also is a human pathogen that can cause a wide range of life-threatening acute and chronic infections. Figure 69-i shows the fluorescence confocal microscopy images of *P. aeruginosa* grown on different substrates. As shown, after 28 d culture on the planar glass, a number of live *P. aeruginosa* were attached to the surface, as indicated by the green fluorescence. A lower density of *P. aeruginosa* was observed on the planar CA sample as compared with that on the planar glass. Many of the attached *P. aeruginosa* were revealed on the CA nanoneedles as dead ones as evidenced by the red fluorescence, indicating that strong bactericidal effects can be obtained. Although a few attached bacteria were observed on the MPC-treated CA nanoneedle, the majority of them were dead as indicated by the red fluorescence.

For quantitative evaluation of the biofilm-resistant behavior of the CA nanoneedle array, we performed analysis of colony forming unit (CFU) assay, as shown in Figure 69-ii for *P. aeruginosa*. The CA nanoneedle and MPC-coated CA nanoneedle maintained its effective anti-biofilm performance during the 28 d of bacterial culture. These results show that MPC-treated CA nanoneedle can simultaneously exhibit pronounced antibacterial (bacteria-killing) and antifouling (bacteria-repelling) properties.

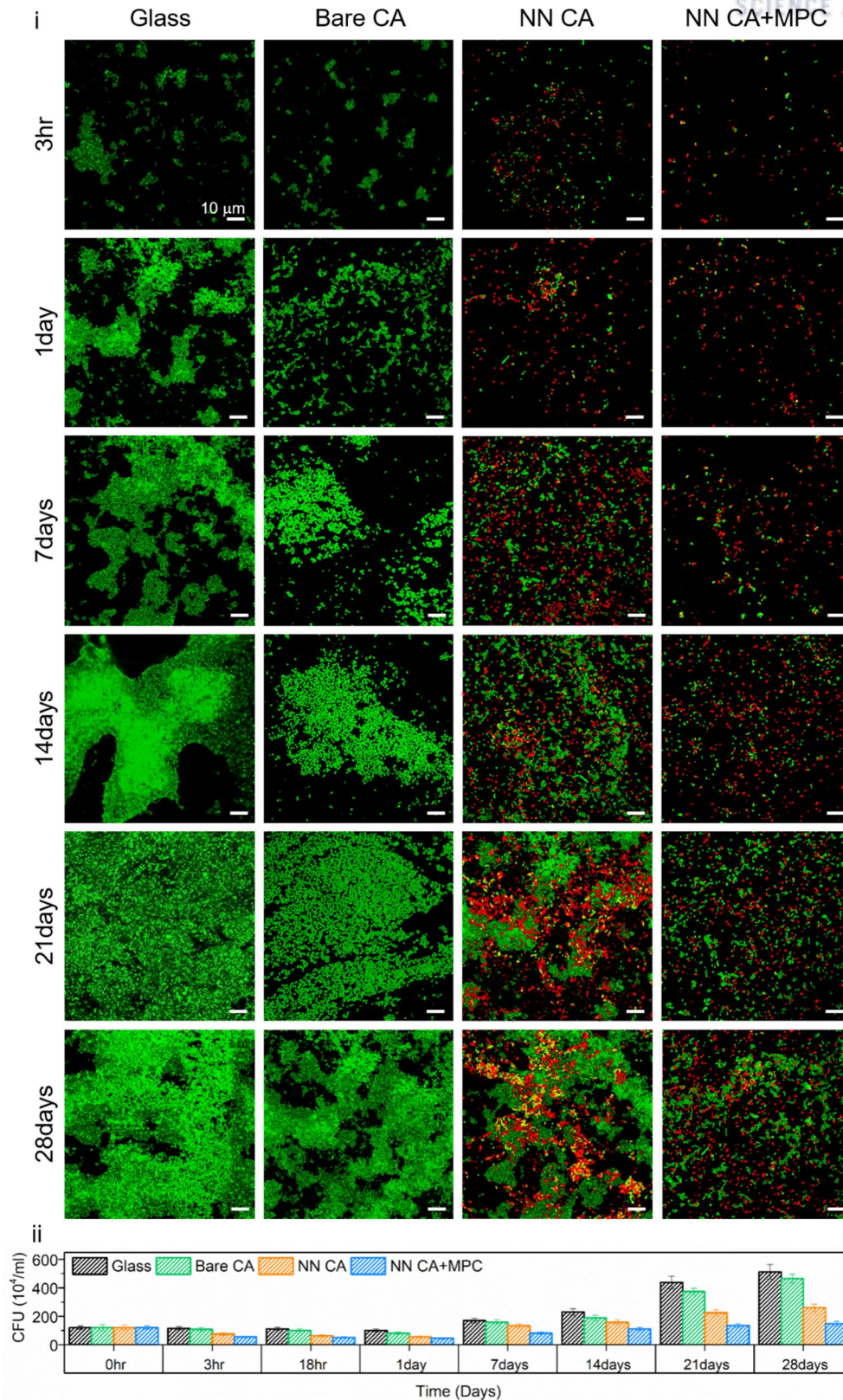


Figure 69. (i) Confocal microscopy images of *P. aeruginosa* grown on the planar glass, planar CA, CA nanoneedle, and MPC-coated CA nanoneedle surfaces for 28 d. The bacteria were stained with a fluorescent labeling reagent. (ii) CFU of the *P. aeruginosa* grown on the control and various CA samples after 0 h, 3 h, 18 h, 1 d, 7 d, 14 d, 21 d, and 28 d culture.



### 3.4. Summary

In summary, we have presented a sustainable antibiofilm material made of a naturally abundant, biocompatible, and biodegradable CA. A CA nanostructure array having sharp tips with a tip diameter of 50 nm could be fabricated based on a nanomolding technique using CA as the base material in a simple and reproducible manner. Due to the negatively charged polyion layer of the plasma-treated CA, the surface of the CA nanostructure could be functionalized with MPC via a facile plasma polymerization mechanism. Based on the unique integrated architecture of the highly biocompatible and environmentally friendly cellulose derivative, bioinspired MPC, and nanoscale topography incorporated in a single flexible film, this integrated cellulose derivative material exhibited remarkable simultaneous repelling and -killing capabilities for both gram-negative and gram-positive bacteria, which efficiently and reliably prevented formation of bacterial biofilms. Considering the burgeoning interest in safe and eco-friendly materials, the cellulose derivative-based biofilm-resistant materials proposed in this study should serve as a versatile biocompatible, biodegradable, and environment-friendly antibiofilm material for every-day, biomedical, and industrial applications. For example, the highly flexible film with MPC-coated CA nanoneedles can be applied to the curved or non-planar surfaces of diverse biomedical devices. Currently, bacterial adhesion and biofilm formation on biomedical devices, such as catheters, lead to device-associated infections, resulting in significant morbidity and mortality. The MPC-functionalized CA nanoneedles with outstanding biofilm-resistance, biocompatibility, and biodegradability have the potential to address such critical problems and contribute to the enhancement of public health.



## 4. Conclusions and Perspectives

In conclusion, I proposed a chemical/mechanical hybrid antifouling strategy using biocompatible antifouling materials with high mechanical durability and applicable to three-dimensional surfaces.

The first research goal was to select biocompatible materials with antifouling function. I chose PEGDMA and CA, which are biocompatible materials and eco-friendly materials, to make antifouling surfaces. The selected materials had mechanical stability, low cost, and good flexibility. Due to the flexibility of the base material, it can be applied to various 3D surfaces and large areas, and antifouling nano-structural surfaces can be used.

The second research goal was to fabricate mechanically durable nanostructures that mimic the nanostructures of a cicada wing having a bactericidal function. Nanostructures had excellent antibacterial properties by damaging cell membranes regardless of the type of bacteria. The nanostructured surface, which mimicked the cicada wing, was easily fabricated by UV molding and soft lithography. Based on the nanostructure of the cicada wing, the structure spacing was adjusted and optimized to maximize the antibacterial performance. The fabricated nanostructures were observed and measured by SEM, AFM and TEM.

The third research goal was to enhance the antifouling and bactericidal function of the covalently bonded MPC and nanostructured surfaces for long term anti-biofouling durability. In order to maximize the antifouling properties on the surface of the fabricated nanostructures, MPC was coated as a zwitterionic material with excellent antifouling properties after oxygen plasma treatment. Surface chemical analysis was performed through FT-IR, XPS, and contact angle to confirm stable surface coating, and it was proved that MPC is stably covalently bonded on the fabricated surface. The coating surface of MPC was the primary antifouling surface that can be minimized the adhesion of bacteria, so the excellent antifouling properties were confirmed through the bacteria adhesion experiments. In addition, cell lysis due to nanostructures was observed through SEM, TEM, and AFM to confirm the physical interaction between nanostructures and bacterial membranes.

The final research goal was to ensure the long-term anti-biofouling performance of hybrid surfaces with anti-biofouling function, as well as strong resistance to external stimuli, and to suggest the potential for use in the medical and marine industries. When the MPC was damaged or the PEGDMA surface was damaged by external stimuli, it showed strong antifouling durability against bacterial attachment of gram-negative and gram-positive bacteria on the damaged antifouling surface. In addition, due to the stable coating of the MPC and the bactericidal function of the nanostructures, hybrid anti-biofouling surfaces proved superior antifouling function compared to single function surfaces when testing bacteria for a long time (28 days). Quantification of the antifouling performance of *E. coli*, *B. subtilis* and *P. aeruginosa* was performed using % area coverage and CFU.

In this study, nanostructured surface with the excellent bactericidal function was fabricated using biocompatible antifouling materials, and by covalently coating the amphiphilic material thinner once more, a surface having an antifouling function that can be used for a long time was realized.

Many of the researches reported so far could only be produced under laboratory conditions using sophisticated instruments and relatively complex procedures, which are difficult to apply to actual medical and marine

industries. Simple, cost-effective, environmentally friendly and reproducible fabrication methods are needed, and these important design criteria should be considered in future studies. While coping with these important challenges may require collaborative efforts by researchers in the fields of surface chemistry, materials science, biomedical engineering and biotechnology, the research should provide many opportunities for innovation beyond antibacterial surfaces.

## References

- [1] S.S. Magill, J.R. Edwards, W. Bamberg, Z.G. Beldavs, G. Dumyati, M.A. Kainer, R. Lynfield, M. Maloney, L. McAllister-Hollod, J. Nadle, "Multistate point-prevalence survey of health care-associated infections," *J New England Journal of Medicine*, vol. 370, pp. 1198-1208, 2014.
- [2] R.H. Dahal, D.K. Chaudhary, "Microbial infections and antimicrobial resistance in Nepal: current trends and recommendations," *The open microbiology journal*, vol. 12, pp. 230, 2018.
- [3] J.M. Boiano, A.L. Steege, "Ethylene oxide and hydrogen peroxide gas plasma sterilization: Precautionary practices in US hospitals," *Zentralsterilisation*, vol. 23, pp. 262, 2015.
- [4] R.S. Peres, A.F. Baldissera, E. Armelin, C. Alemán, C.A. Ferreira, "Marine-friendly antifouling coating based on the use of a fatty acid derivative as a pigment," *Materials Research*, vol. 17, pp. 720-727, 2014.
- [5] A.G. Nurioglu, A.C.C. Esteves, "Non-toxic, non-biocide-release antifouling coatings based on molecular structure design for marine applications," *J Mater Chem B*, vol. 3, pp. 6547-6570, 2015.
- [6] T. Wei, Z. Tang, Q. Yu, H. Chen, "Smart antibacterial surfaces with switchable bacteria-killing and bacteria-releasing capabilities," *ACS applied materials interfaces*, vol. 9, pp. 37511-37523, 2017.
- [7] S. Lowe, N.M. O'Brien-Simpson, L.A. Connal, "Antibiofouling polymer interfaces: poly (ethylene glycol) and other promising candidates," *Polymer Chemistry*, vol. 6, pp. 198-212, 2015.
- [8] K.W. Kolewe, S.R. Peyton, J.D. Schiffman, "Fewer bacteria adhere to softer hydrogels," *ACS applied materials interfaces*, vol. 7, pp. 19562-19569, 2015.
- [9] M. He, K. Gao, L. Zhou, Z. Jiao, M. Wu, J. Cao, X. You, Z. Cai, Y. Su, Z. Jiang, "Zwitterionic materials for antifouling membrane surface construction," *Acta biomaterialia*, vol. 40, pp. 142-152, 2016.
- [10] W.G. Herrick, T.V. Nguyen, M. Sleiman, S. McRae, T.S. Emrick, S.R. Peyton, "PEG-phosphorylcholine hydrogels as tunable and versatile platforms for mechanobiology," *Biomacromolecules*, vol. 14, pp. 2294-2304, 2013.
- [11] W.R. Gombotz, W. Guanghai, T.A. Horbett, A.S. Hoffman, "Protein adsorption to poly (ethylene oxide) surfaces," *J Biomed Mater Res*, vol. 25, pp. 1547-1562, 1991.
- [12] H.-H. Park, K. Sun, M. Seong, M. Kang, S. Park, S. Hong, H. Jung, J. Jang, J. Kim, H.E. Jeong, "Lipid-Hydrogel-Nanostructure Hybrids as Robust Biofilm-Resistant Polymeric Materials," *ACS Macro Letters*, vol. 8, pp. 64-69, 2018.
- [13] K. Baek, J. Liang, W.T. Lim, H. Zhao, D.H. Kim, H. Kong, "In situ assembly of antifouling/bacterial silver nanoparticle-hydrogel composites with controlled particle release and matrix softening," *ACS applied materials & interfaces*, vol. 7, pp. 15359-15367, 2015.
- [14] D.O. Schairer, J.S. Chouake, J.D. Nosanchuk, A.J. Friedman, "The potential of nitric oxide releasing therapies as antimicrobial agents," *Virulence*, vol. 3, pp. 271-279, 2012.
- [15] E.P. Ivanova, J. Hasan, H.K. Webb, V.K. Truong, G.S. Watson, J.A. Watson, V.A. Baulin, S. Pogodin, J.Y. Wang, M.J. Tobin, "Natural bactericidal surfaces: mechanical rupture of *Pseudomonas aeruginosa* cells by

cicada wings," *Small*, vol. 8, pp. 2489-2494, 2012.

[16] C.D. Bandara, S. Singh, I.O. Afara, A. Wolff, T. Tesfamichael, K. Ostrikov, A. Oloyede, "Bactericidal effects of natural nanotopography of dragonfly wing on Escherichia coli," *ACS applied materials interfaces*, vol. 9, pp. 6746-6760, 2017.

[17] S.M. Kelleher, O. Habimana, J. Lawler, B. O'reilly, S. Daniels, E. Casey, A. Cowley, "Cicada wing surface topography: an investigation into the bactericidal properties of nanostructural features," *ACS applied materials interfaces*, vol. 8, pp. 14966-14974, 2015.

[18] A. Tripathy, P. Sen, B. Su, W.H. Briscoe, "Natural and bioinspired nanostructured bactericidal surfaces," *Advances in colloid interface science*, vol. 248, pp. 85-104, 2017.

[19] E.P. Ivanova, J. Hasan, H.K. Webb, G. Gervinskas, S. Juodkazis, V.K. Truong, A.H. Wu, R.N. Lamb, V.A. Baulin, G.S. Watson, "Bactericidal activity of black silicon," *Nat Commun*, vol. 4, pp. 2838, 2013.

[20] C.M. Bhadra, V.K. Truong, V.T. Pham, M. Al Kobaisi, G. Seniutinas, J.Y. Wang, S. Juodkazis, R.J. Crawford, E.P. Ivanova, "Antibacterial titanium nano-patterned arrays inspired by dragonfly wings," *Sci Rep*, vol. 5, pp. 16817, 2015.

[21] I.S. Kurtz, J.D. Schiffman, "Current and emerging approaches to engineer antibacterial and antifouling electrospun nanofibers," *Materials*, vol. 11, pp. 1059, 2018.

[22] M. Cloutier, D. Mantovani, F. Rosei, "Antibacterial coatings: challenges, perspectives, and opportunities," *Trends in biotechnology*, vol. 33, pp. 637-652, 2015.

[23] H.E. Jeong, I. Kim, P. Karam, H.-J. Choi, P. Yang, "Bacterial recognition of silicon nanowire arrays," *Nano Lett*, vol. 13, pp. 2864-2869, 2013.

[24] H. Zhang, M. Chiao, "Anti-fouling coatings of poly (dimethylsiloxane) devices for biological and biomedical applications," *Journal of medical biological engineering*, vol. 35, pp. 143-155, 2015.

[25] K. Yang, H. Jung, H.-R. Lee, J.S. Lee, S.R. Kim, K.Y. Song, E. Cheong, J. Bang, S.G. Im, S.-W. Cho, "Multiscale, hierarchically patterned topography for directing human neural stem cells into functional neurons," *Acs Nano*, vol. 8, pp. 7809-7822, 2014.

[26] W.-G. Bae, J. Kim, Y.-H. Choung, Y. Chung, K.Y. Suh, C. Pang, J.H. Chung, H.E. Jeong, "Bio-inspired configurable multiscale extracellular matrix-like structures for functional alignment and guided orientation of cells," *Biomaterials*, vol. 69, pp. 158-164, 2015.

[27] J.H. Lee, H.B. Lee, J.D. Andrade, "Blood compatibility of polyethylene oxide surfaces," *Progress in polymer science*, vol. 20, pp. 1043-1079, 1995.

[28] S. Yang, S.P. Zhang, F.M. Winnik, F. Mwale, Y.K.J.J.o.B.M.R.P.A.A.O.J.o.T.S.f.B. Gong, The Japanese Society for Biomaterials,, "Group reorientation and migration of amphiphilic polymer bearing phosphorylcholine functionalities on surface of cellular membrane mimicking coating," *J Biomed Mater Res A*, vol. 84, pp. 837-841, 2008.

[29] K. Ishihara, Y. Iwasaki, S. Ebihara, Y. Shindo, N. Nakabayashi, "Photoinduced graft polymerization of 2-methacryloyloxyethyl phosphorylcholine on polyethylene membrane surface for obtaining blood cell adhesion resistance," *Colloids Surfaces B*, vol. 18, pp. 325-335, 2000.

- [30] X. Ding, C. Yang, T.P. Lim, L.Y. Hsu, A.C. Engler, J.L. Hedrick, Y.-Y. Yang, "Antibacterial and antifouling catheter coatings using surface grafted PEG-b-cationic polycarbonate diblock copolymers," *Biomaterials*, vol. 33, pp. 6593-6603, 2012.
- [31] G. Donelli, *Biofilm-based healthcare-associated infections*, Springer 2014.
- [32] H.-H. Park, M. Seong, K. Sun, H. Ko, S.M. Kim, H.E. Jeong, "Flexible and shape-reconfigurable hydrogel interlocking adhesives for high adhesion in wet environments based on anisotropic swelling of hydrogel microstructures," *ACS Macro Letters*, vol. 6, pp. 1325-1330, 2017.
- [33] H. Yi, M. Seong, K. Sun, I. Hwang, K. Lee, C. Cha, T.i. Kim, H.E. Jeong, "Wet Responsive, Reconfigurable, and Biocompatible Hydrogel Adhesive Films for Transfer Printing of Nanomembranes," *Adv Funct Mater*, vol. 28, pp. 1706498, 2018.
- [34] Y. Dang, M. Quan, C.-M. Xing, Y.-B. Wang, Y.-K. Gong, "Biocompatible and antifouling coating of cell membrane phosphorylcholine and mussel catechol modified multi-arm PEGs," *J Mater Chem B*, vol. 3, pp. 2350-2361, 2015.
- [35] F. Götz, "Staphylococcus and biofilms," *Molecular microbiology*, vol. 43, pp. 1367-1378, 2002.
- [36] S.-J. Choi, P.J. Yoo, S.J. Baek, T.W. Kim, H.H. Lee, "An ultraviolet-curable mold for sub-100-nm lithography," *Journal of the American Chemical Society*, vol. 126, pp. 7744-7745, 2004.
- [37] Y. Inoue, Y. Onodera, K. Ishihara, "Preparation of a thick polymer brush layer composed of poly (2-methacryloyloxyethyl phosphorylcholine) by surface-initiated atom transfer radical polymerization and analysis of protein adsorption resistance," *Colloids Surfaces B*, vol. 141, pp. 507-512, 2016.
- [38] T. Moro, Y. Takatori, M. Kyomoto, K. Ishihara, K.-i. Saiga, K. Nakamura, H. Kawaguchi, "Surface grafting of biocompatible phospholipid polymer MPC provides wear resistance of tibial polyethylene insert in artificial knee joints," *Osteoarthritis cartilage*, vol. 18, pp. 1174-1182, 2010.
- [39] J.A. Killion, L.M. Geever, D.M. Devine, J.E. Kennedy, C.L. Higginbotham, "Mechanical properties and thermal behaviour of PEGDMA hydrogels for potential bone regeneration application," *Journal of the mechanical behavior of biomedical materials*, vol. 4, pp. 1219-1227, 2011.
- [40] Y.-H. Wu, H.B. Park, T. Kai, B.D. Freeman, D.S. Kalika, "Water uptake, transport and structure characterization in poly (ethylene glycol) diacrylate hydrogels," *J Membrane Sci*, vol. 347, pp. 197-208, 2010.
- [41] K.W. Kolewe, J. Zhu, N.R. Mako, S.S. Nonnenmann, J.D. Schiffman, "Bacterial adhesion is affected by the thickness and stiffness of poly (ethylene glycol) hydrogels," *ACS applied materials interfaces*, vol. 10, pp. 2275-2281, 2018.
- [42] S.-Y. Lin, V.R. Parasuraman, S.L. Mekuria, S. Peng, H.-C. Tsai, G.-H. Hsiue, "Plasma initiated graft polymerization of 2-methacryloyloxyethyl phosphorylcholine on silicone elastomer surfaces to enhance bio (hemo) compatibility," *Surface Coatings Technology*, vol. 315, pp. 342-349, 2017.
- [43] P. Kingshott, H. Thissen, H.J. Griesser, "Effects of cloud-point grafting, chain length, and density of PEG layers on competitive adsorption of ocular proteins," *Biomaterials*, vol. 23, pp. 2043-2056, 2002.



- [44] S. Tristram-Nagle, Y. Liu, J. Legleiter, J.F. Nagle, "Structure of gel phase DMPC determined by X-ray diffraction," *Biophys J*, vol. 83, pp. 3324-3335, 2002.
- [45] K.W. Kolewe, K.M. Dobosz, T. Emrick, S.S. Nonnenmann, J.D. Schiffman, "Fouling-Resistant Hydrogels Prepared by the Swelling-Assisted Infusion and Polymerization of Dopamine," *ACS applied bio materials*, vol. 1, pp. 33-41, 2018.
- [46] A. Al-Jumaili, S. Alancherry, K. Bazaka, M.V. Jacob, "Review on the Antimicrobial Properties of Carbon Nanostructures," *Materials*, vol. 10, pp. 2017.
- [47] D.E. Fullenkamp, J.G. Rivera, Y.K. Gong, K.H.A. Lau, L.H. He, R. Varshney, P.B. Messersmith, "Mussel-inspired silver-releasing antibacterial hydrogels," *Biomaterials*, vol. 33, pp. 3783-3791, 2012.
- [48] S. Kang, M. Herzberg, D.F. Rodrigues, M. Elimelech, "Antibacterial effects of carbon nanotubes: Size does matter," *Langmuir*, vol. 24, pp. 6409-6413, 2008.
- [49] T. Liu, B. Yin, T. He, N. Guo, L.H. Dong, Y.S. Yin, "Complementary Effects of Nanosilver and Superhydrophobic Coatings on the Prevention of Marine Bacterial Adhesion," *Acs Applied Materials & Interfaces*, vol. 4, pp. 4683-4690, 2012.
- [50] N. Padmavathy, P.K. Samantaray, L.D. Ghosh, G. Madras, S.J.N. Bose, "Selective cleavage of the polyphosphoester in crosslinked copper based nanogels: enhanced antibacterial performance through controlled release of copper," *Nanoscale*, vol. 9, pp. 12664-12676, 2017.
- [51] W.W. Yang, J. Li, P. Zhou, L.H. Zhu, H.Q. Tang, "Superhydrophobic copper coating: Switchable wettability, on-demand oil-water separation, and antifouling," *Chem Eng J*, vol. 327, pp. 849-854, 2017.
- [52] A.P. Francis, T. Devasena, "Toxicity of carbon nanotubes: A review," *Toxicol Ind Health*, vol. 34, pp. 200-210, 2018.
- [53] Muhammadi, Shabina, M. Afzal, S. Hameed, "Bacterial polyhydroxyalkanoates-eco-friendly next generation plastic: production, biocompatibility, biodegradation, physical properties and applications," *Green Chemistry Letters and Reviews*, vol. 8, pp. 56-77, 2015.
- [54] C.F. Ma, W.P. Zhang, G.Z. Zhang, P.Y. Qian, "Environmentally Friendly Antifouling Coatings Based on Biodegradable Polymer and Natural Antifoulant," *Acs Sustain Chem Eng*, vol. 5, pp. 6304-6309, 2017.
- [55] F. Zentz, C. Hellio, A. Valla, D. De La Broise, G. Bremer, R. Labia, "Antifouling activities of N-substituted imides: Antimicrobial activities and inhibition of *Mytilus edulis* phenoloxidase," *Mar Biotechnol*, vol. 4, pp. 431-440, 2002.
- [56] X. Ding, C. Yang, T.P. Lim, L.Y. Hsu, A.C. Engler, J.L. Hedrick, Y.Y. Yang, "Antibacterial and antifouling catheter coatings using surface grafted PEG-b-cationic polycarbonate diblock copolymers," *Biomaterials*, vol. 33, pp. 6593-6603, 2012.
- [57] T. Kang, X. Banquy, J.H. Heo, C.N. Lim, N.A. Lynd, P. Lundberg, D.X. Oh, H.K. Lee, Y.K. Hong, D.S. Hwang, J.H. Waite, J.N. Israelachvili, C.J. Hawker, "Mussel-Inspired Anchoring of Polymer Loops That Provide Superior Surface Lubrication and Antifouling Properties," *Acs Nano*, vol. 10, pp. 930-937, 2016.
- [58] C. Yang, X. Ding, R.J. Ono, H. Lee, L.Y. Hsu, Y.W. Tong, J. Hedrick, Y.Y. Yang, "Brush-Like Polycarbonates Containing Dopamine, Cations, and PEG Providing a Broad-Spectrum, Antibacterial, and

- Antifouling Surface via One-Step Coating," *Adv Mater*, vol. 26, pp. 7346-7351, 2014.
- [59] Q.H. Zhang, J.X. Jiang, F. Gao, G.F. Zhang, X.L. Zhan, F.Q. Chen, "Engineering high-effective antifouling polyether sulfone membrane with P(PEG-PDMS-KH570)@SiO<sub>2</sub> nanocomposite via in-situ sol-gel process," *Chem Eng J*, vol. 321, pp. 412-423, 2017.
- [60] R. Zhang, Y. Liu, M. He, Y. Su, X. Zhao, M. Elimelech, Z. Jiang, "Antifouling membranes for sustainable water purification: strategies and mechanisms," *Chemical Society Reviews*, vol. 45, pp. 5888-5924, 2016.
- [61] B.K.D. Ngo, M.A. Grunlan, "Protein Resistant Polymeric Biomaterials," *Acs Macro Letters*, vol. 6, pp. 992-1000, 2017.
- [62] C.M. Bhadra, V.K. Truong, V.T.H. Pham, M. Al Kobaisi, G. Seniutinas, J.Y. Wang, S. Juodkazis, R.J. Crawford, E.P. Ivanova, "Antibacterial titanium nano-patterned arrays inspired by dragonfly wings," *Sci Rep-Uk*, vol. 5, pp. 2015.
- [63] G. Hazell, P.W. May, P. Taylor, A.H. Nobbs, C.C. Welch, B. Su, "Studies of black silicon and black diamond as materials for antibacterial surfaces," *Biomater Sci-Uk*, vol. 6, pp. 1424-1432, 2018.
- [64] E. Ozkan, C.C. Crick, A. Taylor, E. Allan, I.P. Parkin, "Copper-based water repellent and antibacterial coatings by aerosol assisted chemical vapour deposition," *Chem Sci*, vol. 7, pp. 5126-5131, 2016.
- [65] Y.K. Bai, Y.J. Liu, Q.H. Wang, "Cellulose Acetate for Shape Memory Polymer: Natural, Simple, High Performance, and Recyclable," *Adv Polym Tech*, vol. 37, pp. 21732, 2018.
- [66] Y. Habibi, L.A. Lucia, O.J. Rojas, "Cellulose Nanocrystals: Chemistry, Self-Assembly, and Applications," *Chem Rev*, vol. 110, pp. 3479-3500, 2010.
- [67] J.O. Zoppe, M.S. Peresin, Y. Habibi, R.A. Venditti, O.J.J.A.a.m. Rojas, interfaces, "Reinforcing poly ( $\epsilon$ -caprolactone) nanofibers with cellulose nanocrystals," *ACS applied materials & interfaces*, vol. 1, pp. 1996-2004, 2009.
- [68] B.X. Han, D.L. Zhang, Z.Q. Shao, L.L. Kong, S.Y. Lv, "Preparation and characterization of cellulose acetate/carboxymethyl cellulose acetate blend ultrafiltration membranes," *Desalination*, vol. 311, pp. 80-89, 2013.
- [69] J.M. Joubert, G.J.R. Krige, K. Borgin, "Evidence for a Hydrate of Cellulose from Studies of Its Surface Properties," *Nature*, vol. 184, pp. 1561-1562, 1959.
- [70] T. Mohan, R. Kargl, K.E. Tradt, M.R. Kulterer, M. Bracic, S. Hribernik, K. Stana-Kleinschek, V. Ribitsch, "Antifouling coating of cellulose acetate thin films with polysaccharide multilayers," *Carbohydrate Polymers*, vol. 116, pp. 149-158, 2015.
- [71] D.G. Yu, X.Y. Li, X. Wang, W. Chian, Y.Z. Liao, Y. Li, "Zero-order drug release cellulose acetate nanofibers prepared using coaxial electrospinning," *Cellulose*, vol. 20, pp. 379-389, 2013.
- [72] T. Mohan, R. Kargl, K.E. Tradt, M.R. Kulterer, M. Bračić, S. Hribernik, K. Stana-Kleinschek, V. Ribitsch, "Antifouling coating of cellulose acetate thin films with polysaccharide multilayers," *Carbohydrate polymers*, vol. 116, pp. 149-158, 2015.
- [73] W.Z. Xu, G. Gao, J.F. Kadla, "Synthesis of antibacterial cellulose materials using a "clickable" quaternary ammonium compound," *Cellulose*, vol. 20, pp. 1187-1199, 2013.

- [74] H. Abou-Yousef, E. Saber, M.S. Abdel-Aziz, S. Kamel, "Efficient alternative of antimicrobial nanocomposites based on cellulose acetate/Cu-NPs," *Soft Materials*, vol. 16, pp. 141-150, 2018.
- [75] A.W. Jatoi, I.S. Kim, Q.-Q. Ni, "Cellulose acetate nanofibers embedded with AgNPs anchored TiO<sub>2</sub> nanoparticles for long term excellent antibacterial applications," *Carbohydrate polymers*, vol. 207, pp. 640-649, 2019.
- [76] M.S.S.A. Saraswathi, D. Rana, S. Alwarappan, S. Gowrishankar, P. Kanimozhi, A. Nagendran, "Cellulose acetate ultrafiltration membranes customized with bio-inspired polydopamine coating and in situ immobilization of silver nanoparticles," *New J Chem*, vol. 43, pp. 4216-4225, 2019.
- [77] L.N. Nthunya, M.L. Masheane, S.P. Malinga, E.N. Nxumalo, T.G. Barnard, M. Kao, Z.N. Tetana, S.D. Mhlanga, "Greener approach to prepare electrospun antibacterial  $\beta$ -cyclodextrin/cellulose acetate nanofibers for removal of bacteria from water," *ACS Sustainable Chemistry Engineering*, vol. 5, pp. 153-160, 2016.
- [78] J.A. Wahab, I.S. Kim, Q.Q. Ni, "A comparative study on synthesis of AgNPs on cellulose nanofibers by thermal treatment and DMF for antibacterial activities," *Mat Sci Eng C-Mater*, vol. 98, pp. 1179-1195, 2019.
- [79] K. Ishihara, T. Ueda, N. Nakabayashi, "Preparation of phospholipid polylners and their properties as polymer hydrogel membranes," *Polymer Journal*, vol. 22, pp. 355, 1990.
- [80] T. Moro, Y. Takatori, K. Ishihara, T. Konno, Y. Takigawa, T. Matsushita, U.I. Chung, K. Nakamura, H. Kawaguchi, "Surface grafting of artificial joints with a biocompatible polymer for preventing periprosthetic osteolysis," *Nat Mater*, vol. 3, pp. 829-836, 2004.
- [81] S.H. Ye, J. Watanabe, Y. Iwasaki, K. Ishihara, "Antifouling blood purification membrane composed of cellulose acetate and phospholipid polymer," *Biomaterials*, vol. 24, pp. 4143-4152, 2003.
- [82] S. Zhang, P. Rolfe, G. Wright, W. Lian, A. Milling, S. Tanaka, K. Ishihara, "Physical and biological properties of compound membranes incorporating a copolymer with a phosphorylcholine head group," *Biomaterials*, vol. 19, pp. 691-700, 1998.
- [83] R. Kwak, H.-H. Park, H. Ko, M. Seong, M.K. Kwak, H.E. Jeong, "Partially cured photopolymer with gradient bingham plastic behaviors as a versatile deformable material," *ACS Macro Letters*, vol. 6, pp. 561-565, 2017.
- [84] H. Yi, I. Hwang, J.H. Lee, D. Lee, H. Lim, D. Tahk, M. Sung, W.-G. Bae, S.-J. Choi, M.K. Kwak, "Continuous and scalable fabrication of bioinspired dry adhesives via a roll-to-roll process with modulated ultraviolet-curable resin," *ACS applied materials & interfaces*, vol. 6, pp. 14590-14599, 2014.
- [85] C. Lim, S. Park, J. Park, J. Ko, D.W. Lee, D.S. Hwang, "Probing nanomechanical interaction at the interface between biological membrane and potentially toxic chemical," *J Hazard Mater*, vol. 353, pp. 271-279, 2018.
- [86] K. Morigaki, H. Schönherr, C.W. Frank, W. Knoll, "Photolithographic polymerization of diacetylene-containing phospholipid bilayers studied by multimode atomic force microscopy," *Langmuir*, vol. 19, pp. 6994-7002, 2003.
- [87] K. Morigaki, H. Schönherr, T. Okazaki, "Polymerization of diacetylene phospholipid bilayers on solid substrate: Influence of the film deposition temperature," *Langmuir*, vol. 23, pp. 12254-12260, 2007.

- [88] N. Vogel, S. Utech, G.T. England, T. Shirman, K.R. Phillips, N. Koay, I.B. Burgess, M. Kolle, D.A. Weitz, J. Aizenberg, "Color from hierarchy: Diverse optical properties of micron-sized spherical colloidal assemblies," *P Natl Acad Sci USA*, vol. 112, pp. 10845-10850, 2015.
- [89] A. Salama, A. Mohamed, N.M. Aboamera, T. Osman, A. Khattab, "Characterization and mechanical properties of cellulose acetate/carbon nanotube composite nanofibers," *Adv Polym Tech*, vol. 37, pp. 2446-2451, 2018.
- [90] J.L. Song, N.L. Birbach, J.P. Hinstroza, "Deposition of silver nanoparticles on cellulosic fibers via stabilization of carboxymethyl groups," *Cellulose*, vol. 19, pp. 411-424, 2012.
- [91] S.P. Kusumocahyo, T. Kanamori, T. Iwatsubo, K. Sumaru, T. Shinbo, "Development of polyion complex membranes based on cellulose acetate modified by oxygen plasma treatment for pervaporation," *J Membrane Sci*, vol. 208, pp. 223-231, 2002.
- [92] A. Calvimontes, P. Mauersberger, M. Nitschke, V. Dutschk, F. Simon, "Effects of oxygen plasma on cellulose surface," *Cellulose*, vol. 18, pp. 803-809, 2011.
- [93] Z. Hua, R. Sitaru, F. Denes, R. Young, "Mechanisms of oxygen-and argon-RF-plasma-induced surface chemistry of cellulose," *Plasmas and polymers*, vol. 2, pp. 199-224, 1997.
- [94] Z. Persin, A. Vesel, K.S. Kleinschek, M. Mozetic, "Characterisation of surface properties of chemical and plasma treated regenerated cellulose fabric," *Text Res J*, vol. 82, pp. 2078-2089, 2012.
- [95] L. Surdu, M.D. Stelescu, E. Manaila, G. Nicula, O. Iordache, L.C. Dinca, M.-D. Berechet, M. Vamesu, D. Gurau, "The improvement of the resistance to *Candida albicans* and *Trichophyton interdigitale* of some woven fabrics based on cotton," *Bioinorganic chemistry and applications*, vol. 2014, pp. 763269, 2014.